# Single-Photon Avalanche Diodes for Short-Wave Infrared detection

***Zoë Greener***

Submitted for the degree of Doctor of Philosophy

*Institute of Photonics and Quantum Sciences*

*School of Engineering and Physical Sciences*

*Heriot-Watt University*

**May 2022**

## Abstract

Single-photon detection is an exciting and rapidly advancing field with numerous emerging applications areas. There is a demand for highly efficient low noise single-photon detectors. 1310 and 1550 nm are particularly desirable detection wavelengths for use in time-of-flight imaging, light detection and ranging in automobiles, and low loss optical fibre transmission in quantum key distribution networks. Silicon based single-photon detectors dominate in the visible and near-infrared spectral ranges, but this report investigates the design and characterisation of planar Germanium-on-Silicon Single-Photon Avalanche Diodes (SPADs) as an efficient short-wave infrared detector. A single-photon detection efficiency of up to 30 % at a temperature of 125 K was achieved at a wavelength of 1310 nm, with dark count rates in the order of a few thousand counts per second, a low noise equivalent power of 4 x10 $^{-17}$ WHz$^{-1/2}$ and timing jitter as low as 126 ps at 150 K. These results represent the highest sensitivity and lowest jitter Ge-on-Si SPAD detectors demonstrated. These planar geometry Ge-on-Si SPADs show potential for operation at Peltier cooled temperatures and easy integration into readily available Si SPAD circuitry as well as high efficiency single-photon detection. Further investigation was performed into altering the thickness of the germanium absorption layer within the Ge-on-Si devices and the results showed potential to improve the single-photon detection efficiency with a refined fabrication process by growing thicker Ge layers to increase the absorption of SWIR photons. A selection of avalanche photodiodes fabricated in the alternative material system of InGaAsSb/GaSb and AlGaAsSb/GaSb were also investigated for operation in the short-wave infrared region.

This Thesis is dedicated to Patterson George Murray Inglis.

“Hope is born again in the faces of children”

## Acknowledgements

I would like to thank everyone who contributed to my research, and scientific development. Including my supervisor Professor Gerald Buller for guiding me through the process of research and the many opportunities I was given to travel and attend conferences. I am also grateful for all the research groups, scientists and engineers I got to meet, and the chances I had to work with a variety of people.

I would like to specifically thank Dr. Peter Vines for his initial help in getting my research started and Dr. Kateryna Kuzmenko for guiding me throughout the whole process, and her impressive intellect and dedication to the research. And I would like to also acknowledge Dr. Fiona Fleming, Dr. Xin Yi and Laura Huddleston for assisting me with everything experimentally and who will be continuing with the ground-breaking research I was able to be a part of and I hope they enjoy their time within the Single-Photon group.

I have thoroughly enjoyed working with the whole of the Single-Photon Group at Heriot-Watt University. And want to thank Dr. Aurora Maccarone, Dr. Rachael Tobin, Dr. Ross Donaldson and Dr. Aongus McCarthy for all the times they have helped me with equipment or given me advice. Neil Ross for helping me with the clean room equipment. Dr. David Canning, Dr. Ugo Zanforlin, and Dr. Pete Connolly were all great fun to work alongside. Professor Carl Pidgeon has been incredibly helpful in proofreading my work and steering it in the right direction.

Without Dr Jaroslaw Kirdoda, Dr Lourdes Ferre Llin, Dr Derek Dumas and Dr. Ross Millar under the supervision of Professor Douglas Paul none of my work would have been possible, so I would like to thank them for producing the devices and giving me the experience of working alongside a successful academic research group.

Finally, I would like to thank my partner Alan Inglis for giving me confidence in myself and supporting me throughout the ups and downs of scientific research. And my family who have always pushed me to do better.

# Research Thesis Submission

| | | | |
|---|---|---|---|
| Name*:* | Zoe Greener | | |
| School: | Engineering and Physical Sciences | | |
| Version: *(i.e. First, Resubmission, Final)* | Final | Degree Sought: | PhD |

## Declaration

In accordance with the appropriate regulations I hereby submit my thesis and I declare that:

1. The thesis embodies the results of my own work and has been composed by myself
2. Where appropriate, I have made acknowledgement of the work of others
3. The thesis is the correct version for submission and is the same version as any electronic versions submitted*.
4. My thesis for the award referred to, deposited in the Heriot-Watt University Library, should be made available for loan or photocopying and be available via the Institutional Repository, subject to such conditions as the Librarian may require
5. I understand that as a student of the University I am required to abide by the Regulations of the University and to conform to its discipline.
6. I confirm that the thesis has been verified against plagiarism via an approved plagiarism detection application e.g. Turnitin.

## ONLY for submissions including published works

7. Where the thesis contains published outputs under Regulation 6 (9.1.2) or Regulation 43 (9) these are accompanied by a critical review which accurately describes my contribution to the research and, for multi-author outputs, a signed declaration indicating the contribution of each author (complete)
8. Inclusion of published outputs under Regulation 6 (9.1.2) or Regulation 43 (9) shall not constitute plagiarism.

* *Please note that it is the responsibility of the candidate to ensure that the correct version of the thesis is submitted.*

| | | | |
|---|---|---|---|
| Signature of Candidate*:* | | Date: | |

## Submission

| | |
|---|---|
| Submitted By *(name in capitals):* | Zoe Greener |
| Signature of Individual Submitting: | *Z.Greener* |
| Date Submitted: | 04/05/2022 |

## For Completion in the Student Service Centre (SSC)

| | | | | | | | | | | |
|---|---|---|---|---|---|---|---|---|---|---|
| Limited Access | Requested | Yes | | No | | Approved | Yes | | No | |
| *E-thesis Submitted* ***(mandatory for final theses)*** | | | | | | | | | | |
| Received in the SSC by *(name in capitals):* | | | | | | Date: | | | | |

# Table of Contents

# List of Publications by the Candidate

**Papers Published in Journals**

F. Thorburn, X. Yi, **Z. Greener**, J. Kirkoda, R. Millar, L. Huddleston, D. Paul, G. Buller, Ge-on-Si single-photon avalanche diode detectors for short-wave infrared wavelengths, Journal of Physics: Photonics, (2021).

L.F. Llin, J. Kirdoda, F. Thorburn, L.L. Huddleston, **Z.M. Greener**, K. Kuzmenko, P. Vines, D.C.S. Dumas, R.W. Millar, G.S. Buller, D.J. Paul, High sensitivity Ge-on-Si single-photon avalanche diode detectors, Opt. Lett., 45 (2020) 6406-6409.

Y.D. Shah, P.W.R. Connolly, J.P. Grant, D. Hao, C. Accarino, X. Ren, M. Kenney, V. Annese, K.G. Rew, **Z.M. Greener**, Ultralow-light-level color image reconstruction using high-efficiency plasmonic metasurface mosaic filters, Optica, 7 (2020) 632-639.

K. Kuzmenko, P. Vines, A. Halimi, R.J. Collins, A. Maccarone, A. McCarthy, **Z.M. Greener**, J. Kirdoda, D.C.S. Dumas, L.F. Llin, M.M. Mirza, R.W. Millar, D.J. Paul, G.S. Buller, 3D LIDAR imaging using Ge-on-Si single-photon avalanche diode detectors, Opt. Express, 28 (2020) 1330-1344.

**Conference Proceedings**

R.W. Millar, J. Kirdoda, F. Thorburn, X. Yi, **Z.M. Greener**, L. Huddleston, B. Benakaprasad, S. Watson, C. Coughlan, G.S. Buller, Pseudo-planar Ge-on-Si single photon avalanche diode detector with record low noise-equivalent power, SPIE, pp. 45-52.

J. Kirdoda, R.W. Millar, F. Thorburn, L.L. Huddleston, D.C.S. Dumas, **Z.M. Greener**, K. Kuzmenko, P. Vines, L.F. Llin, X. Yi, Pseudo-planar Ge-on-Si single-photon avalanche detectors with low noise equivalent power, International Society for Optics and Photonics, pp. 1183107.

R.W. Millar, J. Kirdoda, F. Thorburn, L.L. Huddleston, D.C.S. Dumas, **Z.M. Greener**, K. Kuzmenko, P. Vines, L. Ferre-Llin, X. Yi, Ge-on-Si Single-Photon Avalanche Diode Detectors with Low Noise Equivalent Power in the Short-Wave Infrared, Optical Society of America, pp. 2_2.

J. Kirdoda, D.C.S. Dumas, R.W. Millar, M.M. Mirza, D.J. Paul, K. Kuzmenko, P. Vines, **Z. Greener**, G.S. Buller, Geiger mode Ge-on-Si single-photon avalanche diode detectors, IEEE, pp. 1-4.

K. Kuzmenko, P. Vines, **Z. Greener**, J. Kirdoda, D. Dumas, M.M.A. Mirza, R. Millar, D.J. Paul, G.S. Buller, Planar geometry Ge-on-Si SPAD detectors for the short-wave infrared (Conference Presentation), International Society for Optics and Photonics, pp. 109780P.

G.S. Buller, A. Halimi, A. Maccarone, X. Ren, R. Tobin, P.W.R. Connolly, **Z.M. Greener**, Y. Altmann, A. McCarthy, Three-Dimensional Imaging Under Extreme Conditions Using Single-Photon Counting, Optical Society of America, pp. AW3R-4.

# Glossary

| Abbreviation | Terminology | Description |
|---|---|---|
| APD | Avalanche Photodiode | Solid-state photodetector that exploits the internal gain provided by impact ionization. |
| CMOS | Complementary Metal-Oxide Semiconductor | A type of metal–oxide–semiconductor field-effect transistor fabrication process. |
| DCR | Dark count rate | The number of times per second a photodetector registers a detection event without external illumination. |
| Jitter | | Variation in risetime of the detector, typically characterised by the full-width half-maximum of the timing histogram. |
| LIDAR | Light Detection and Ranging | LIDAR is a remote sensing ranging technique which uses light to estimate the distance to an object. |
| NEP | Noise-Equivalent Power | The signal power required to attain a unity signal-to-noise ratio within a one second integration time. |
| NIR | Near Infrared | Defines a specific wavelength range approximately 0.7 – 1.4 μm. |
| PCC | Photon Counting Card | Computer hardware used to build histograms from single-photon detection data collected. |
| PMT | Photomultiplier Tube | Type of single-photon detectors which utilise the photoelectric effect to detect photons. |
| SNSPD | Superconducting Nanowires Single-Photon Detector | Single-photon detection technology based on superconductivity of nanowires. |

| | | |
|---|---|---|
| SPAD | Single-Photon Avalanche Diode | Solid-state photodetector operated in Geiger mode with single-photon sensitivity. |
| SPDE | Single-Photon Detection Efficiency | The probability that a single-photon generates a measurable current pulse across the photodetector. |
| SWIR | Shortwave Infrared | Defines a specific wavelength range approximately 1.4 – 3.0 μm. |
| TCSPC | Time-Correlated Single-Photon Counting | Technique used to measure the arrival time of single-photon events with respect to a reference signal. |

# Chapter 1. Introduction

This Thesis will describe the motivation behind producing highly efficient, picosecond resolution, low noise single-photon avalanche diodes (SPADs) for detection wavelengths in the near infrared (NIR) and short-wave infrared (SWIR) range. Much of the work will focus on Ge-on-Si SPADs, including the design and fabrication. Comparisons are made between Ge-on-Si SPAD detector designs that work under different operating conditions. The benefits and challenges for the specific applications will be investigated. Much of this Thesis will focus on the experimental methods used and the process required to characterise different types of single-photon sensitive devices, and the subsequent results and analysis feed into the design process in order to make device improvements. Comparisons will be made between devices already available and other prototype detectors still being optimised. InGaAsSb/GaSb avalanche photodiodes (APDs) will also be characterized and reported on as a longer term solution to the SWIR SPAD. Before conclusions about the future of SWIR single-photon detection are drawn.

Chapter 2 gives a brief introduction to single-photon detection and the benefits of using certain wavelengths in specific applications as well as an overview of the current devices available on the market that detect single photons in the infrared wavelength region. A summary of the advantages and disadvantages of each of these devices is given. A short explanation of APDs and SPADs is also included in this chapter.

Chapter 3 is a more in-depth study of the science behind PN junctions and how they form single photon avalanche diodes. This includes an explanation of impact ionisation, thick and thin junction detectors and gain and bandwidth mechanisms of the single-photon avalanche diodes. The theory behind desirable and non-desirable characteristics is explained thoroughly before the actual characterisation and factors for consideration when fabricating the devices are systematically described.

Chapter 4 focuses on short-wave infrared single-photon avalanche diodes already available, comparing the band structure of a current commercial InGaAs/InP SPAD detector to a Ge-on-Si device. The advantages and disadvantages of each material system are then assessed, as well as fabrication techniques and device design. Although both are avalanche photodiodes, InGaAs/InP devices have been developed since the 1970's and are commercially available, whereas Ge-on-Si remains a relatively immature detector technology at present. InGaAsSb/GaSb based SPADs are also mentioned as a potential avenue for further research but are still in the early stages of research. The motivation for producing highly efficient and low noise Ge-on-Si SPADs for detection of SWIR photons is examined, particularly for wavelengths of up to 1550 nm.

A quick review into previous research concerning Ge-on-Si detectors is performed in Chapter 5 as well as a more detailed explanation of the device characterisation experiments. Chapter 5 also includes details on the fabrication methods, the detailed experiments that were performed, final results and analysis of planar geometry Ge-on-Si SPADs. This includes the single-photon efficiency, dark count rate measurements, the noise equivalent power of the device and the jitter.

The phenomenon of afterpulsing is a major issue limiting the operation speed and DCR of avalanche-based devices, especially at low temperatures. This was thoroughly investigated in Chapter 6 which includes background information into research previously performed on InGaAs/InP SPADs, which describes the theory behind activation energies and their importance in improving the fabrication process. The experimental results on afterpulsing lifetime and analysis of the Ge-on-Si SPADs are then described. And to verify and compare the results, afterpulsing analysis was performed on a commercial all-silicon SPAD. Different methods of analysis were used based on fitting theoretical behaviours to the afterpulsing decay graphs, and from these, different activation energies were calculated. Following on from previous research we attempted to ascertain the physical significance of the afterpulsing time constants extracted from the results and activation energies.

Chapter 7 contains the results of the characterisation of InGaAsSb/GaSb and AlGaAsSb/GaSb APDs provided by Lancaster University. A small summary of background information and the theory behind the design and materials used is followed by IV results and an analysis of the issues we found during characterization. The information was then fed back to Lancaster University and the chapter finishes with some hypothesis of the cause of the issues we experienced.

And finally, Chapter 8 summarises the demand for efficient and fast single-photon avalanche diodes, the process of characterising the devices, the results and what can be inferred from them and lastly, ideas for potential experimental endeavours in the future.

# Chapter 2. Single-Photon Detectors

Scientific interest in single photons can be traced back to as early as the 1900s when Max Planck hypothesised light as a quantised packet of energy as opposed to wave propagation, followed shortly by Einstein in 1905 when he described the photoelectric effect. This led to a curiosity into the production and detection of single photons which peaked in the mid-1900s, with the famous Hanbury-Brown and Twiss experiment of 1956 [1]. Prior to this, infrared radiation (IR) was discovered over 200 years ago by astronomer Sir William Herschel and since then research has emphasised development of IR detectors and sources to harness the many exciting opportunities that arose from its discovery [2]. Some fascinating applications involve the use and consequently the detection of single photons. To date, many different types of single-photon detectors have been successful across a range of operational temperatures, detection efficiencies, and spectral regions including the IR. This PhD thesis will address aspects of single-photon detection in the short-wave infrared.

## 2.1 SWIR Single-Photon Detection

Single-photon detectors are essential in certain fields, for example: quantum key distribution, which allows the secure sharing of keys encoded on the single-photon level; and in some forms of quantum computing which could enable fantastically fast processing speeds but can require single-photons to form qubits. Biophotonics could benefit from detectors in the short-wave infrared region that work in low photon regimes and over short acquisition times to avoid damage to biological materials [3]. Single-photon detection combined with time-correlated single-photon counting has already been used in time-resolved imaging of florescent tissue and diffusing optical tomography [4]. In applications such as Lidar using SWIR as opposed to shorter wavelengths means a higher power can be used as the eye safety threshold is higher for IR than it is for visible light [5]. Another benefit of using SWIR for imaging purposes is the low levels of atmospheric scattering at some wavelengths [6].

There are many different types of single-photon detectors that work in the IR region of the spectrum;

- Superconducting nanowires boast impressive single-photon detection efficiencies, but require cryogenic cooling to low temperatures of typically less than 3 K [7, 8].
- Photomultiplier tubes are a well-established technology but even the best photomultiplier tubes are limited by their detection efficiency and, often have relatively poor jitter performance [9, 10].
- Quantum dot field effect transistors can be used for single-photon detection with high efficiency and the added benefit of preserving the quantum mechanical properties of the photogenerated carriers [11].
- Avalanche photodiodes can be used for the detection of single-photons. They are semiconductor-based devices that utilise impact ionisation to multiply photo-generated carriers to the level of a self-sustaining current. This is currently an exciting area of research with different materials, manufacture and design being investigated to extend the wavelength range of operation.

Single-photon detection using avalanche photodiodes form the subject matter of this thesis. Because they have such a wide variety of applications, no single-photon detector is considered optimum for all applications, with each detector type boasting their own unique benefits and disadvantages when used in a range of systems spanning medicine, astronomy, and industry. The main advantages and disadvantages of each detector will be discussed in this chapter.

## 2.2 Photomultiplier Tubes

Photomultiplier tubes are arguably the oldest inventions for detection of single photons in the visible and near-infrared wavelength range, they utilise the photo-electric effect and have been used for the detection of light since the 1930s [12, 13]. Since then, they have been used commonly in spectrophotometers and other laboratory-based instruments such as amplifiers and are capable of single-photon sensitivity [9, 14].

When an incident photon passes through the photocathode it produces a photogenerated electron via the photo-electric effect, the initial electron is then accelerated in a vacuum tube to a charged dynode with a higher positive charge relative to the photocathode. The initial

electron is accelerated to the first positively charged dynode, having enough kinetic energy to produce several secondary electrons at the dynode. These secondary electrons are accelerated towards the next dynode where further electrons can be released. This process continues through several dynodes until eventually at the final anode there are enough electrons collected so that a measurable current pulse is produced. Overall voltages as high as 1000 V may be required for the succession of dynodes to provide high gain in the photomultiplier tube, as shown in Figure 2.1.

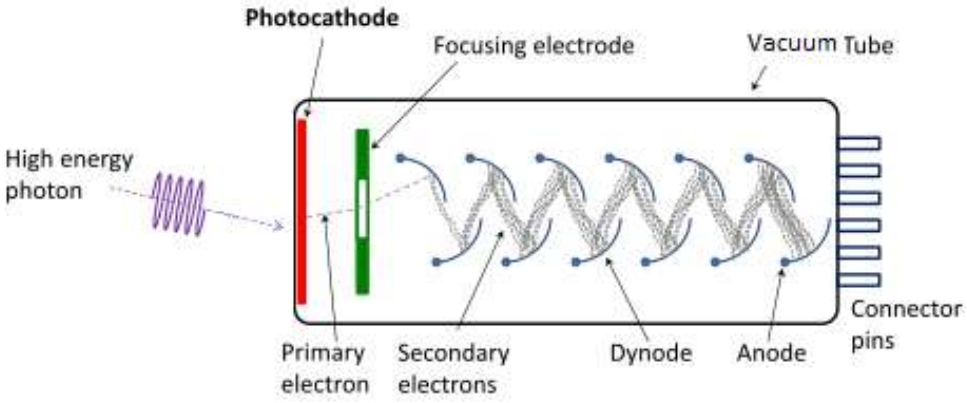


*Figure 2.1. A typical photomultiplier vacuum tube layout showing cathode where the incident photon generates the initial electron-hole pair before being accelerated towards the next dynodes where multiple electrons are produced through impact ionisation until the number of electrons is great enough for a detectable current to be produced at the anode. This takes place within a vacuum sealed tube [15].*

Quantum efficiencies of over 30 % can be achieved depending on wavelength [16]. Figure 2.2 shows the spectral variation of quantum efficiencies achieved by Hamamatsu photomultiplier tubes (PMTs) which are currently available. However due to their size and mechanically fragile material they can be impractical for use outside of a controlled environment, severely limiting their uses.

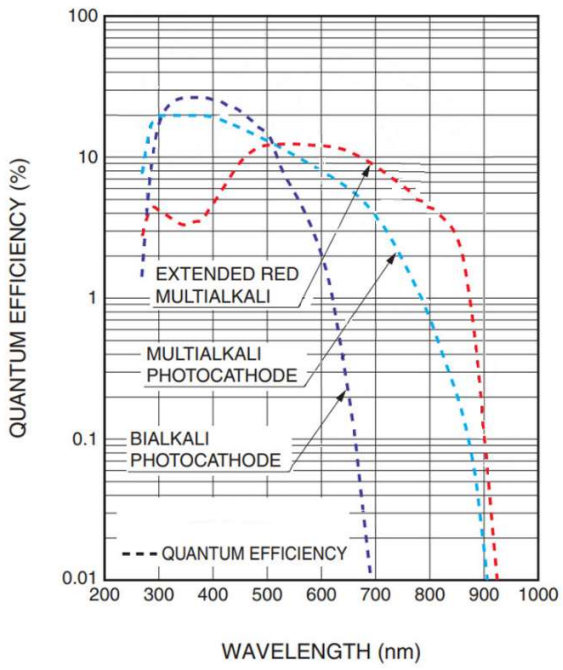


*Figure 2.2. Quantum efficiency dependence on wavelength of three PMT tube photomultipliers where the photocathode is made from Extended Red Multialkali (red), Multialkali (light blue) and Bialkali (dark blue)[17].*

### 2.3 Superconducting Nanowires

Although a relatively new detector technology, having first been demonstrated in 1991 by Gol'tsman *et. al.,* after discovering the resistive hotspot created when a photon is absorbed, superconducting nanowire single-photon detectors (SNSPDs) are another candidate for infrared photon detection. It has been reported single-photon sensitivity is possible using a niobium nitrite (NbN) SNSPD at wavelengths of up to 5 μm wavelength. This opens up many potential applications in the mid infrared such as defence against heat seeking missiles [18, 19]. They boast an impressive temporal resolution of as low as 3 ps using an NbN SNSPD but require temperatures of typically well below 4 K to achieve these results [20, 21]. Because superconducting nanowires can operate at infrared detection wavelengths and typically have very low jitter values of under 10s of picoseconds they can also be used in applications such as laser ranging experiments [20, 22, 23].

They consist of a thin nanowire cooled below the critical temperature and a current lower than the superconducting critical current is applied. When a photon is absorbed in the nanowire, a localised hot spot is created, leading to the nanowire momentarily going into a non-conducting state, causing a measurable current transient which is amplified and recorded. This process is outlined in Figure 2.3. The region needs to cool before it can return to its superconducting state, typically hot spot cooling takes as little as 10s of picoseconds [24, 25]. SNSPDs have recently shown efficiencies of over 90% using amorphous tungsten silicide nanowires [26].

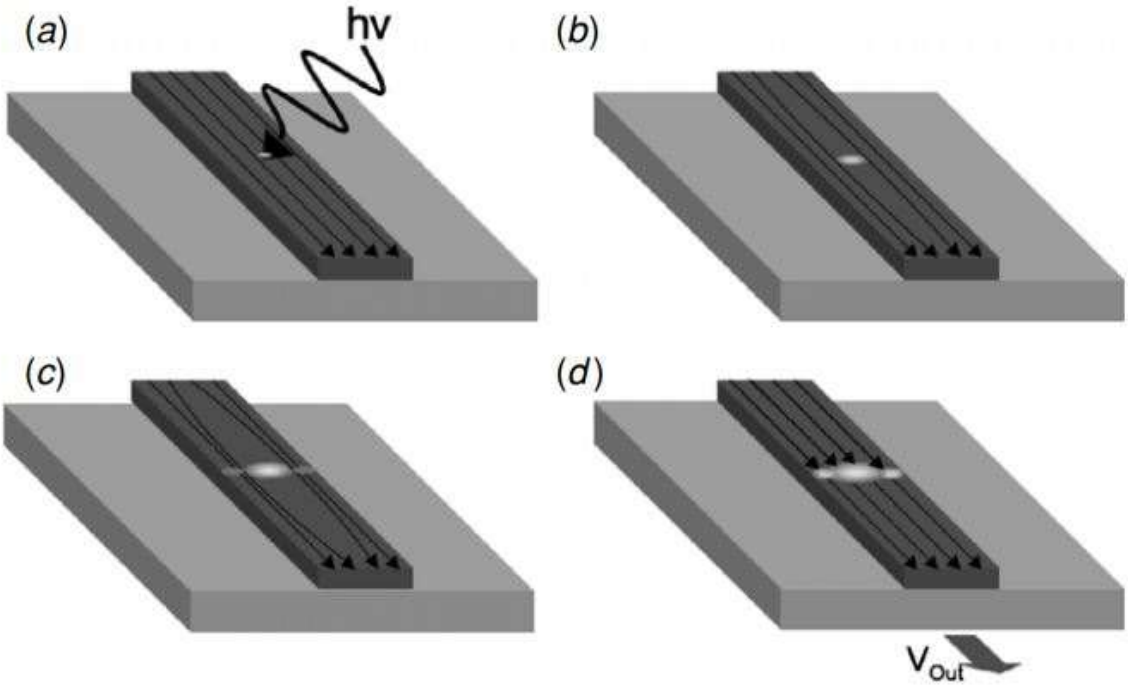


*Figure 2.3. The four stages of a superconducting nanowire single-photon detector in use. (a) The incident photon is absorbed by the superconducting nanowire, (b) this causes a localised heating effect. (c) The current is repelled by the hot spot and concentrated at the edges, (d) which causes a resistive barrier across the wire and the current is redirected. The voltage can be amplified for use with time-correlated single-photon counting electronics, the device needs to cool before the process can restart [27].*

Superconducting nanowire detectors have been used in quantum key distribution and for depth imaging using the time-of-flight approach, having been performed previously, over

long distances at eye-safe laser power levels. McCarthy *et al*. [28] highlight the importance and advancement of superconducting nanowires which were used to image objects at approximately a kilometre away with less than one-centimetre depth resolution. This demonstrates the potential for high-resolution, long distance eye-safe imaging using single-photon detectors. The high-resolution depth imaging is attributed to the 1560 nm detection wavelength where there is lower atmospheric attenuation as well as increased laser eye-safety thresholds. It is accepted that superconducting nanowires show impressive performance with regards to timing jitter, dark count rate and maximum count rates but are limited in applications as they typically operate efficiently at temperatures of less than 3K [29].

## 2.4 Quantum Dot Field Effect Transistors

Field effect transistors are devices used to amplify typically weak signals; they use an electric field produced by applying a voltage to the gate of the device to control the current flow across the active layer, as can be seen in Figure 2.4. By using quantum dots as the active layer of the device, between the source and the drain, researchers hope to produce versatile optoelectronic devices [30].

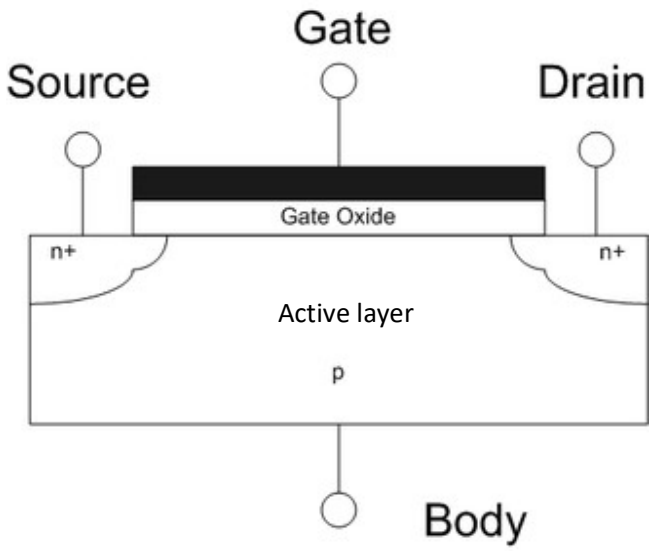


*Figure 2.4. Schematic of a field effect transistor that could have quantum dots forming the active layer of the device between the source and the drain.*

Quantum dots are semi-conductor nanocrystals that exhibit different qualities than their material in bulk form. They are so small that if they gain or lose an electron their properties change. A single photon absorbed by the quantum dot will produce an electron which is then detected by a nearby conducting channel. Because they do not rely on an avalanche process, they are less prone to multiplication noise. However, they can only operate at very low temperatures which gives rise to the discrete energy levels that produce electron tunnelling. Materials like GaAs/AlGaAs and InAs are used to give the quantum dot sensitivity to near infrared photons but the principles can be extended to facilitate longer wavelength detection [31]. The disadvantages of any field effect transistor is their susceptibility to overload voltages, as they can be vulnerable to electrostatic discharge or changes to threshold voltage during handling, usually once the device is installed this does not cause any issues. They are not as widely used as SNSPDs and SPADs, as they typically have lower detection efficiencies [32]. Field effect transistors can also have a very low resistance whilst they are on and a high resistance when they are off. However, during switching there is a significant transitional resistance, which can cause substantial amounts of power to be dropped whilst switching on and off. Thus, efficiency can hinder switching quickly, therefore field effect transistor circuits often have to compromise between their switching speed and power dissipation [33].

### 2.5 Introduction into Single-Photon Avalanche Diodes

As early as the 1900s solid state technologies were being investigated. This was around the same time as research into ionisation of trace gases in vacuum tubes and large advances came from studying the photoelectric effect inside semi-conductors and solids [34]. This then led to the mass production of APDs and SPADs implemented within the CMOS process in the early 2000s, and eventually to the variety of different SPAD and APD based circuits that are available today. APDs have become an increasingly popular choice as a photosensitive diode. And can be made from a variety of materials. APDs and SPADs are composed of a doped semiconductor material and the bandgap of the material chosen governs what photon energies can be absorbed and hence the operational design wavelength of the device. Silicon is currently the most popular choice for an APD because it has good multiplication properties and its also cost effective and abundant as silicon makes up 25 % of the Earth's crust providing ample supply. However, Si only works well for wavelengths within the visible

light range, up to approximately 1.1 μm, leaving a gap in the market for a highly efficient and reasonably priced APD or SPAD working in the SWIR range. For example, a material like Ge which absorbs wavelengths up to approximately 1600 nm or InGaAs/InP SPADs which have had extensive research showing efficiencies up to approximately 50 % in the SWIR spectral region with low noise and jitter [35-40]. A major advantage however, of Si SPADs is their compatibility with standard complementary metal oxide semiconductor (CMOS) processes which allows for use in large detector arrays. Si SPADs are currently used in a range of applications including the testing of quantum foundations [41], optical and free-space quantum communications [42] where the transmission loss is more acceptable then in optical fibres. And due to their high sensitivity and quick response time SPADs have been used in 3D imaging [43-45].

APDs and SPADs are formed from a basic PN junction, diffusion of particles across the junction forms a depletion region. This creates a small internal electric field. When a large external voltage is applied across the junction internal gain can be achieved via impact ionisation which leads to an avalanche process. The number of carriers exponentially increases within the device. This is called linear multiplication mode and is the basis of operation of an avalanche photodiode, or APD. This is explained in more detail in Chapter 3. If there is sufficient electric field that the avalanche breakdown voltage is exceeded the gain becomes infinite. With infinite gain, the electron-hole pair created by the absorption of a single-photon can induce a self-sustaining avalanche. When a device is operated in this regime it is referred to as Geiger mode operation, SPADs are designed to operate in this way. Although both APDs and SPADs are based on the same principles there will be slight design differences to allow SPADs to efficiently detect single photons whilst operating under higher voltages than an APD. At lower voltages the PN junction still operates successfully as a sensitive photodetector with a gain higher than unity but is not sensitive to single photons in the same way it is at higher voltages where avalanche breakdown occurs. Typical gain values for APDs are in the region of 10 to 100 and have a bandwidth approximately in the GHz regime for low multiplication levels. Whilst Si SPADs and APDs currently dominate the detector market, as mentioned previously they can only detect in the visible and near-infrared spectral range within wavelengths of approximately 400 nm to 1.1 μm [46]. Si SPADs have typical detection efficiencies of around 70% at 650 nm wavelength, and timing jitters of a

few tens of picoseconds [27, 47]. Operating temperatures are compatible with Peltier-cooling and they can be fabricated in CMOS electronics. They do not have as large a surface area as photomultiplier tubes, but this is superseded by their integration into arrays of Si SPADs for use in imaging applications.

Because conventional Si based SPADs tend to exhibit poor efficiency when used in the SWIR region whilst Si SPADs have been used in free-space time-of-flight imaging, the silicon's detection wavelength cut-off has limited its uses over long distances as described in McCarthy's paper [48]. There have been rapid advances in APDs recently with many researchers looking at expanding the bandwidth into the SWIR region to allow longer range imaging and low loss optical fibre transmission. A recent variation on a typical silicon SPAD is a Si photomultiplier which is emerging as a potentially valuable detector in single-photon or few photon applications like optical spectroscopy, biomedical applications and even for cameras in telescopes [49, 50].

The table below summaries the advantages and disadvantages of each of the detectors described above and gives examples of typical performance characteristics. Where the quantum efficiency is the probability that a photon in the detector is converted into an electron. And the single-photon detection efficiency (SPDE) is defined as the probability that a single photon hitting the detector will be converted into a measurable signal.

| Detector | Efficiency | Advantages | Disadvantages |
|---|---|---|---|
| Photo-multiplier tubes | Approximately 20 % single-photon detection efficiency in near infrared rising to above 50 % for visible light [51-53] | Nanosecond electron transit time | Requires voltages over 1000 V. Fragile, bulky and sensitive to magnetic fields. |
| Super-conducting nanowires | Quantum efficiency of 20 % at 1550 nm [54] and over 90 % single-photon detection efficiency in lab testing [26, 55] | Jitter and hotspot cooling can both be under tens of picoseconds [23-25]. Works in SWIR. | Only operates at a few Kelvin or lower making it impractical and expensive to operate. |
| Quantum dot field effect transistors | Typically, less than 10 % single-photon detection efficiency [32, 56]. | No avalanching means less multiplication noise | Can be sensitive to electrostatic and overload voltages making it delicate to install. Relatively new technology means limited research performed. |
| Single-photon avalanche diodes | Single- photon detection efficiency of up to 30 % at 800 nm in lab testing for Si devices [57]. InGaAs devices have efficiencies of 26% at 1550 nm and 45% at 1310 nm [58, 59]. | Peltier cooling compatible. And jitter values typically under a hundred picoseconds | Silicon detection wavelength limited to 1.1μm and expensive to manufacture InGaAs devices for use in SWIR applications which are not compatible with existing silicon circuitry. |

**References**


[1] R. Hanbury Brown, R.Q. Twiss, *A Test of a New Type of Stellar Interferometer on Sirius*, Nature, 178 (1956) 1046-1048.

[2] M. Rowan-Robinson, *Night Vision: Exploring the Infrared Universe, Cambridge University Press*, New York, NY, 2013.

[3] S. Bellis, C. Jackson, A. König, *Photon counting sensors for medical and biophotonic applications*, Laser+ Photonik, 5 (2005) 34-37.

[4] W. Becker, A. Bergmann, M. Kacprzak, A. Liebert, *Advanced time-correlated single photon counting technique for spectroscopy and imaging of biological systems*, International Society for Optics and Photonics, pp. 604714.

[5] I.E. Commission, *Safety of laser products-Part 1: Equipment classification and requirements*, IEC 60825-1, (2007).

[6] V. Lombardo, L. Merucci, M.F. Buongiorno, *Wavelength influence in sub-pixel temperature retrieval using dual-band technique*, Annals of Geophysics, 49 (2009).

[7] C.M. Natarajan, M.G. Tanner, R.H. Hadfield, *Superconducting nanowire single-photon detectors: physics and applications*, Superconductor Science and Technology, 25 (2012) 063001.

[8] S. Miki, T. Yamashita, M. Fujiwara, M. Sasaki, Z. Wang, *Multichannel SNSPD system with high detection efficiency at telecommunication wavelength*, Opt. Lett., 35 (2010) 2133-2135.

[9] R. Foord, R. Jones, C.J. Oliver, E.R. Pike, *The Use of Photomultiplier Tubes for Photon Counting*, Appl. Opt., 8 (1969) 1975-1989.

[10] B.L. Paredes, H. Araújo, F. Froborg, N. Marangou, I. Olcina, T. Sumner, R. Taylor, A. Tomás, A. Vacheret, *Response of photomultiplier tubes to xenon scintillation light*, Astroparticle Physics, 102 (2018) 56-66.

[11] E.J. Gansen, M.A. Rowe, D. Rosenberg, M. Greene, T.E. Harvey, M.Y. Su, R.H. Hadfield, N. Sae Woo, R.P. Mirin, *Single-photon detection using a semiconductor quantum dot, optically gated, field-effect transistor*, 2006 Conference on Lasers and Electro-Optics and 2006 Quantum Electronics and Laser Science Conference2006, pp. 1-2.

[12] S. Karl, *Electron multiplier*, Google Patents1940.

[13] P. Görlich, *Über zusammengesetzte, durchsichtige Photokathoden*, Zeitschrift für Physik A Hadrons and Nuclei, 101 (1936) 335-342.
[14] P. Liebman, G. Entine, *Sensitive low-light-level microspectrophotometer: detection of photosensitive pigments of retinal cones*, JOSA, 54 (1964) 1451-1459.
[15] Wikimedia, *Schematic view of a photomultiplier coupled to a scintillator, illustrating detection of gamma rays*, 2013.
[16] P. Dorenbos, J. De Haas, R. Visser, C. Van Eijk, R. Hollander, *Absolute light yield measurements on BaF/sub 2/crystals and the quantum efficiency of several photomultiplier tubes*, IEEE transactions on nuclear science, 40 (1993) 424-430.
[17] Hamamatsu, www.hamamatsu.com, Japan.
[18] G. Gol'tsman, A. Korneev, M. Tarkhov, V. Seleznev, A. Divochiy, O. Minaeva, N. Kaurova, B. Voronov, O. Okunev, G. Chulkova, *Middle-infrared ultrafast superconducting single photon detector*, 2007 Joint 32nd International Conference on Infrared and Millimeter Waves and the 15th International Conference on Terahertz Electronics, IEEE2007, pp. 115-116.
[19] E. Lippert, M.W. Haakestad, H. Fonnum, *High-energy mid-IR laser for defense against heat-seeking missiles*, SPIE, (2014).
[20] B.A. Korzh, Q.Y. Zhao, S. Frasca, J.P. Allmaras, T.M. Autry, E.A. Bersin, M. Colangelo, G.M. Crouch, A.E. Dane, T. Gerrits, *Demonstrating sub-3 ps temporal resolution in a superconducting nanowire single-photon detector*, arXiv preprint arXiv:1804.06839, (2018).
[21] G.N. Gol'tsman, A.D. Semenov, Y.P. Gousev, M.A. Zorin, I.G. Godidze, E.M. Gershenzon, P.T. Lang, W.J. Knott, K.F. Renk, *Sensitive picosecond NbN detector for radiation from millimetre wavelengths to visible light*, Superconductor Science and Technology, 4 (1991) 453-456.
[22] A. McCarthy, N.J. Krichel, N.R. Gemmell, X. Ren, M.G. Tanner, S.N. Dorenbos, V. Zwiller, R.H. Hadfield, G.S. Buller, *Kilometer-range, high resolution depth imaging via 1560 nm wavelength single-photon detection*, Opt. Express, 21 (2013) 8904-8915.
[23] R.H. Hadfield, *Superfast photon counting*, Nature Photonics, 14 (2020) 201-202.
[24] H. Zhang, L. Xiao, B. Luo, J. Guo, L. Zhang, J. Xie, *The potential and challenges of time-resolved single-photon detection based on current-carrying superconducting nanowires*, Journal of Physics D: Applied Physics, 53 (2019) 013001.

[25] L. Zhang, L. You, X. Yang, J. Wu, C. Lv, Q. Guo, W. Zhang, H. Li, W. Peng, Z. Wang, X. Xie, *Hotspot relaxation time of NbN superconducting nanowire single-photon detectors on various substrates*, Scientific Reports, 8 (2018) 1486.
[26] F. Marsili, V.B. Verma, J.A. Stern, S. Harrington, A.E. Lita, T. Gerrits, I. Vayshenker, B. Baek, M.D. Shaw, R.P. Mirin, S.W. Nam, *Detecting single infrared photons with 93% system efficiency, Nature Photonics*, 7 (2013) 210.
[27] G. Buller, R. Collins, *Single-photon generation and detection*, Measurement Science and Technology, 21 (2009) 012002.
[28] A. McCarthy, X. Ren, A. Della Frera, N.R. Gemmell, N.J. Krichel, C. Scarcella, A. Ruggeri, A. Tosi, G.S. Buller, *Kilometer-range depth imaging at 1550 nm wavelength using an InGaAs/InP single-photon avalanche diode detector*, Opt. Express, 21 (2013) 22098-22113.
[29] R.E. Warburton, A. McCarthy, A.M. Wallace, S. Hernandez-Marin, R.H. Hadfield, S.W. Nam, G.S. Buller, *Subcentimeter depth resolution using a single-photon counting time-of-flight laser ranging system at 1550 nm wavelength*, Opt. Lett., 32 (2007) 2266-2268.
[30] F. Hetsch, N. Zhao, S.V. Kershaw, A.L. Rogach, *Quantum dot field effect transistors*, Materials Today, 16 (2013) 312-325.
[31] A.J. Shields, M.P. O'sullivan, I. Farrer, D.A. Ritchie, R.A. Hogg, M.L. Leadbeater, C.E. Norman, M. Pepper, *Detection of single photons using a field-effect transistor gated by a layer of quantum dots*, Applied Physics Letters, 76 (2000) 3673-3675.
[32] B. Hsu, S.T. Chang, T. Chen, P. Kuo, P.S. Chen, Z. Pei, C.W. Liu, *A high efficient 820 nm MOS Ge quantum dot photodetector*, IEEE Electron Device Letters, 24 (2003) 318-320.
[33] S.M. Sze, *Semiconductor Devices*, Physics and Technology, 2nd ed.2002.
[34] F.C. Nix, *Photo-conductivity*, Reviews of Modern Physics, 4 (1932) 723-766.
[35] S. Pellegrini, R.E. Warburton, L.J.J. Tan, N. Jo Shien, A.B. Krysa, K. Groom, J.P.R. David, S. Cova, M.J. Robertson, G.S. Buller, *Design and performance of an InGaAs-InP single-photon avalanche diode detector*, IEEE Journal of Quantum Electronics, 42 (2006) 397-403.
[36] A. Tosi, N. Calandri, M. Sanzaro, F. Acerbi, Low-Noise, Low-Jitter, *High Detection Efficiency InGaAs/InP Single-Photon Avalanche Diode*, IEEE Journal of Selected Topics in Quantum Electronics, 20 (2014) 192-197.

[37] J. Zhang, M.A. Itzler, H. Zbinden, J.-W. Pan, *Advances in InGaAs/InP single-photon detector systems for quantum communication*, Light: Science & Applications, 4 (2015) e286-e286.
[38] L.C. Comandar, B. Fröhlich, J.F. Dynes, A.W. Sharpe, M. Lucamarini, Z.L. Yuan, R.V. Penty, A.J. Shields, *Gigahertz-gated InGaAs/InP single-photon detector with detection efficiency exceeding 55% at 1550 nm*, Journal of Applied Physics, 117 (2015) 083109.
[39] A. Restelli, J.C. Bienfang, A.L. Migdall, *Single-photon detection efficiency up to 50% at 1310 nm with an InGaAs/InP avalanche diode gated at 1.25 GHz*, Applied Physics Letters, 102 (2013) 141104.
[40] Z. Huang, *Germanium photodetector integrated with silicon-based optical receivers*, (2021).
[41] P. Shadbolt, J.C.F. Mathews, A. Laing, J.L. O'Brien, *Testing foundations of quantum mechanics with photons*, Nature Physics, 10 (2014) 278-286.
[42] C.J. Pugh, S. Kaiser, J.-P. Bourgoin, J. Jin, N. Sultana, S. Agne, E. Anisimova, V. Makarov, E. Choi, B.L. Higgins, T. Jennewein, *Airborne demonstration of a quantum key distribution receiver payload*, Quantum Science and Technology, 2 (2017) 024009.
[43] X. Ren, P.W.R. Connolly, A. Halimi, Y. Altmann, S. McLaughlin, I. Gyongy, R.K. Henderson, G.S. Buller, *High-resolution depth profiling using a range-gated CMOS SPAD quanta image sensor*, Opt. Express, 26 (2018) 5541-5557.
[44] A. Maccarone, F. Mattioli Della Rocca, A. McCarthy, R. Henderson, G.S. Buller, *Three-dimensional imaging of stationary and moving targets in turbid underwater environments using a single-photon detector array*, Opt. Express, 27 (2019) 28437-28456.
[45] S. Chan, A. Halimi, F. Zhu, I. Gyongy, R.K. Henderson, R. Bowman, S. McLaughlin, G.S. Buller, J. Leach, *Long-range depth imaging using a single-photon detector array and non-local data fusion*, Scientific Reports, 9 (2019) 8075.
[46] Excelitas, Photon Detection Solutions, 2020.
[47] K. Zang, X. Jiang, Y. Huo, X. Ding, M. Morea, X. Chen, C.-Y. Lu, J. Ma, M. Zhou, Z. Xia, Z. Yu, T.I. Kamins, Q. Zhang, J.S. Harris, *Silicon single-photon avalanche diodes with nano-structured light trapping*, Nature Communications, 8 (2017) 628.

[48] A. McCarthy, R.J. Collins, N.J. Krichel, V. Fernández, A.M. Wallace, G.S. Buller, *Long-range time-of-flight scanning sensor based on high-speed time-correlated single-photon counting*, Appl. Opt., 48 (2009) 6241-6251.
[49] F. Acerbi, G. Paternoster, A. Gola, N. Zorzi, C. Piemonte, S*ilicon photomultipliers and single-photon avalanche diodes with enhanced NIR detection efficiency at FBK*, Nuclear Instruments and Methods in Physics Research Section A: Accelerators, Spectrometers, Detectors and Associated Equipment, 912 (2018) 309-314.
[50] A. Asano, D. Berge, G. Bonanno, M. Bryan, B. Gebhardt, A. Grillo, N. Hidaka, P. Kachru, J. Lapington, S. Leach, *Evaluation of silicon photomultipliers for dual-mirror Small-Sized Telescopes of Cherenkov Telescope Array*, Nuclear Instruments and Methods in Physics Research Section A: Accelerators, Spectrometers, Detectors and Associated Equipment, 912 (2018) 177-181.
[51] Hamamatsu, Japan.
[52] C. Bayram, M. Razeghi, *ULTRAVIOLET DETECTORS: Nitrides push performance of UV photodiodes*, Laser Focus World, 45 (2009) 47-51.
[53] M. Ryan, R. Manijeh, *Ultraviolet avalanche photodiodes*, Proc.SPIE2015.
[54] F. Marsili, F. Najafi, E. Dauler, F. Bellei, X. Hu, M. Csete, R.J. Molnar, K.K. Berggren, *Single-Photon Detectors Based on Ultranarrow Superconducting Nanowires*, Nano Letters, 11 (2011) 2048-2053.
[55] M. Gu, X. Lin, D. Liu, W. Wang, X. Wu, *High-efficiency fast superconducting nanowire single-photon detector with a reflection grating structure*, Frontiers in Optics + Laser Science APS/DLS, Optical Society of America, Washington, DC, 2019, pp. JTu4A.50.
[56] E. Bellini, *Lead-free quantum dot solar cells with 10 % efficiency*, PV magazine2020.
[57] G. Angelo, P. Francesco, R. Ivan, M. Piera, G. Massimo, D.C. Sergio, *Planar silicon SPADs with improved photon detection efficiency*, Proc.SPIE2010.
[58] X. Meng, S. Xie, X. Zhou, N. Calandri, M. Sanzaro, A. Tosi, C.H. Tan, J.S. Ng, *InGaAs/InAlAs single photon avalanche diode for 1550 nm photons*, R Soc Open Sci, 3 (2016) 150584.
[59] M. Liu, C. Hu, X. Bai, X. Guo, J.C. Campbell, Z. Pan, M.M. Tashima, *High-performance InGaAs/InP single-photon avalanche photodiode*, IEEE Journal of selected topics in quantum electronics, 13 (2007) 887-894.

# Chapter 3. Single-Photon Avalanche Diodes

## 3.1 Semiconductor Materials

One of the most important aspect of producing high efficiency and low noise SPADs is the material choice. Because SPADs are made from semiconductors they have a unique set of properties that differ from conductors or insulators, with each material also exhibiting extremely different advantages and disadvantages. The properties of a material depend on the crystal structure formed from the lattice. The lattice is made up of repeating unit cells, with unit cells representing atoms in their relatively fixed position within the lattice. A face-centered cubic unit cell for example would have one atom at each of the 8 corners and in the centre of 6 of the cubic faces. Both germanium and silicon have diamond lattice structure which is, in essence, two face-centered cubic lattices overlapping each other, in this configuration there are four nearest neighbour atoms. In a lattice there are valence electrons that covalently bond with surrounding electrons. These bonds will begin to break above a certain temperature due to thermal vibrations, providing carriers for current and allowing conduction. At low temperatures the electrons are strongly bound, and the semiconductor does not conduct. In an isolated one electron (H, $He^+$ and Rydberg) atom the electrons have discrete energy levels given by Bohr model:

$$E = \frac{-m_o q^4}{8\varepsilon_0{}^2 h^2 n^2} \tag{3.1}$$

where $m_0$, is the free-electron mass, $q$ is the electronic charge, $\varepsilon_0$ is the free-space permittivity, $h$ is the Planck constant, and $n$ is a positive integer called the principal quantum number. At $n \geq 3$ energy levels split according to their angular momentum ($\ell$) and quantum number, so $n = 3$ contains levels $\ell=0$, $\ell=1$, and $\ell=2$ called 3s, 3p and 3d orbitals.

However, in a lattice atomic interaction between atoms causes these discrete energy levels to change. As you bring two separate atoms together, the discrete level, say one that is initially doubly degenerate whereby two electrons can contain the same energy split into two. As more atoms begin to interact in close range the energy levels split into an almost continuum of closely space levels. For example, in a silicon lattice only four valence electrons contribute to interatomic interactions as the other ten have far deeper energy levels. These four valence electrons would normally occupy 3s and 3p orbitals, two in each as 3s is doubly degenerate. But when they are in a lattice, 3s and 3p orbitals hybridise into four and therefore can contain

all four of the valence electrons in silicon, one in each orbital. Because electrons at T=0 will always occupy the lowest energy levels, in all atoms when the outer orbitals split, allowing lower orbitals to contain more electrons. This will form a gap between inner and outer orbits, called the valence and conduction bands. This is essentially what gives rise to the unique characteristics of semiconductors. Because of this band gap between the top of the valence band and the bottom of the conduction band a certain amount of energy is required to excite and electron into the conduction band where it can behave in a manner similar to a free electron. Except, due to the periodic potential of the lattice the apparent mass of the electron is slightly different, this is called its effective mass ($m_e$). Therefore, it's energy is given by Equation 3.2.

$$E = \frac{p^2}{2m_e} \tag{3.2}$$

Where $p$ is the momentum. This equation is important as the parabolic momentum energy curve for materials can be very different and dictate whether an electron can be directly excited into the conduction band, these materials are called direct bandgap semiconductors, or whether it requires momentum, as in the case of an indirect bandgap semiconductor like silicon in Figure 3.1.

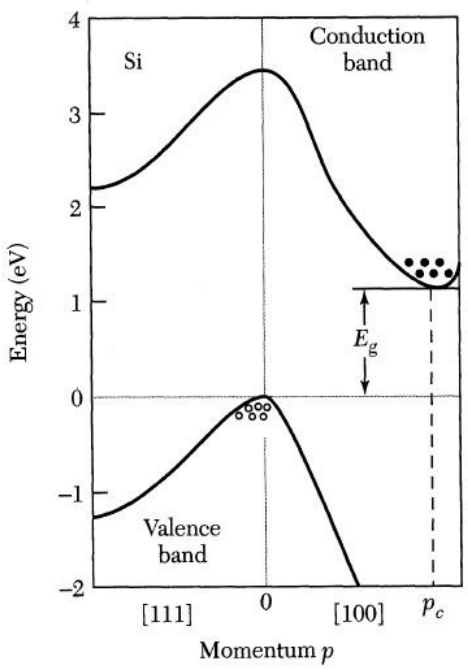


*Figure 3.1. Momentum-Energy diagram for silicon showing indirect excitation requiring a change in the electron's momentum [1].*

At low temperatures there are no electrons in the conduction band and therefore no conduction is possible but at high enough temperatures the bonds begin to break from the thermal vibrational energy lowering the resistance of the material. These characteristics are only valid for a semiconductor in thermal equilibrium, whereby there are no external factors that could affect the atomic behaviour such as light, electric field or pressure. And the material is in a steady condition at a given temperature.

The devices we are investigating in this thesis are extrinsic semiconductors. An extrinsic semiconductor is one which has been doped with impurities to increase the number of unbound carriers, a semiconductor can either be positively or negatively doped to increase the number of unbound holes or electrons respectively. Whereas an intrinsic semiconductor is made from one material and contains few impurities when compared with the thermally generated electrons and holes produced by the main material. Extrinsic semiconductors have dopants with either more or less electrons in the valence band, this means when the dopant is substituted into the lattice it can have either an extra electron that is not covalently bonded and therefore has a much lower binding energy or an extra hole which behaves in the same manner. A dopant with an extra electron is called a donor, and dopants with an extra hole are called acceptors. At low enough temperatures freeze out can occur, this is where there is not enough thermal energy for ionisation of any of the carriers, including the dopants. And at high enough temperatures there is enough thermal energy present for the intrinsic carrier concentration to become comparable to that of the donor concentration. The temperature which these events occur depends on the bandgap of the material and the concentration of dopants.

The Fermi level is the highest energy level an electron can occupy at T = 0 K. The higher the doping concentration the more the Fermi energy level moves, for a high acceptor concentration it will move closer to the valence band and equally with a high donor concentration it will move toward the conduction band. A semiconductor with a much lower concentration of dopants is called non-degenerate, and if the material is very heavily doped such that the Fermi energy gets so close to, or within 3 kT, or even moves inside the

conduction or valence bands, then the semiconductor can be referred to as degenerate. A degenerate semiconductor has a narrower bandgap given by Equation 3.3 [1].

$$\Delta E_g = 22(\frac{N}{10^{18}})^{1/2}\ (meV) \tag{3.3}$$

Where $\Delta E_g$ is the shift in the bandgap due to doping and N is the doping concentration in $cm^{-3}$.

### 3.2 PN Junctions

A PN junction is formed when an n-type and p-type semiconductor are in contact; the p-type material is positively doped and n-type negatively doped, and the excess of holes from the p-type and excess of electrons in the n-type will diffuse across the junction and combine because of the concentration gradient. This is called the diffusion current. The region where there are no free carriers is called the depletion region. The formation of the depletion region can be seen in Figure 3.2.

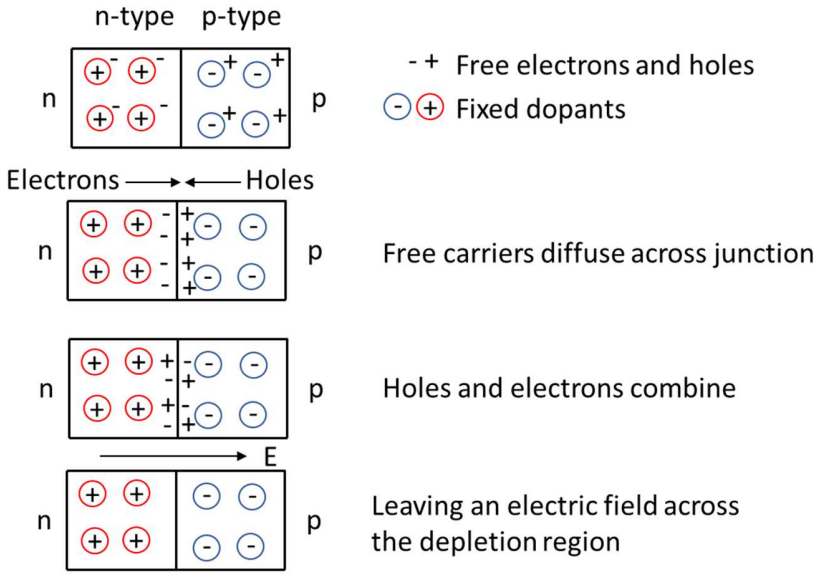


*Figure 3.2. A hypothetical examination of a PN junction formed when a p-type and n-type semiconductors are brought into intimate contact. Initially, there is an excess of holes in the n-type and excess holes in the p-type, and dopants fixed in position in the lattice. After coming into contact, the excess of holes and electrons in the p-type and n-type regions diffuse across the junction to establish equilibrium. The dopant centres remain in position. A net electric field opposes further carrier motion, forming a space-charge region, or depletion region, where free carriers are swept out.*

Within the depleted region the n-type material now becomes positively charged and vice versa in the p-type material. This produces an electric field which leads to two types of opposing carrier movement, the carrier diffusion caused by different doping concentrations and the drift caused by the electric field. The drift current pushes the holes in the p-type material and electrons in the n-type material away from the depletion region at the same time the high concentration of electrons and holes in n-type and p-type materials drives the diffusion current, forcing both electrons and holes towards the depletion region. When there is no net current across the device, it is said to be in equilibrium. This is caused by the diffusion current being equal and opposite to the drift current, so there is no flow of carriers. But there is a potential voltage that is built into the PN junction and can be estimated using Equation 3.4:

$$V_{bi} = \frac{K_B T}{q_e} \ln\left(\frac{N_a N_d}{n_i^2}\right) \tag{3.4}$$

Where $V_{bi}$ is the built-in voltage, $N_a$ and $N_d$ are the acceptor and donor concentrations. $n_i$ is the intrinsic carrier concentration and $q_e$ is the charge of an electron, $K_B$ is the Boltzmann's constant and T is the temperature. The intrinsic carrier concentration is the number of electrons in the conduction band which depends on the temperature and band gap of the material, the acceptor and donor concentrations are selected depending on the desired application of the PN junction.

Typically, the Fermi level lies just above the valence band in p-type and near to the conduction band in the n-type material. It is continuous across the boundary when the n-type and p-type material are brought together. The effect of applying a voltage across a PN junction can be seen in Figure 3.3.

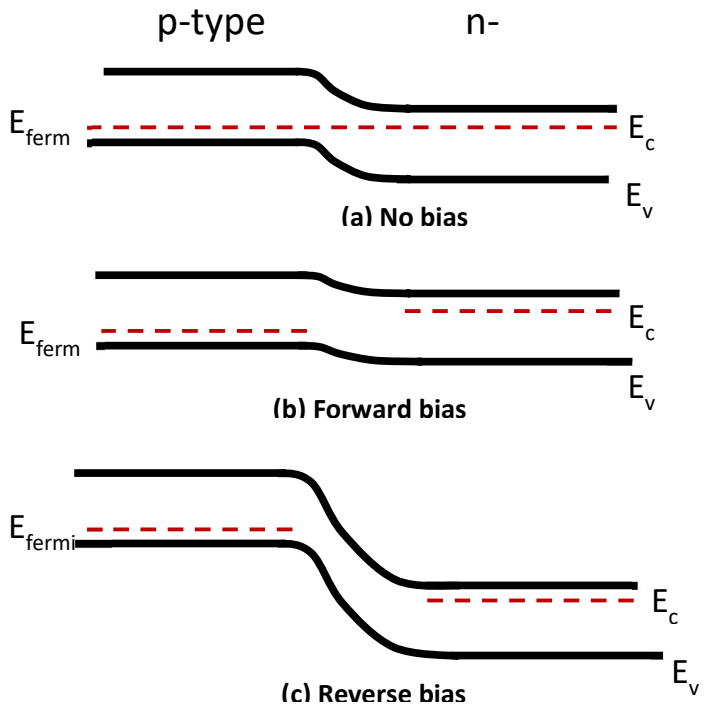


*Figure 3.3. Energy bands of a PN junction in (a) equilibrium and under (b) forward and (c) reverse bias operating conditions whereby $E_{fermi}$, $E_c$, and $E_v$ represent the Fermi energy and the energy of the conduction and valence bands.*

The overall resistance of the PN junction is reduced as the forward bias is increased. In these operating conditions the potential barrier is reduced, and a low impedance path is formed for carriers to travel across the barrier. The carriers that diffuse across the barrier do not do so indefinitely as it is favourable that they recombine. The distance at which equilibrium takes place is called the diffusion length and is typically of the order of micrometres [2]. However, the current is continuous across the device as the holes flow into the n-type region and recombine in a manner analogous to the flow of electrons. When the applied bias is equal to $V_{bi}$ there is no energy barrier and the PN junction becomes a conductor.

If a negative terminal is connected to the p-type side and positive to the n-type side the device is said to be reverse biased. The depletion region increases with bias as the electrons in the n-type and holes in the p-type are pulled towards the respective terminals. The most common and informative method of characterising reverse biased PN junction is the current-voltage characteristic. An example is shown in Figure 3.4.

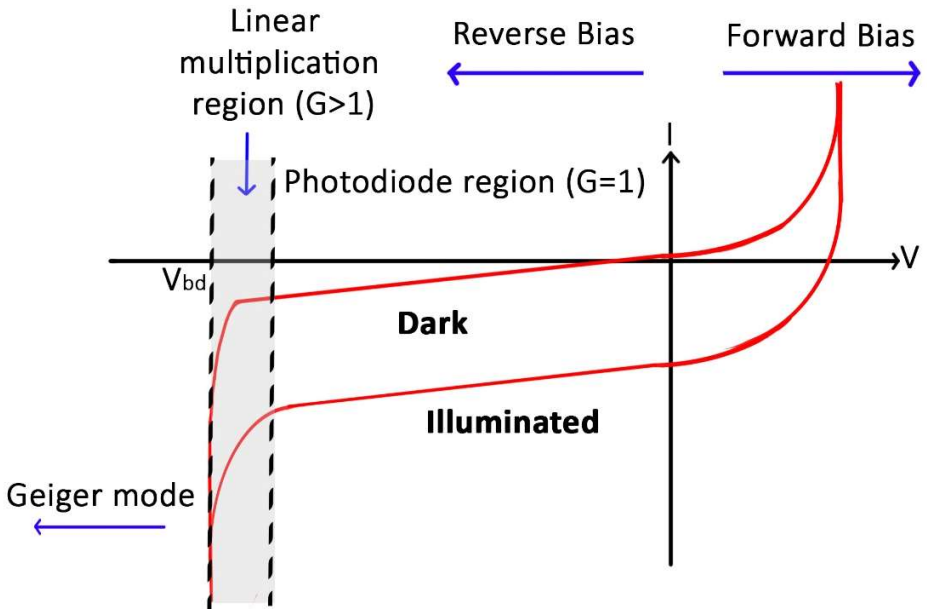


*Figure 3.4. Current-voltage characteristics for a PN junction under forward and reverse bias when in dark and illuminated conditions where the photodiode region is defined by where the gain (G) is equal to 1.*

As can be seen in Figure 3.4. Current-voltage characteristics for a PN junction under forward and reverse bias when in dark and illuminated conditions where the photodiode region is

defined by where the gain (G) is equal to 1 the current increases with reverse bias because the stronger the electric field the more probability that impact ionisation will take place.

There are many other factors that need to be considered in a reverse biased PN junction, such as minority carriers (the holes in the n-type material and electrons in the p-type material) which can move across the junction as they are not opposed by the electric field. Their movement produces a small current called the reverse saturation current. This reverse saturation current in addition to the thermal generation of carriers leads to a dark current in a reverse biased PN junction. Currents caused by surface leakage also contribute to the dark current and therefore the electrical noise of the devices. The level of surface leakage is a reflection of the quality of fabrication and the material used. In certain devices this can lead to power dissipation and therefore an increase in heat and a change in characteristics of the PN junction. This would be detrimental in most, if not all, applications. PN junctions can also be used as photodiodes, so when designing, and fabricating APD and SPAD devices these factors must be taken into account to ensure the dark current is kept low which produces a low noise device and allows more accurate photon detection to take place.

To summarise, the process in which a PN junction acts as a photodiode is as follows: when an incident photon with enough energy is absorbed within the depletion region where the initial electron-hole pair is created, separating the electron and hole as they drift in opposite directions due to the electric field. The electron and hole are pulled to opposite sides of the junction under the high electric field, and if the electric field across the device is large enough this movement can lead to impact ionisation and further electron-hole pairs being created during the process. Impact ionisation is described in more detail in the section below. If sufficient impact ionisation takes place then a detectable current caused by the movement of the many charge carriers across the junction is produced. In a linear avalanche photodiode the amount of incident radiation would vary linearly with the optical input signal. The level of gain in this linear multiplication region depends on the reverse bias voltage. In a single-photon avalanche diode the device is biased above the avalanche breakdown voltage, and a single photo-generated electron or hole can lead to the initiation of a self-sustaining avalanche photo-current.

### 3.3 Impact Ionisation

When a PN junction operates as an APD the device exhibits internal gain via the impact ionisation process. The primary carriers generated through photon absorption acquire sufficient kinetic energy in the applied electric field to cause further impact ionization. Mobility is therefore an important parameter as it dictates how strongly the carriers motion will be influenced by an applied electric field. An electron in the conduction band under a high enough electric field gains sufficient kinetic energy before it collides with the lattice, such that it can then transfer some of its energy to the lattice on impact and exciting an electron from the valence to the conduction band which leaves a hole in the valence band. After the impact ionization event, the original primary electron and the secondary electron and hole drift in the high electric field, leading to additional electron and hole impact ionisation events. This process continues, creating further electrons and holes, forming an avalanche photocurrent, as shown in Figure 3.5. The electrons and holes are swept across the device in opposite directions both contributing to the current across the diode. Therefore, a material like silicon makes a good multiplication region because the mobility ratio between the electrons (with mobilities of approximately 1400 $cm^2V^{-1}s^{-1}$ [3, 4]) and holes (with mobilities of approximately 450 $cm^2V^{-1}s^{-1}$ [3, 4]) is high. This means that electrons will gain the necessary kinetic energy from the applied electric field to cause impact impact ionisation, preferentially to holes travelling in the opposite direction. As the electric field is increased, the average gain increases, as shown in the bottom left-hand quadrant of the graph in Figure 3.4. If the electric field is increased past a certain point, then eventually the gain will effectively become infinite, this is avalanche breakdown.

Under reverse bias operating conditions when a high enough voltage is applied the depletion region breaks down in a reversible avalanche process. The amount of energy required for the initial photon absorption event to take place depends on the bandgap of the material, which must be equal or smaller than the energy of the incident photon. Therefore, the selection of material that initially absorbs the photon will dictate the wavelengths and efficiency at which absorption takes place.

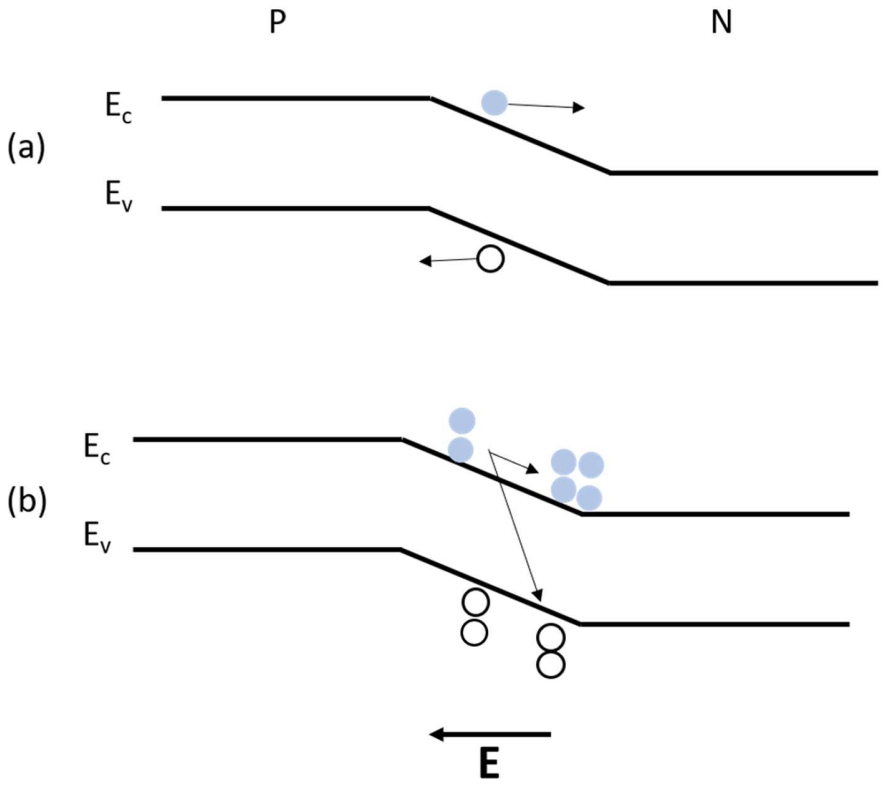


*Figure 3.5. The process of impact ionisation (a) where an electron hole pair is formed under an electric field and pulled to opposite sides of the junction (b) colliding with other electrons after gaining energy from the electric field which leads to further impact ionisation of both holes and electrons causing an avalanche effect. Where $E_c$ and $E_v$ are the energy levels of the conduction and valence band respectivley.*

### 3.4 Avalanche Photodiodes

APDs and SPADs generally operate under different conditions. APDs are designed to operate at electric fields which produce internal gain, as shown in the G > 1 region of Figure 3.4. SPADs are designed to be operated in Geiger mode where the applied voltage is higher than the avalanche breakdown voltage ($V_{bd}$). The higher electric field across the device in Geiger mode means that a self-sustaining current can be triggered by an incident single photon creating a single electron-hole pair. This gives the device single-photon sensitivity, unlike APDs that operate at lower voltages and produce a current that is linearly proportional

to the amount of light detected. Recent research has shown it is possible to detect single-photons within the linear multiplication range at very high multiplication levels, typically APDs do not have such capabilities [5].

Linear multiplication APDs are operated at a bias which provides an internal gain and have typical bandwidths of greater than 1 GHz. APDs, unlike SPADs, automatically recover after each avalanche event. In a SPAD detector, the device is biased to greater than avalanche breakdown, meaning that an initial impact ionization event can lead to a self-sustaining avalanche current. If a self-sustaining current occurs it will need to be stopped (quenched) using external circuitry which acts to bring the device below the breakdown voltage. SPAD detectors have a digital output; it is a trigger device that can only detect the presence or absence of a single-photon and cannot distinguish the exact number of photons arriving at exactly the same time.

### 3.5 Quenching Single-Photon Avalanche Diodes

Because SPADs work above breakdown voltage where self-sustaining avalanche currents can occur, the device will need to be quenched after an avalanche event so that the applied voltage drops below breakdown, before being able to detect a subsequent photon. In this sense a SPAD can be considered a digital detector; either it does or does not detect photons before the circuit gets quenched and the device resets. A SPAD cannot detect the difference between one and two or more photons that are incident at the same time, the detector is either triggered or not.

Quenching can be performed passively where a high resistor is connected in series to the SPAD. During the avalanche process the resistance of the SPAD significantly reduces and so most of the potential is dropped across the external resistor which reduces the applied bias of the SPAD to well below avalanche breakdown for a short period while the circuit recovers. Gating is another technique for quenching a circuit, where the extra voltage required to bring the device above breakdown is only applied for a set amount of time. For example, a DC

voltage is applied to the device just below breakdown and an AC voltage is added to bring the device periodically above and below the breakdown voltage. Another form of quenching is active quenching involving a fast comparator which switches the current in an emitter-coupled transistor pair when an avalanche takes place, the negative pulse applied quickly quenches the bias. The use of these different approaches depends on the operational circumstances and detector layout used. Passive quenching typically has a slower recovery time than active quenching, with its recovery time being dominated by the RC time constant of the device capacitance and quenching resistor, this could be as high as 100's ns. Gated quenching works well in quantum key distribution where photon arrival times can be accurately predicted but are not as effective as in time-of-flight ranging where the distance to the scene is often unknown. In our experiments we use a gated quenching technique with a DC voltage approximately 1.4 V below the breakdown voltage of the device and apply AC voltages high enough to bias the SPADs up to an excess bias of approximately 6.5 %.

### 3.6 Silicon Single-Photon Avalanche Diodes

Silicon SPADs are a well-researched and readily available area of single-photon detection, they are low cost and work in the visible spectral range up to 1100 nm, with maximum responsivity in the 400 nm to 600 nm wavelength range. Silicon SPADs are an ideal solution for less expensive imaging and photon counting applications, as silicon is abundant and has good multiplication properties. The microstructure for a basic silicon SPAD can be seen in Figure 3.6. Photons are incident on top of the device and the Si-diffused and Si-substrate regions act as the P and N part of the junction. The reach-through APD has a thick absorption region, and the primary carriers drift towards a thin multiplication region. The multiplication and absorption region are separate, this means each level of doping can be adjusted to maximise that region's function. In a perfect device, incident photons should be able to penetrate through to the absorption region without any loss in the n-type Si-diffused region. Reach-through SPADs have larger depletion regions but prevent impact ionisation occurring in most of the device, except the defined small multiplication region. To achieve this, they require a thick depletion region so absorption can take place in a lightly doped layer and multiplication in a separate, much thinner region. This way an electric field can extend through the absorption region and into the positively doped layer, assisting the carriers

towards the multiplication region. This also means a higher operating voltage and subsequently more energy is required for thicker SPADs. The avalanche is initiated by electrons in the multiplication region and an efficient device confines the impact ionisation to only the multiplication region.

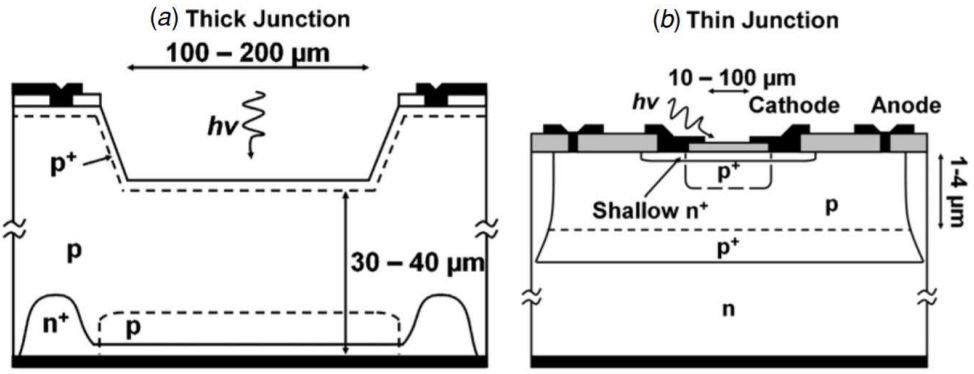


*Figure 3.6. (a) A basic schematic diagram of a thick junction and a (b) thin junction Si-SPAD where the photon is absorbed at the top of the device and multiplication takes place under a strong electric field. [6, 7].*

In the thick junction device shown in Figure 3.6. (a), the peak electric field is maintained over the longer multiplication region (typically 10's µm), meaning higher photon absorption. It also leads to a higher trigger probability, which is the likelihood of a self-sustaining avalanche occurring on creation of the primary carrier. In the thin-junction device the multiplication region is typically ~ 1 µm thickness, leading to reduced absorption and lower trigger probability. The thickness of the depletion region in a SPAD dramatically effects its performance, with thicker absorbers having a greater single-photon detection efficiency. These thicker structures mean that the device diameters are larger, which leads to a slower jitter. However, thinner junction devices have reduced detection efficiencies but perform with much faster jitters [8]. This makes thin junction devices better for some applications because of their superior timing resolution and lower power consumption. Thick planar devices have high efficiency because of their thick absorption region, but this leads to a slow response time as carriers within the multiplication region respond quickly whilst carriers in the neutral region lag behind, limiting the speed of the device to 100s of picoseconds [9]. One of the significant benefits of using silicon as a SPAD is that they are compatible with

CMOS circuitry. Standard CMOS circuitry allows the fabrication of high density thin-junction SPAD arrays with intricate on-chip electronics which can be used in counting and or timing applications as they offer all the benefits of microelectronic devices such as low voltage and power requirements alongside the advantage of being small and compact [10].

### 3.7 Characterisation Parameters

One important quality in a SPAD is the SPDE, defined as the probability that a single-photon generates a measurable current pulse across the device. However, events can occur inside photodetectors called dark events, where a current is produced without any illumination, this is characterised as the Dark Count Rate (DCR). And can be caused by thermally generated carriers. Afterpulsing is a phenomenon in which carriers are trapped within the device after an avalanche event. This contributes to the dark count rate because the carriers are then released after the avalanche event, and this leads to a subsequent false detection after the first initial detection. Afterpulsing is caused by carriers being trapped inside lattice defects. These traps can have a number of origins, sometimes associated with material defects, but also with surfaces and hetero-interfaces. So SPAD design and improvements in material quality can reduce the chances of afterpulsing taking place. The rate of afterpulsing decreases as the time after the initial event increases, due to the finite trap lifetime. The trap lifetime will decrease with increasing temperature, meaning that room temperature SPADs are much less affected than cryogenically cooled SPADs. Afterpulsing will be discussed in more detail in Chapter 6.

Noise equivalent power is defined as the signal power required to attain a unity signal-to-noise ratio within a one second integration time. It takes into account both the detection efficiency and the dark count rate and is a measure of the device sensitivity.

Another parameter which is essential for a fast-responding device is the jitter. The timing jitter is the full width at half-maximum of the instrumental response, as measured in timing histogram form and tells us the variation in the risetime of the detector pulse for many short

laser pulses incident on the detector (where the laser pulse duration is much shorter than the detector jitter).

### 3.8 Performance of Silicon Single-Photon Avalanche Diodes

The SPDE of a single-photon detector is an important characteristic of a SPAD, describing its detection efficiency. It encompasses the entire process from absorption to external electronic detection. The SPDE is the ratio of detectable events divided by the photon flux. This only is valid in the sparse photon regime and assumes that the photons are spaced in time sufficiently to allow detection, whereby only one photon can arrive at the detector at any one time and the detector must be fully operation before the next photon. To increase the SPDE of a device, one must maximize its likelihood of absorbing photons. Silicon SPADs have been refined since the 1960s. Even in the 1980s silicon SPADs worked at room temperature and had impressive timing jitters in the order of tens of picoseconds [11-13]. Currently, it is possible to achieve over 80 % detection efficiency from silicon SPADs when operating within the visible light regime [14-16]. Many factors affect the SPDE of a device, factors such as the refractive index of the surface of the device which can lead to reflection. An anti-reflection coating is therefore essential when fabricating high sensitivity devices, but care must be taken with the design of the AR coatings to be consistent with the operational range of the detector.

Photons that do pass through the device may not be efficiently absorbed within the device. A material with a high absorption coefficient at the desired wavelength will help maximize the number of photogenerated carriers created, when used in conjunction with a sufficiently thick absorption region it would increase the likelihood of photons being absorbed. Recombination is another problem that contributes to a reduced SPDE and can be caused by lattice defects at the heterostructure surface which act as recombination centres and careful fabrication can reduce the chances of contaminants introducing more defects. If the electric field strength across the device is zero or very low in the absorption region the photogenerated electron-hole pairs can only diffuse in the absorption region and recombination is likely to occur prior to the carriers entering the multiplication region.

Another factor is the likelihood of a photo-generated carrier entering the gain region if there is a discontinuity in the band-gap, as in the case of InGaAs/InP SPADs (see next Chapter). Finally, there is the trigger probability, which is the probability that once a photo-generated carrier enters the gain region it will cause a self-sustaining avalanche. The trigger probability will depend on the length of the gain region and the shape of the longitudinal electric field profile. The SPDE as a percentage is calculated using Equation 3.5.

$$SPDE\ (\%) = \frac{N_d}{F \times t \times N_{ppp}} \times 100 \tag{3.5}$$

Where '$N_d$' is the number of photons detected, 'F' is the frequency of the laser pulses, 't' is the time over which the reading was taken and '$N_{ppp}$' is the number of photons per pulse. The number of photons per pulse ($N_{ppp}$) is calculated from the laser frequency, wavelength, power, and attenuation all of which can be adjusted as show in Equation 3.6.

$$N_{ppp} = \frac{P \times \lambda}{F \times c \times h} \tag{3.6}$$

Where 'P' is the laser power, 'F' is the frequency, 'λ' is the wavelength, 'c' is the speed of light and 'h' is Planck's constant. The frequency and acquisition time are easily varied parameters which are dependent on the device performance during the experiment. The parameters are varied to get the most reliable and accurate results from testing. If the frequency is too high afterpulsing can distort the results and if the frequency is too low the acquisition time and therefore the whole experiment would take longer to perform. A simple time-correlated single-photon counting (TCSPC) experiment is used to produce a timing histogram which is then analysed to calculate the number of photons that were detected $'N_d'$. The number of events (after the dark counts had been removed) is counted over the histogram laser peak and used to calculate the SPDE. An example of a typical histogram used to collect SPDE data can be seen in Figure 3.7.

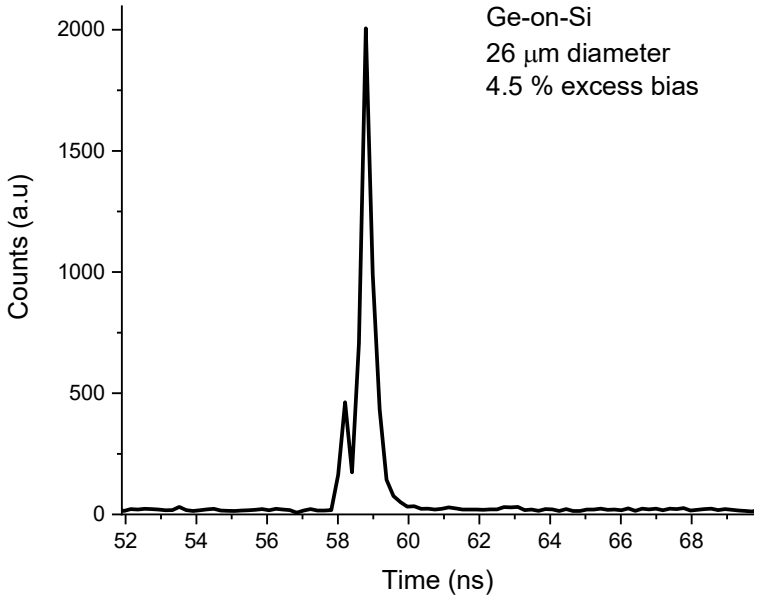


*Figure 3.7. An example of a timing histogram collected from a TCSPC experiment used to calculate the SPDE of a Ge-on-Si SPAD.*

The DCR of a SPAD is the rate at which events are recorded when there is no external light incident on the detector. These can be caused by thermal excitation, tunnelling, or trapped carriers from a previous illumination; it is a false positive which will contribute to the error rate in measurements and gives the minimum count rate of the device. As the active area of the device increases, the likelihood is that the dark count rate will increase. It has been shown with SPADs that there is a linear relationship between active area and the DCR [17]. In certain cases, a larger active area can mean more light can be detected when the illuminated spot size becomes a limiting factor. These are factors that should be considered when designing a SPAD. Microlenses can help address this issue by effectively increasing the active area without increasing the device volume. Microlenses have been used in CMOS SPAD detector arrays to help concentrate the light from a relatively large area into a small detector diameters [18]. They can be both refractive or diffractive structures and are typically made of fused silica. By incorporating microlenses it makes it possible to have a smaller active area device and hence a reduced DCR whilst achieving similar incident photon flux to that of the much larger microlens diameter. Another factor which needs to be balanced in is the excess bias applied during testing, again, a higher bias increases the SPDE but also

increases the DCR as more carriers are generated. The excess bias is defined in percentage terms in Equation 3.7 for an electrically gated SPAD.

$$Excess\ Bias\ (\%) = \frac{V_{dc}+V_{ac}-V_{bd}}{V_{bd}} \times 100 \tag{3.7}$$

$V_{dc}$ is the voltage of the direct current applied to the device, $V_{bd}$ is the voltage at which the device breaks down. $V_{ac}$ is the voltage of the alternating current which is used to operate the device in Geiger mode and quench it periodically using a gating technique. This is further explained in Chapter 5. The breakdown voltage is also dependent on the temperature, it decreases at lower temperatures as the kinetic energy of the internal carriers decreases. The dark count rate in counts per second (cps) is calculated using Equation 3.8.

$$DCR\ (cps) = \frac{N_{dark}}{F \times t \times \tau} \tag{3.8}$$

$N_{dark}$ is the number of dark events detected, and $\tau$ is the time window of the histogram we analysed the data over. 'F' is the frequency of the laser pulses and 't' is the time over which the reading was taken. A larger time range would give more data and possibly more accurate results, however including data from the edges of the histogram would include counts caused by transients in the device. To compromise, the flattest part of the histogram was used to calculate $N_{dark}$.

The noise equivalent power (NEP) is a useful parameter when comparing photon detection devices. It gives a measure of the weakest optical signal that can be detected and therefore a desirable, sensitive detector will have a low NEP. NEP takes into account both the SPDE and the DCR with the following Equation 3.9 [19].

$$NEP\ (WHz^{-\frac{1}{2}}) = \frac{hv}{SPDE} \times \sqrt{2 \times DCR} \tag{3.9}$$

The jitter can often represent the temporal response of a single-photon detector. The reliability and repeatability of the time taken for a photon to produce an avalanche and subsequently an electrical pulse is important in many SPAD applications including ranging and time resolved spectroscopy, where precise timing is essential [20]. This assumes that other jitter contributions in the timing system are negligible compared to the detector jitter. The deviation in the instrumental response is measured with a histogram, in our experiment,

and the arrival time of the photons was measured with a timing bin of 9.77 ps. The jitter should follow a Gaussian distribution, as a normal error should lead to an equal number of measurements above and below the mean value.

Figure 3.7 is an example of a timing histogram for a Ge-on-Si SPAD, illustrating the detector jitter.

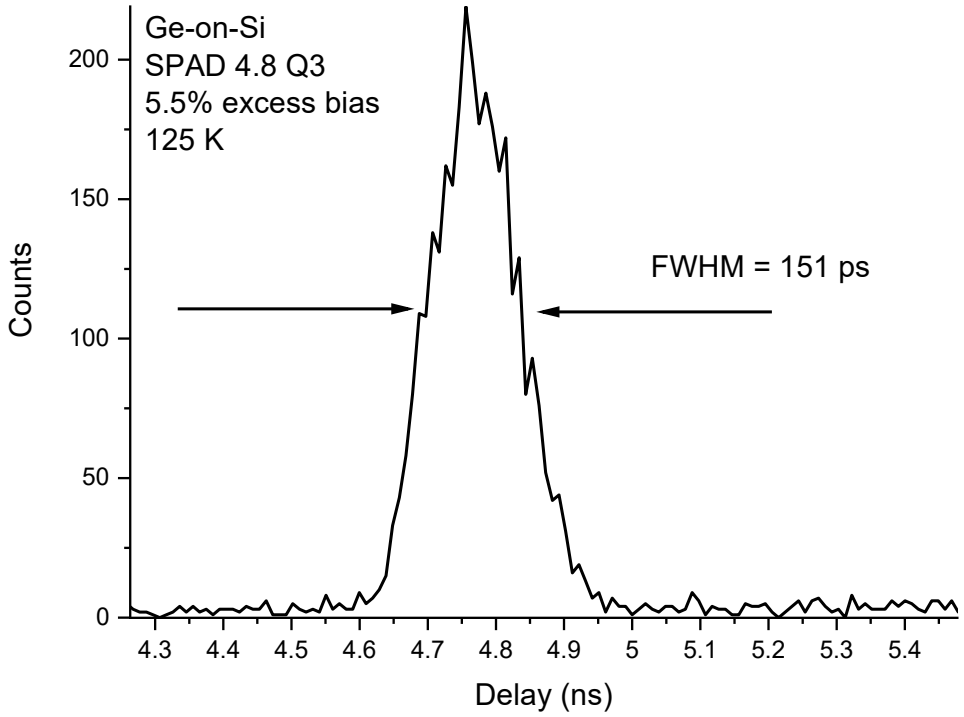


*Figure 3.7. A typical timing histogram illustrating the detector jitter. The timing jitter is typically characterised as the full-width-at-half-maximum of the histogram as indicated with arrows.*

Photons which are absorbed by the device can cause avalanche current, and some of the carriers can be captured by traps caused by defects in the lattice. These carriers are subsequently released a considerable amount of time after initial illumination of the SPAD takes place. These carriers cause dark events, leading to the phenomenon known as afterpulsing which can make a significant contribution to the DCR. Factors affecting the afterpulsing are temperature, fabrication quality and the detector reset time delay after the initial avalanche. Over time the rate of trapped carriers being released is reduced as the traps

are emptied. At higher temperatures the traps in the device are emptied much faster, since all SPADs must have a "dead-time" after each event as the detector is reset, afterpulsing ceases to be an issue if the trap decay time is less than the dead-time [21]. The quicker the traps empty, the lower the chances of a carrier being released between laser pulses. The probability of afterpulsing with respect to time shows an exponential decay.

Since afterpulsing is caused by trapped carriers, one can find the activation energy of traps by performing afterpulsing decay measurements as a function of temperature. By isolating the origin of traps responsible for afterpulsing, it may be possible to design improved SPAD detectors.

**References**


[1] S.M. Sze, *Semiconductor Devices*, Physics and Technology, 2nd ed.2002.

[2] J.R. Hook, H.E. Hall, *Solid State Physics,* 2013.

[3] G.W. Ludwig, R.L. Watters, *Drift and conductivity mobility in silicon*, Physical Review, 101 (1956) 1699.

[4] *Physical Properties of Semiconductors* NSM Archive.

[5] A.S. Huntington, M.A. Compton, G.M. Williams, *Linear-mode single-photon APD detectors*, SPIE, pp. 145-155.

[6] G. Buller, R. Collins, Single-photon generation and detection, *Measurement Science and Technology*, 21 (2009) 012002.

[7] F. Zappa, S. Tisa, S. Cova, P. Maccagnani, D.B. Calia, R. Saletti, R. Roncella, G. Bonanno, M. Belluso, *Single-photon avalanche diode arrays for fast transients and adaptive optics*, IEEE Transactions on Instrumentation and Measurement, 55 (2006) 365-374.

[8] K. Zang, X. Jiang, Y. Huo, X. Ding, M. Morea, X. Chen, C.-Y. Lu, J. Ma, M. Zhou, Z. Xia, Z. Yu, T.I. Kamins, Q. Zhang, J.S. Harris, *Silicon single-photon avalanche diodes with nano-structured light trapping*, Nature Communications, 8 (2017) 628.

[9] J. Cheng, S. You, S. Rahman, Y.-H. Lo, *Self-quenching InGaAs/InP single photon avalanche detector utilizing zinc diffusion rings*, Opt. Express, 19 (2011) 15149-15154.

[10] M. Ghioni, A. Gulinatti, I. Rech, F. Zappa, S. Cova, *Progress in Silicon Single-Photon Avalanche Diodes, Selected Topics in Quantum Electronics*, IEEE Journal of, 13 (2007) 852-862.
[11] M. Ghioni, S. Cova, A. Lacaita, G. Ripamonti, *New silicon epitaxial avalanche diode for single-photon timing at room temperature*, Electronics Letters, 24 (1988) 1476-1477.
[12] M. Ghioni, S. Cova, A. Lacaita, G. Ripamonti, *Epitaxial silicon single photon detector with reduced carrier diffusion effect and picosecond resolution*, 1987 International Electron Devices Meeting1987, pp. 452-455.
[13] M. Ghioni, A. Lacaita, S. Cova, G. Ripamonti, *20-ps Resolution Single-Photon Solid-State Detector*, March &-1iOr 1989 in Salt Lake Cityr Utah Volume 4, (1989) 194.
[14] F. Villa, D. Bronzi, Y. Zou, C. Scarcella, G. Boso, S. Tisa, A. Tosi, F. Zappa, D. Durini, S. Weyers, U. Paschen, W. Brockherde, *CMOS SPADs with up to 500 μm diameter and 55% detection efficiency at 420 nm*, Journal of Modern Optics, 61 (2014) 102-115.
[15] M. Liu, X. Bai, C. Hu, X. Guo, J.C. Campbell, Z. Pan, M.M. Tashima, *Low Dark Count Rate and High Single-Photon Detection Efficiency Avalanche Photodiode in Geiger-Mode Operation*, IEEE Photonics Technology Letters, 19 (2007) 378-380.
[16] H. Dautet, P. Deschamps, B. Dion, A.D. MacGregor, D. MacSween, R.J. McIntyre, C. Trottier, P.P. Webb, *Photon counting techniques with silicon avalanche photodiodes*, Appl. Opt., 32 (1993) 3894-3900.
[17] E. Dauler, P. Hopman, K. McIntosh, J. Donnelly, E. Duerr, R. Magliocco, L. Mahoney, K. Molvar, A. Napoleone, D. Oakley, *Scaling of dark count rate with active area in 1.06 μ m photon-counting In Ga As P/ In P avalanche photodiodes*, Applied physics letters, 89 (2006) 111102.
[18] P. Connolly, X. Ren, A. McCarthy, H. Mai, F. Villa, A. J. Waddie, M. R. Taghizadeh, A. Tosi, F. Zappa, R. K. Henderson, and G. S. Buller, *High concentration factor diffractive microlenses integrated with CMOS single-photon avalanche diode detector arrays for fill-factor improvement*, Appl. Opt. 59 (14) pp. 4488-4498 (2020).
[19] S. Pellegrini, R.E. Warburton, L.J.J. Tan, N. Jo Shien, A.B. Krysa, K. Groom, J.P.R. David, S. Cova, M.J. Robertson, G.S. Buller, *Design and performance of an InGaAs-InP single-photon avalanche diode detector*, IEEE Journal of Quantum Electronics, 42 (2006) 397-403.

[20] M. Stipčević, H. Skenderovic, D. Gracin, *Characterization of A Novel Avalanche Photodiode for Single Photon Detection in VIS-NIR Range*, 2010.
[21] G. Ribordy, J.-D. Gautier, H. Zbinden, N. Gisin, *Performance of InGaAs/InP avalanche photodiodes as gated-mode photon counters*, Appl. Opt., 37 (1998) 2272-2277.

# Chapter 4. Short-Wave Infrared Single-Photon Avalanche Diodes

## 4.1 InGaAs/InP SPADs

InGaAs/InP SPADs are a current state-of-the-art semiconductor single-photon detector which operate within the short-wave infrared. These device microstructures are usually epitaxially grown using metal organic chemical vapour deposition [1, 2]. InGaAs/InP SPADs are an example of a separate absorption grading charge multiplication avalanche diode, which because of their high multiplication and sensitivity they are an appealing detector for low signal measurements in the SWIR region [3] These devices are very similar in structure to the linear multiplication InGaAs/InP APDs commonly used in long-haul optical telecommunications. InGaAs is used as an absorption layer because of its sensitivity at a wavelength of 1550 nm which is a strategically important wavelength band as it can be used for minimum loss in optical fibres and corresponds to minimum loss is long-range free-space imaging. Operational wavelengths of InGaAs/InP SPAD detectors range from 900 to 1700 nm and they have detection efficiencies of up to 50 % with many devices providing under 100 ps timing resolution making them excellent in time gated applications like optical range finding in astronomy and metrology by time-of-flight measurements [4, 5]. These diodes have lower noise equivalent power levels than that available from commercial Ge diodes operated in Geiger mode, which are currently the main competition for InGaAs/InP devices in the infrared single-photon detection range [6]. Germanium and InGaAs/InP APDs utilize their narrow bandgaps to absorb near infrared photons. The downside is the production of a much higher level of thermal generated of carriers than one would typically get in, for example, a silicon-based device. Hence, for reducing the DCR to tolerable levels, devices must be cooled well below room temperature which can be impractical in some applications [7]. The NEP of InGaAs/InP SPADs can be as low as the order of $1x10^{-17}$ [5], these impressive values could be due to its lattice matched epitaxy, unlike, for example, Ge-on-Si SPADs which suffer from threading dislocations at the hetero-interface. The effect of dislocations on SPAD dark count rate is still the subject of ongoing research. It should also be noted, however, that InGaAs/InP epitaxy and fabrication is at a far more mature stage than that of Ge-on-Si APDs and SPADs which is the focus of this thesis.

One major drawback of InGaAs/InP based SPADs was initially that the maximum counting rates possible for these types of devices were limited by the phenomenon of afterpulsing, but there is ongoing research into methods that reduce the effects of afterpulsing [8-10]. One method of reducing the effects of afterpulsing is the use of sinusoidal gating which has resulted in InGaAs/InP APDs operating at impressive rates of 80 MHz with no afterpulsing evident. This effectively reduces the amount of charge per avalanche thus lowering the probability of traps being filled, reducing the effects of afterpulsing [11]. A typical microstructure of an InGaAs/InP SPAD is shown in Figure 4.1.

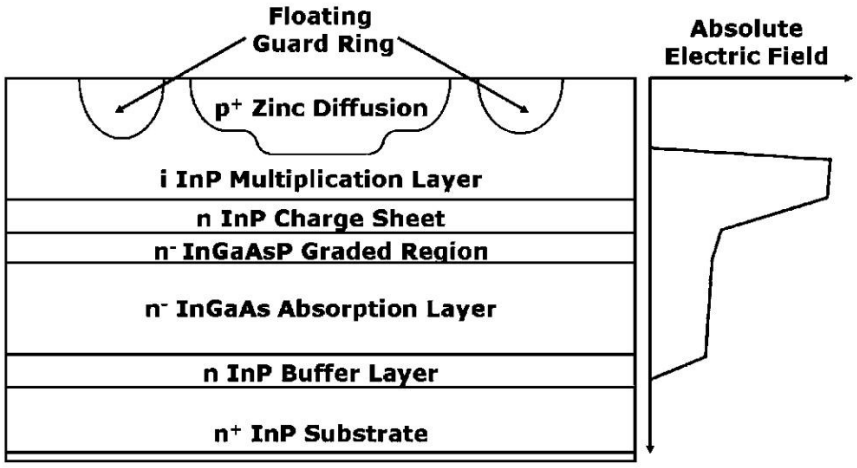


*Figure 4.1. InGaAs/InP SPAD featuring a p-doped zinc diffusion layer, intrinsic InP multiplication layer, a negatively doped InP charge sheet and slightly higher doped InGaAsP graded region and an InGaAs absorption layer, followed by an InP buffer layer and substrate. This design has floating guard rings to prevent preferential edge breakdown [12].*

The structure in Figure 4.1 is described by a number of authors [1, 8]. The device has a planar geometry, and the photon absorption takes place in the InGaAs layer giving the device the desired optical absorption range. The floating guard ring is used to reduce the likelihood of edge breakdown since they are designed to eliminate the electric field spikes at the edges of the main (central) junction. Edge breakdown will cause a lack of detection efficiency in the main detector junction, and is a serious issue in avalanche photodiode structures. Tunnelling takes place in the narrow-gap InGaAs at low electric field strengths, so to avoid this multiplication takes place within the InP region which has a larger bandgap. In this

device, hole injection is used since the impact ionisation coefficient of holes is greater than that of electrons in the InP multiplication layer. The InGaAsP layer is added to aid transport of the photogenerated hole across a large discontinuity in the different bandgaps of the materials.

Although super conducting nanowires are able to operate within the SWIR region with higher efficiencies than InGaAs/InP SPADs, their lower costs and better mobility has meant they are the detector of choice in many applications. InGaAs/InP SPADs have facilitated long distance QKD [13] as well as high-performance imaging array cameras for single-photon depth imaging applications [14] and even depth imaging over long distances, has been attempted using InGaAs/InP detectors [4, 15, 16]. Utilising LIDAR, which is the preferred technique for remote sensing, and time correlated single-photon counting (TCSPC). This process involved illuminating a target with a pulsed laser source and using time-of-flight data from the returned photons to build a 3D image of the scene. Images were produced in low light with excellent surface-to-surface resolution. TCSPC was used to collect both depth and intensity information when building up accurate 3D images. At 325 metres range in daylight using 1550 nm wavelength radiation, high-resolution depth and intensity images were achieved with as little as 1 mW laser power. By working with 1550 nm illumination, solar radiation, which contributes most of the background level, is decreased considerably in this long wavelength regime. An example of the excellent depth resolution achieved using InGaAs/InP SPAD detectors in a scanning LIDAR system can be seen in Figure 4.2.

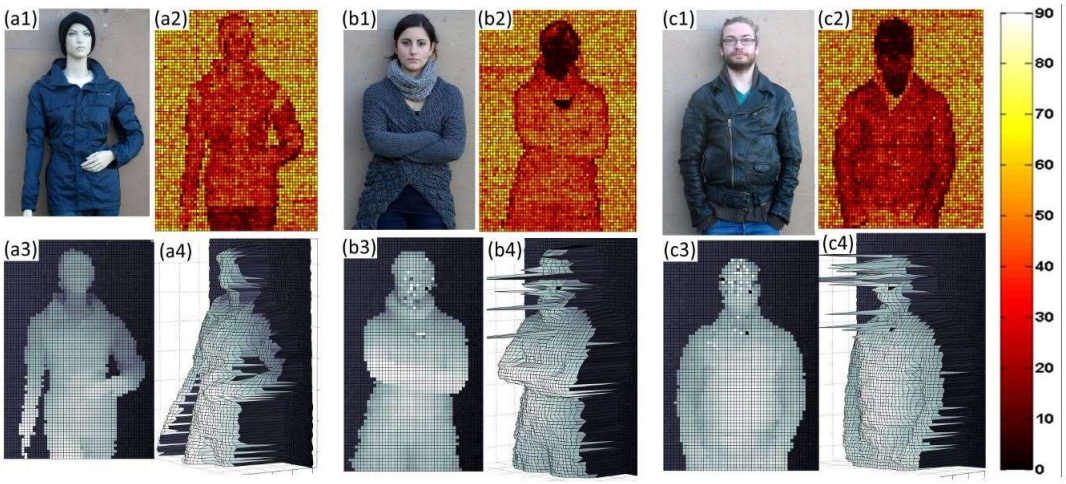


*Figure 4.2. An example of the results obtained at 325 m range and 1550 nm wavelength using an InGaAs/InP SPAD detector in a scanning LIDAR transceiver. (a1), (b1) and (c1) are photographs using 5 ms per pixel acquisition time. (a2), (b2) and (c2) show the intensity of returned photons using colour bar. The bottom row of images show depth intensity data where shading represents the depth [4].*

InGaAsSb/GaSb SPADs have also recently become an interesting area of research; GaSb and InAs based structures allow a variety of narrow gap layers to be grown lattice matched. This lattice matching allows for separate absorption and multiplication region heterostructures, which takes advantage of the absorption properties of one material and the multiplication properties of another. Unlike in InGaAs/InP devices used in TCSPC which were produced by organic chemical vapour deposition, InGaAsSb/GaSb devices have been produced by molecular beam epitaxy and dry and wet etched [17]. InGaAsSb/GaSb APDs have successfully been demonstrated in 2015 by A.R.J. Marshall *et al.* [18]. The concept can be applied to other absorber materials and therefore longer wavelengths. InAs has been demonstrated detecting wavelengths up to 3.5 µm showing potential for mid-range infrared photon detection [19]. Although these materials seem promising this technology is generally at a very immature stage compared to InGaAs/InP SPAD and APD detectors [20].

To summarise, the single-photon detection efficiency of InGaAs/InP SPADs is typically in the order of 10 % to 50 % and Peltier-cooled operation makes them potential candidates for many short-wave infrared single-photon applications. Unfortunately, these devices suffer from excessive afterpulsing, a phenomenon that can lead to increased dark count rates and reduced maximum count rates, but this can be addressed with gating techniques and different temperature operation. They cannot be easily integrated into silicon circuitry which makes their incorporation into existing technology more expensive and less practical.

### 4.2 Germanium Avalanche Photodetectors

An alternative absorption material for detection of short-wave infrared light is germanium, which has a cut-off wavelength of approximately 1600 nm at room temperature in commercially available devices. Germanium is an indirect band gap semiconductor however, the narrow direct bandgap which gives germanium its SWIR wavelength detection also causes band-to-band tunnelling, resulting in high DCRs and making all-germanium devices unsuitable in many applications [21, 22]. However recent research which has shown photon detection up to 2000 nm wavelength in lab testing using germanium [23], was achieved using a separate absorption-charge-multiplication (SACM) avalanche photodetector, with a germanium layer grown on silicon waveguides, utilising both germanium's absorption range and silicon's multiplication properties. Another option for providing this is growing Ge-on-Si devices. Ge-on-Si SPADs are a promising technology, being highly responsive in the range which sweeps from visible into SWIR, and with potential to be compatible with silicon CMOS circuitry. The benefit of using Ge-on-Si is retaining the compatibility of Si based detectors whilst increasing the spectral range. This would then allow detectors for use with low-loss optical fibre telecommunications, as well as free space applications whilst remaining within eye-safe thresholds. One disadvantage of using Ge-on-Si is the large 4 % lattice mismatch between materials. This leads to dislocations and these act as recombination centres for carriers, reducing the device efficiency and providing traps which contribute to the dark count rate and overall noise of the devices.

### 4.3 Bandstructure Comparison of InGaAs/InP and Ge-on-Si

Using different absorption and multiplication materials allows us to utilize the bandgap of one material and subsequently the detection wavelength, whilst keeping the multiplication efficiency of another. However, there can be issues with discontinuity in the bandgap of the two materials. If the bandgap of the absorber and the multiplication region are different the carrier must be able to flow through without having to overcome a large energy gradient to produce an efficient SPAD. For example, in a Ge-on-Si SPAD, the electron is able to drift from the Ge absorber into the Si down the energy gradient into multiplication region, there is no barrier for the electron movement as can be seen in Figure 4.3 (b). Whereas in an InGaAs/InP SPAD the photogenerated holes in the InGaAs must overcome a large energy barrier to enter the InP multiplication region. In Figure 4.3 (a), the band-structure of a reverse-biased InGaAs/InP SPAD with a grading layer is compared to the bandstructure of Ge-on-Si SPADs. In a Ge-on-Si SPAD absorption only takes place within the germanium and therefore the bandgap of the silicon is largely irrelevant to the absorption process. Because there is no barrier for the electrons to overcome when moving from the absorption region to the multiplication region, the device is simpler and does not need grading layers, unlike InGaAs/InP SPADs. The discontinuity in the bandgap at the heterosurface comes from the different bandgaps of Ge and Si. Germanium the direct bandgap of germanium is 0.8 eV at room temperature [24]. This corresponds to a wavelength of approximately 1550 nm but because the bandgap increases at lower temperatures, our experiments were performed with a pulsed laser with a wavelength of 1310 nm used for excitation within the germanium to ensure the initial photon absorption could take place [25]. It is still possible in theory to get a low level of absorption at longer wavelengths such as 1850 nm at room temperature corresponding to a 0.67 eV bandgap but the devices will exhibit less efficiency as this is the indirect bandgap for germanium [26]. And as with all indirect bandgap semiconductors it therefore requires a phonon for excitation to take place.

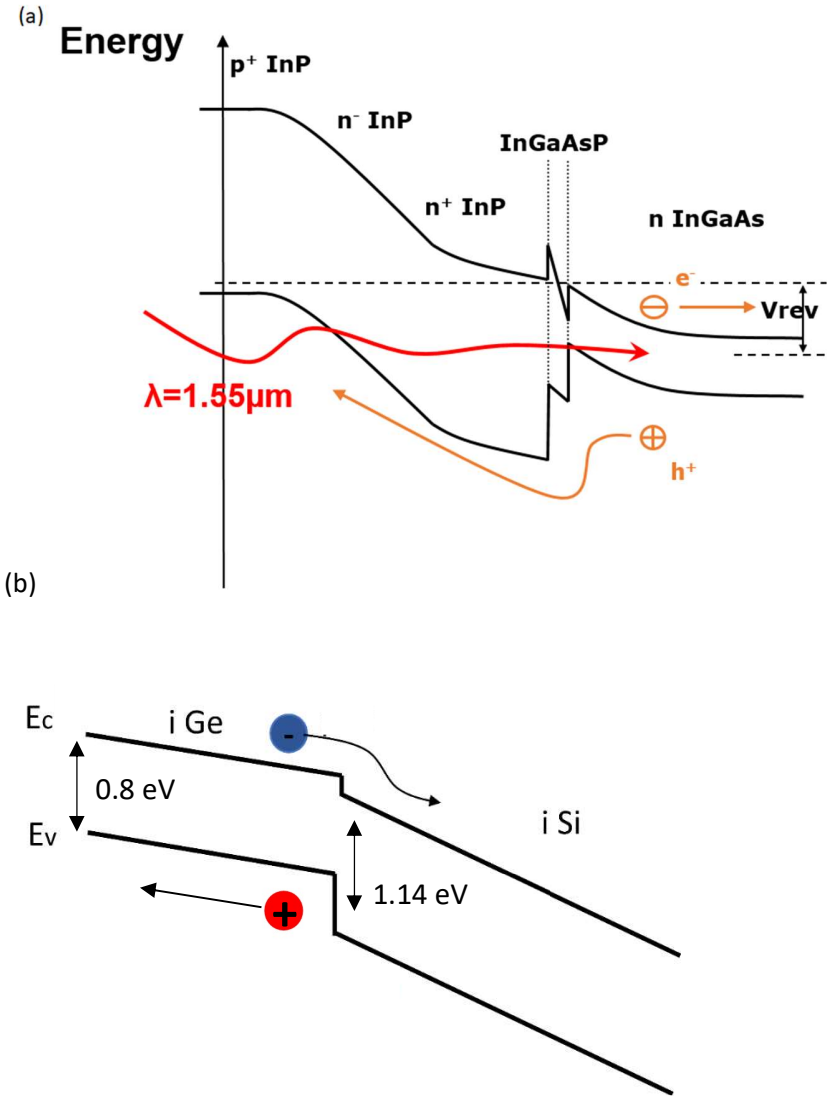


*Figure 4.3.(a) The band-structure for a reverse-biased InGaAs/InP SPAD depicting the energy barrier a photo-generated hole must overcome to reach the multiplication region [14].(b) The band-structure of a Ge-on-Si SPAD where the photo-generated electron is able to drift from the germanium absorber to the silicon multiplication region since there is no barrier [24, 27].*

At room temperature Germanium has an absorption coefficient of approximately 8000 $cm^{-1}$ for an incident photon at 1310 nm wavelength but at 1550 nm the absorption coefficient drops to approximately 2500 $cm^{-1}$ [26]. The variation of absorption with respect to wavelength is shown in Figure 4.4.

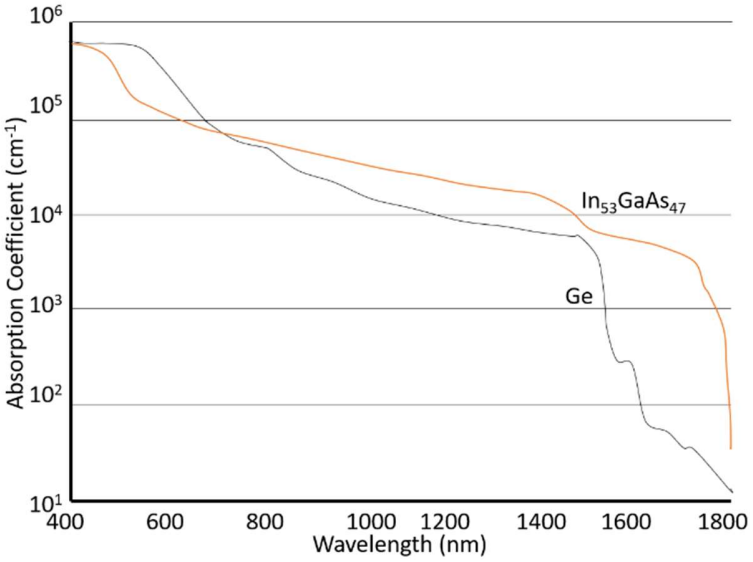


*Figure 4.4. Absorption coefficient dependence on wavelength of Ge and $In_{53}GaAs_{47}$ at 300 K [28].*

In the Ge-on-Si SPAD the photon passes through the contact layer and straight into the absorbing layer whereas in the InGaAs/InP SPAD the photon must travel through multiple layers to reach the absorbing medium. In the InGaAs/InP SPAD, impact ionisation involves the photo-generated hole reaching the multiplication region after traversing a barrier, and then gaining sufficient kinetic energy in the high electric field to initiate an impact ionisation event, releasing a secondary electron hole pair. As stated previously, these secondary carriers are then accelerated in the electric field causing further impact ionisation events initiated by both electrons and holes, creating an avalanche of carriers. In the Ge-on-Si SPAD the initial electron drifts into the Si layer whereas in the InGaAs/InP SPAD a hole must overcome a barrier to get into the InP multiplication region. To assist with this barrier, one or more grading layers are used between the InGaAs absorber and the InP multiplication region, which are layers composed of materials with an intermediate bandgap, which can act as a step for the carriers to traverse. This makes InGaAs/InP devices more expensive and difficult to produce. This is shown more clearly in the bandgap diagram Figure 4.3 (a). If the field in the multiplication layer is sufficiently high, then the avalanche current can be self-sustaining, resulting in a high current level which, in principle, will not stop unless external stimuli are applied.

### 4.4 Ge-on-Si SPADs with Mesa Geometry

In 2011 Lu *et al* produced mesa geometry Ge-on-Si APDs which operated in Geiger mode and were tested at a wavelength of 1310 nm, and reported to have achieved a maximum SPDE of 14 % at 200 K, and a minimum jitter value of only 117 ps [29]. However, it should be noted that the authors method used 1 photon per pulse which has likely led to an over estimation of SPDE`. Typically, a TCSPC set-up would use significantly fewer than 1 photon per pulse as this is only the average number of photons per pulse and the distribution of actual photons per pulse may end up higher than 1 in some cases. Despite this, it still formed a promising starting point for fabrication of Ge-on-Si mesa devices [30]. Lu *et al.* also found that the afterpulsing in this Ge-on-Si SPAD was significantly less than that for InGaAs/InP based SPADs operating under similar conditions, they believed this was a result of the high-quality Si multiplication layer. Following on from this, research performed by Warburton *et al.* showed that a mesa Ge-on-Si device at 100 K, again at 1310 nm wavelength and an excess bias of 10 % could achieve a SPDE of 4 %, and higher jitter of 300 ps [31]. However, under those conditions the dark count rate was approximately $10^6$-$10^7$ counts per second which is at least one order of magnitude smaller than the $10^8$ dark count rates reported by Lu *et al.*[29]. It was believed the dark count rate of these devices could have been due to surface defects from the mesa geometry shape. At 1550 nm wavelength, at a temperature of 125 K and 6 % excess bias, a much lower SPDE of 0.15 %, giving it a much longer detection range than a Si device, so whilst the SPAD detectors described by Warburton *et al.[31]*, showed a larger jitter and smaller SPDE, the design and fabrication method used showed some promise in lowering the DCR and longer wavelength detection. It was believed the high dark count rate of these devices was likely due to surface effects from the mesa geometry shape. More recently, The University of Glasgow and collaborators fabricated a slightly different design mesa geometry Ge-on-Si SPAD from those previously used, and this design for the mesa geometry SPAD is shown in Figure 4.5; The Si charge sheet extends the full width of the Ge absorption layer, with their edges aligned which exposed their sidewalls and leads to an interaction between carriers and surface defects. Mesa geometry SPADs therefore have high electric field concentrations at the edges of the boundary between the multiplication layer and the charge sheet when compared to a planar SPAD [32].

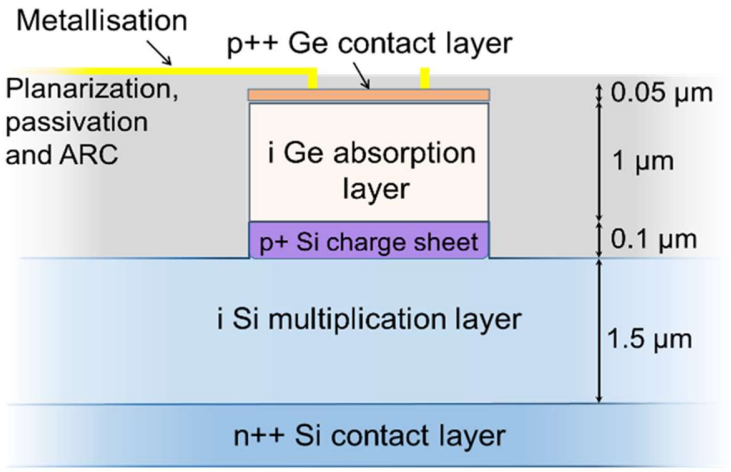


*Figure 4.5. A mesa geometry Germanium-on-Silicon SPAD cross section. With same width Ge absorption layer and Si charge sheet, an intrinsic Si multiplication layer and a heavily doped negative Si contact layer.*

The mesa geometry Ge-on-Si SPAD also proved to have high DCR at 78 K of over $10^5$ counts per second (cps), as well as failing to survive temperature cycling. Waveguide technology is a potential avenue for avoiding the higher DCR associated with mesa geometry SPADs, and to date, Ge waveguide photodiodes that are compatible with CMOS technology have been reported [33]. Waveguides can reduce DCR as they can be made with a smaller volume than a normal incidence circular device whilst maintaining a long interaction length for optical absorption. The smaller volume will lead to a lower DCR whilst maintaining a high detection efficiency. Waveguide-coupled APDs [34] have also been developed and are able to operate at over 1500 nm wavelength. More recently, a waveguide Ge-on-Si SPAD was reported by Martinez *et al*. [35], with a SPDE of 5.27 % at a wavelength of 1310 nm at 80 K, and a DCR of the order of $10^5$ cps. So, although promising, none of these devices have demonstrated results that are close to the InGaAs/InP SPADs, having high DCRs and making them unsuitable in many applications.

### 4.5 Ge-on-Si SPADs with Planar Geometry

Another option for reducing the surface defects and their contribution to the DCR of the device was a planar geometry design, which showed potential in improving detector performance. This is the focus of Chapter 5, which presents state of the art results for small area Ge-on-Si planar geometry devices. However, unlike InGaAs/InP SPADs, the planar geometry Ge-on-Si SPADs required a buried charge sheet. This is a consequence of the Ge being grown on Si, and not the other way around. This necessitated the form of design shown in Figure 4.6, which relied on ion implantation and regrowth after the Si multiplication layer. This is considerably more complex than the fabrication processes required for the mesa Ge-on-Si SPADs.

The planar geometry arrangement allows the germanium absorber to be much wider than the charge sheet and these sidewalls are used to prevent carriers within the material entering the high electric field at the edges of the charge sheet, as seen in Figure 4.7 (a). This design reduces the high electric field on the charge sheet sidewalls and reduces the likelihood of edge breakdown. Edge breakdown occurs when the device breaks down at electric field "hot spots" near the edges of the device, where the photons are not incident. These "hot spots" are considerably worse in mesa geometry design SPADs as can be seen in Figure 4.7 (b). This is undesirable as ideally the breakdown should take place centrally allowing for the most efficient avalanche. Keeping the electric field low at the sidewall edges also reduces the DCR. Hence the planar geometry and increases the device single-photon detection efficiency and reduces the dark count rate.

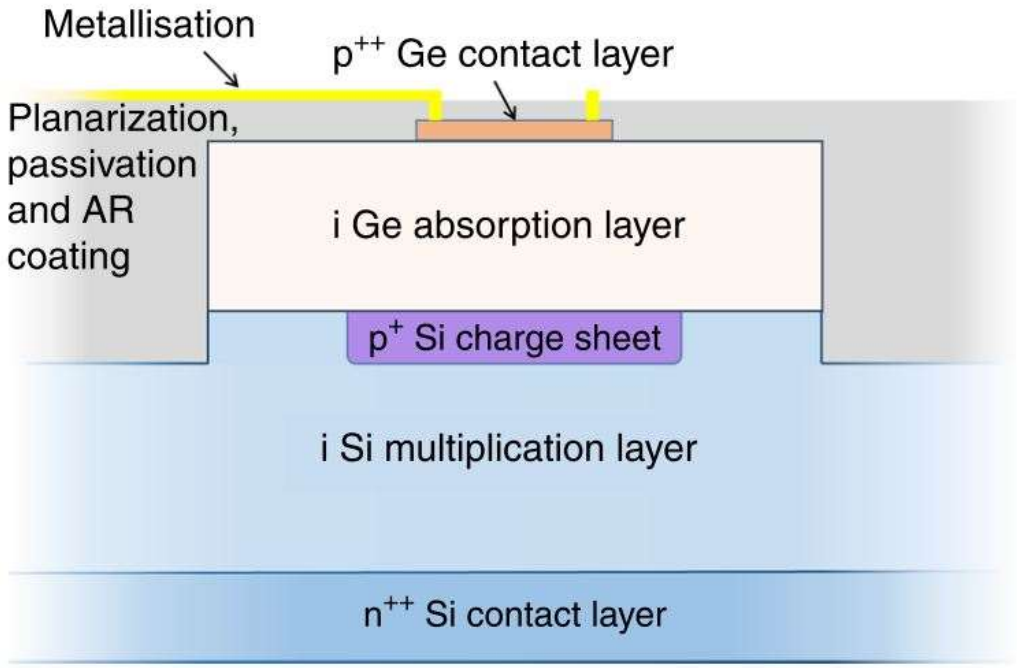


*Figure 4.6. Planar geometry Ge-on-Si SPAD cross section. Schematic showing one of many potential designs for a single-photon avalanche diode with a Ge absorption layer and a Si charge sheet, multiplication layer and negative contact [32].*

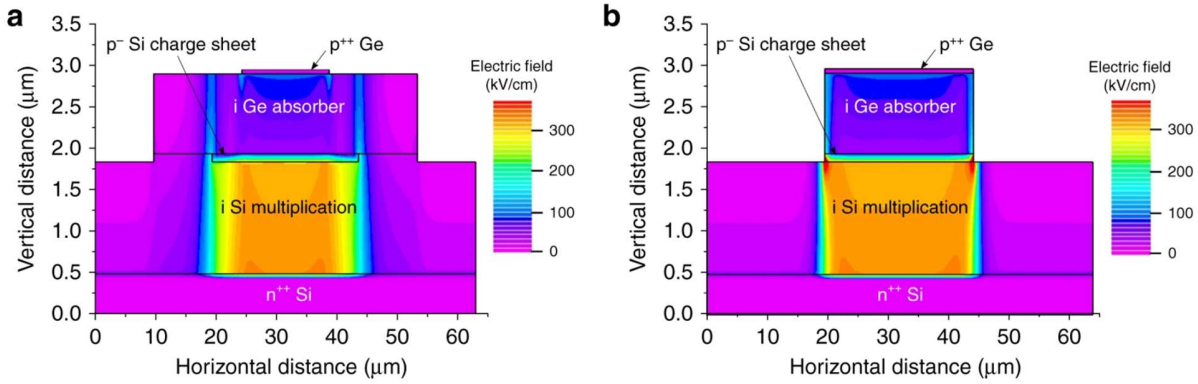


*Figure 4.7. (a) Planar Ge-on-Si SPAD design and (b) mesa Ge-on-Si SPAD electric field strength modelled using SILVACO software at 5 % excess bias [32]*

In 2019 Vines *et al*. improved on the results shown in Warburton's experiment by demonstrating planar geometry Ge-on-Si detectors which detect up to 38% efficiency at 125K detecting 1310 nm wavelength photons [32]. The new planar design, although more difficult to manufacture, showed an impressive increase in efficiency and significant reductions in dark count rate. The Ge-on-Si SPADs used by Vines *et al*. were fabricated by the University of Glasgow and are thin junction SPADs, which comes with many advantages for their intended applications. Thin junction SPADs do not need a cooling system and operate at much lower breakdown voltages, approximately lower than 50 V which makes them easier to use. There is also much improved timing resolution but typically lower SPDE than thick junction SPADs [36]. Vines et al. showed that under limited conditions, that Ge-on-Si SPADs have lower afterpulsing than InGaAs/InP SPADs, as can be seen in Figure 4.8. Afterpulsing in Ge-on-Si SPADs will be described in more detail in the following Chapter.

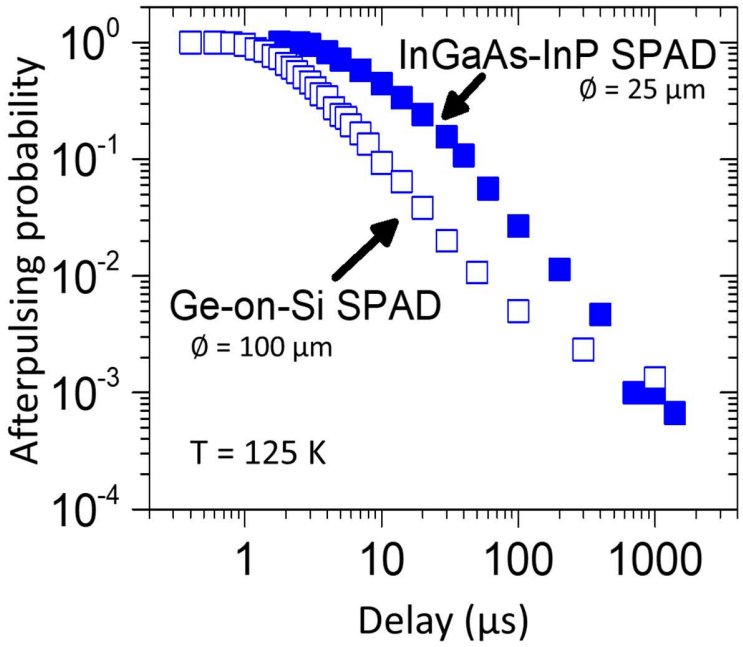


*Figure 4.8. Comparison of afterpulsing between a 100 µm diameter Ge-on-Si SPAD and a 25 µm commercially available InGaAs/InP SPAD at λ = 1310 nm and operated at a single-photon detection efficiency of 17% and a temperature of 125 K [32].*

Germanium and InGaAs both absorb up to a similar wavelength range, Figure 4.4. But InGaAs/InP has been proven to work at Peltier cooled temperatures whereas previous research performed on Ge-on-Si SPADs has only shown competitive single photon detection efficiencies at below Peltier cooling temperatures [32].

To summarise, Ge-on-Si SPADs are a relatively new technology with the potential to provide and alternative method to InGaAs/InP SPADs for single-photon detection in the SWIR with lower afterpulsing, lower manufacturing costs and the added benefit of being integrated with existing Si circuitry.

**References**

[1] S. Pellegrini, R.E. Warburton, L.J.J. Tan, N. Jo Shien, A.B. Krysa, K. Groom, J.P.R. David, S. Cova, M.J. Robertson, *G.S. Buller, Design and performance of an InGaAs-InP single-photon avalanche diode detector*, IEEE Journal of Quantum Electronics, 42 (2006) 397-403.

[2] X.J. Mark Itzler, Mark Entwistle, *Power law temporal dependence of InGaAs/InP SPAD afterpulsing*, Journal of Modern Optics, (2012).

[3] Y. Zhao, D. Zhang, L. Qin, Q. Tang, R. Wu, J. Liu, Y. Zhang, H. Zhang, X. Yuan, W. Liu, *InGaAs–InP avalanche photodiodes with dark current limited by generation-recombination*, Opt. Express, 19 (2011) 8546-8556.

[4] A. McCarthy, X. Ren, A. Della Frera, N.R. Gemmell, N.J. Krichel, C. Scarcella, A. Ruggeri, A. Tosi, G.S. Buller, *Kilometer-range depth imaging at 1550 nm wavelength using an InGaAs/InP single-photon avalanche diode detector,* Opt. Express, 21 (2013) 22098-22113.

[5] M. Liu, C. Hu, X. Bai, X. Guo, J.C. Campbell, Z. Pan, M.M. Tashima, High-*Performance InGaAs/InP Single-Photon Avalanche Photodiode*, IEEE Journal of Selected Topics in Quantum Electronics, 13 (2007) 887-894.

[6] T.P. Lee, *Long-wavelength photodiodes for optical fiber communications*, pp. C2-3.

[7] A. Tosi, A.D. Mora, F. Zappa, S. Cova, *Germanium and InGaAs/InP SPADs for single-photon detection in the near-infrared*, SPIE2007.

[8] J. Zhang, M.A. Itzler, H. Zbinden, J.-W. Pan, *Advances in InGaAs/InP single-photon detector systems for quantum communication*, Light: Science & Applications, 4 (2015) e286-e286.
[9] R.E. Warburton, M. Itzler, G.S. Buller, *Free-running, room temperature operation of an InGaAs/InP single-photon avalanche diode*, Applied Physics Letters, 94 (2009) 071116.
[10] C. Scarcella, G. Boso, A. Ruggeri, A. Tosi, *InGaAs/InP Single-Photon Detector Gated at 1.3 GHz With 1.5% Afterpulsing*, IEEE Journal of Selected Topics in Quantum Electronics, 21 (2015) 17-22.
[11] N. Namekata, S. Inoue, *Afterpulsing-free 80mhz single-photon detection at 1550 nm using an ingaas/inp avalanche photodiode operated with sinusoidal gating*, Optical Society of America, pp. IC6_2.
[12] G. Buller, R. Collins, *Single-photon generation and detection*, Measurement Science and Technology, 21 (2009) 012002.
[13] B. Korzh, C.C.W. Lim, R. Houlmann, N. Gisin, M.J. Li, D. Nolan, B. Sanguinetti, R. Thew, H. Zbinden, *Provably secure and practical quantum key distribution over 307 km of optical fibre*, Nature Photonics, 9 (2015) 163-168.
[14] X. Jiang, M. Itzler, K. O'Donnell, M. Entwistle, M. Owens, K. Slomkowski, S. Rangwala, *InP-Based Single-Photon Detectors and Geiger-Mode APD Arrays for Quantum Communications Applications*, IEEE Journal of Selected Topics in Quantum Electronics, 21 (2015) 5-16.
[15] R. Tobin, A. Halimi, A. McCarthy, X. Ren, K.J. McEwan, S. McLaughlin, G.S. Buller, *Long-range depth profiling of camouflaged targets using single-photon detection*, Optical Engineering, 57 (2017) 1-10, 10.
[16] A.M. Pawlikowska, A. Halimi, R.A. Lamb, G.S. Buller, *Single-photon three-dimensional imaging at up to 10 kilometers range*, Opt. Express, 25 (2017) 11919-11931.
[17] J.O. Kim, N.T. Dai, J. Hwang, S.J. Lee, *Fabrication and characterization of InGaAsSb/GaSb photodetectors for SWIR detection*.
[18] A.R.J. Marshall, A.P. Craig, C.J. Reyner, D.L. Huffaker, *GaAs and AlGaAs APDs with GaSb absorption regions in a separate absorption and multiplication structure using a hetero-lattice interface*, Infrared Physics & Technology, 70 (2015) 168-170.

[19] A. Marshall, C. Tan, M. Steer, J. David, *Electron dominated impact ionization and avalanche gain characteristics in InAs photodiodes*, Applied Physics Letters, 93 (2008) 111107.
[20] A.P. Craig, M. Jain, L. Meriggi, T. Cann, A. Niblett, X. Collins, A.R.J. Marshall, *Extended short-wave infrared linear and Geiger mode avalanche photodiodes*, based on 6.1 Å materials, Applied Physics Letters, 114 (2019) 053501.
[21] F. Thorburn, X. Yi, Z. Greener, J. Kirkoda, R. Millar, L. Huddleston, D. Paul, G. Buller, *Ge-on-Si single-photon avalanche diode detectors for short-wave infrared wavelengths*, Journal of Physics: Photonics, (2021).
[22] A. Lacaita, S. Cova, F. Zappa, P.A. Francese, *Subnanosecond single-photon timing with commercially available germanium photodiodes*, Opt. Lett., 18 (1993) 75-77.
[23] R. Anthony, D.E. Hagan, D. Genuth-Okon, L.M. Maestro, I.F. Crowe, M.P. Halsall, A.P. Knights, *Extended Wavelength Responsivity of a Germanium Photodetector Integrated With a Silicon Waveguide Exploiting the Indirect Transition*, IEEE Journal of Selected Topics in Quantum Electronics, 26 (2020) 1-7.
[24] G. Ben, *Solid state electronic devices*, Englewood Cliffs, NJ, 2000.
[25] U.o. Reading, Infrared Multilayer Laboratory - Germanium, Reading, 2020.
[26] K. Wada, *Electronics and photonics convergence on Si CMOS platform*, Proceedings of SPIE - The International Society for Optical Engineering, (2004).
[27] C. VandeWalle, M.d.P. Martin, *Theoretical calculations of heterojunction discontinuities in the Si/Ge system*, Physical review. B, Condensed matter, 34 8 (1986) 5621-5634.
[28] O.I. Dosunmu, D.D. Cannon, M.K. Emsley, L.C. Kimerling, M.S. Unlu, *High-speed resonant cavity enhanced Ge photodetectors on reflecting Si substrates for 1550-nm operation*, IEEE Photonics Technology Letters, 17 (2004) 175-177.
[29] Z. Lu, Y. Kang, C. Hu, Q. Zhou, H.-D. Liu, J.C. Campbell, *Geiger-mode operation of Ge-on-Si avalanche photodiodes,* IEEE Journal of Quantum Electronics, 47 (2011) 731-735.
[30] Z. Lu, Y. Kang, C. Hu, Q. Zhou, H. Liu, J.C. Campbell, *Geiger-Mode Operation of Ge-on-Si Avalanche Photodiodes, IEEE Journal of Quantum Electronics*, 47 (2011) 731-735.

[31] R.E. Warburton, G. Intermite, M. Myronov, P. Allred, D.R. Leadley, K. Gallacher, D.J. Paul, N.J. Pilgrim, L.J. Lever, Z. Ikonic, *Ge-on-Si single-photon avalanche diode detectors: design, modeling, fabrication, and characterization at wavelengths 1310 and 1550 nm*, IEEE Transactions on Electron Devices, 60 (2013) 3807-3813.
[32] P. Vines, K. Kuzmenko, J. Kirdoda, D.C.S. Dumas, M.M. Mirza, R.W. Millar, D.J. Paul, G.S. Buller, *High performance planar germanium-on-silicon single-photon avalanche diode detectors,* Nature Communications, 10 (2019) 1086.
[33] C.T. DeRose, D.C. Trotter, W.A. Zortman, A.L. Starbuck, M. Fisher, M.R. Watts, P.S. Davids, *Ultra compact 45 GHz CMOS compatible Germanium waveguide photodiode with low dark current*, Opt. Express, 19 (2011) 24897-24904.
[34] N.J.D. Martinez, C.T. Derose, R.W. Brock, A.L. Starbuck, A.T. Pomerene, A.L. Lentine, D.C. Trotter, P.S. Davids, *High performance waveguide-coupled Ge-on-Si linear mode avalanche photodiodes*, Opt. Express, 24 (2016) 19072-19081.
[35] N.J.D. Martinez, M. Gehl, C.T. Derose, A.L. Starbuck, A.T. Pomerene, A.L. Lentine, D.C. Trotter, P.S. Davids, *Single photon detection in a waveguide-coupled Ge-on-Si lateral avalanche photodiode*, Opt. Express, 25 (2017) 16130-16139.
[36] K. Zang, X. Jiang, Y. Huo, X. Ding, M. Morea, X. Chen, C.-Y. Lu, J. Ma, M. Zhou, Z. Xia, Z. Yu, T.I. Kamins, Q. Zhang, J.S. Harris, *Silicon single-photon avalanche diodes with nano-structured light trapping*, Nature Communications, 8 (2017) 628.

# Chapter 5. Planar Geometry Ge-on-Si SPADs

## 5.1 Introduction

Ge-on-Si SPADs are an exciting and innovative candidate for single-photon detector technology for picosecond timing resolved measurement in the SWIR region. As mentioned in previous Chapters, there are many applications that would benefit from improved performance SPADs operating in the SWIR range, such as long-range LIDAR and fibre-based quantum communications [1-4]. However, there are no semiconductor-based single-photon detectors which perform as well as silicon SPADs, which are now a well-established commercially available technology and are commonly used for single-photon detection at wavelengths within the visible and near infrared spectral region This chapter begins by presenting the background research done on Ge-on-Si SPADs and goes on to describe the fabrication methods, device characterisation and future opportunities presented by Ge-on-Si SPADs operating in the short-wave infrared. The concept of the photon was initially proposed by both Planck [5, 6] and Einstein [7] in the 20$^{th}$ century and since then the research into both single-photon sources and detectors has expanded considerably. As the number of applications utilising single-photons grows the desire for high performance single-photon detectors also increases. Primarily biophotonics was the main area of interest for single-photon detectors particularly in the visible and NIR wavelength ranges [8-11]. However, more recently quantum technology has become a major area of interest and motivation behind more current research into single-photon detection and production [12]. The field of quantum technology promises to have a large scientific impact in the near future for sensing, metrology communications and processing. Quantum information applications involve the manipulation and measurement of quantum particles usually photons which can be used to encode and hence transmit data. The most developed area of quantum information is quantum key distribution [13-15], which provides a method for safely and securely communicating information, prototype quantum key distribution systems are now commercially available [16, 17]. Another area of quantum information that appears promising is linear optical quantum computing which is less mature than quantum key distribution but could greatly improve the efficiency of computational tasks that are currently carried out using traditional methods [12, 18, 19]. Linear optical quantum computing places extremely high standards on the optical components in the system being used and

encompasses issues with integrating multiple single-photon detectors, because of this it is expected to be a long term endeavour to reach a point where this application is commercially viable [18, 20]. Consequently, there has been a considerable investment into the development of single-photon detectors in order to support the many emerging applications in quantum information. However, quantum information is not the only driving force behind single-photon detection research, other examples of applications include; optical fibre characterisation which requires optical time domain reflectometry [21], environmental monitoring and other remote sensing applications [22]. LIDAR and 3D imaging particularly benefit from high detection efficiency and low temporal jitters, of the order of hundreds of picoseconds, which commercially available SPADs provide [23-29]. This is especially beneficial when used in harsh environments, such as over long distances and through atmospheric obscurants [23, 27]. In many applications it is particularly beneficial to operate at wavelengths in the SWIR spectral region. For example, low loss fibre telecommunications 1310 nm and 1550 nm wavelengths are the low-loss spectral windows, with 1550 nm typically used for long-haul telecommunications transmission. Atmospheric transmission is also enhanced because there is less scattering from atmospheric particles within the SWIR spectral range and much lower solar background compared to shorter wavelengths, which is particularly beneficial when used in free-space LIDAR and 3D imaging [1, 30-32]. Another benefit of this spectral range is the eye-safety threshold being higher in SWIR than it is in the visible regime and so more laser power can be used in free-space applications, which gives the potential to work over longer ranges [33].

Research into Ge-on-Si SPADs is motivated by the need for improved single-photon detectors which operate at wavelengths over 1 μm with the ideal combination of high efficiency, low noise, low afterpulsing effects and Peltier cooling compatible temperature operation. All-germanium homojunction SPADs have been reported in laboratory experiments but the major issue associated with these devices is that the direct bandgap of germanium is quite narrow, ~ 0.8 eV, which means that there is high photon detection sensitivities in the SWIR, however this also leads to considerable band-to-band tunnelling, resulting in high DCRs which, in turn, severely limits the sensitivity attainable by these devices [34, 35]. InGaAs/InP SPADs operate with high efficiency in the SWIR region and

are used in applications such as QKD and LIDAR but are incompatible with existing CMOS technology and suffer from the phenomenon of afterpulsing which restricts the maximum count rate achievable [36-43]. Nonetheless, several manufacturers offer detector modules based on InGaAs/InP SPADs, and these have been used in a range of single-photon system demonstrations in recent years such as time-of-flight depth imaging [44] and quantum communication systems [45].

In order to address many of the drawbacks, a useful alternative to these existing detection technologies is to utilize Ge as an absorber with a Si multiplication layer. The bandgap of Ge provides efficient absorption at wavelengths throughout the visible, near infrared and parts of the short-wave infrared up to a cut-off wavelength of approximately 1600 nm at room temperature. In 2002 Loudon *et al*. enhanced the efficiency of Si photon-counting detectors at 1210 nm wavelength by using SiGe absorbing layers [46], Ge-on-Si SPADs employ a separate absorption, charge and multiplication (SACM) design which is used commonly with InGaAs/InP APDs and SPADs [46]. These detectors would have the potential to operate in the range of temperatures accessible by Peltier coolers and would operate with high efficiency courtesy of the Si multiplication region. They could operate well into the SWIR spectral region, owing to the Ge absorber, thus providing a useful alternative to InGaAs/InP based SPADs for detection in this spectral range. This Chapter will present the characterisation results for planar geometry Ge-on-Si SPADs and analyse the single-photon detector performance for applications in the SWIR.

The growth of Ge layers on Si mesa geometry Ge-on-Si SPADs appears to be a fruitful area of research when reported by R.E. Warburton *et al.* in 2013. The authors reported a 4 % single-photon detection efficiency (SPDE) and lowest reported NEP for a Ge-on-Si SPAD of $1 \times 10^{-14}$ $WHz^{-1/2}$ at 1310 nm and a much lower SPDE of approximately 0.15 % for a wavelength of 1550 nm [47]. When compared to A. Tosi *et al* who was able to characterise commercially available Ge SPADs in 2007 with a detection efficiency of 30 % at $\lambda = 1310$ nm, there is clearly room for improvement in the detection efficiency for researchers when producing Ge-on-Si devices [48, 49]. However in 2019 Vines *et al*. reported high performance germanium-on-silicon SPADs with efficiencies up to 38 % at

125 K allowing for incorporation into a LIDAR system where images were produced showing toy cars with sub-millimetre depth resolution taken at a distance of 0.4 m as seen in Figure 5.1 using a planar geometry Ge-on-Si SPAD [50]. However, the 1 µm thickness of Ge absorption layer used by Vines *et al*. theoretically absorbs less than 50 % of light at a wavelength of 1310 nm.

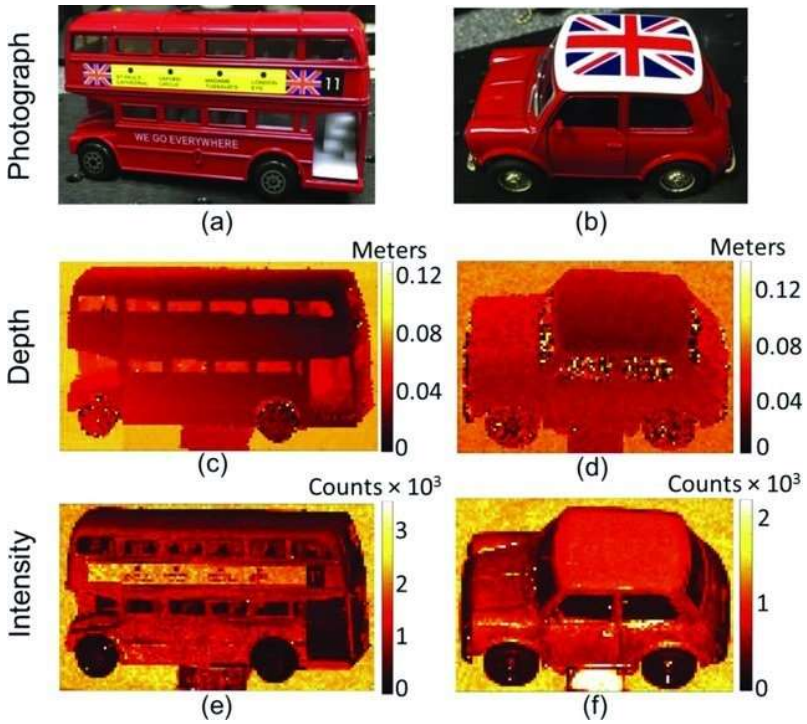


*Figure 5.1. Depth and Intensity profile of (a) double decker toy bus and (b) a Mini Cooper model. The measurements were performed in a dark laboratory environment at a stand-off distance of 0.4 m using a planar Ge-on-Si SPAD [50].*

The fabrication process for the planar geometry detector is given in detail by Dr Jaroslaw Kirdoda in his Thesis 'Germanium on Silicon Single Photon Avalanche Detectors' [51], and was used to produce the planar Ge-on-Si SPADs which form the subject of this Chapter. The method is summarised in Section 5.2 below.

This Chapter describes the fabrication and design processes as well as further investigating the full time-correlated single-photon counting (TCSPC) characterisation of 26 µm and 50 µm diameter charge sheet planar Ge-on-Si SPADs with a 1 µm thick Ge absorber layer and a 15 µm superpixel (this will be fully described in section 5.2), this includes IV results, SPDE, DCR, as well as jitter and NEP results. Ge-on-Si SPADs with thicker Ge layers, up to 2 µm were fabricated for the first time and tested for IV characteristics and photoresponsivity up to 1800 nm. With the aim of achieving operational wavelengths over 1500 nm. These results have subsequently been compared to data collected from the thinner 1 µm Ge layer devices, commercial InGaAs/InP SPAD detectors, as well as all-silicon and all-germanium devices.

## 5.2 Ge-on- Si SPADs Fabrication Processes and Design

The fabrication method used to produce the Ge-on-Si SPADs that form the subject of this Chapter has been used to create several batches of SPADs. However, factors such as variations in the charge sheets, dopant density and other device design parameters can affect the quality of the devices produced. A schematic of the planar devices are shown in Figure 5.2 (b), and they differ from previous mesa designs shown in Figure 5.2 (a), where the sidewalls of the charge sheet are exposed through etching after implantation of the charge sheet.

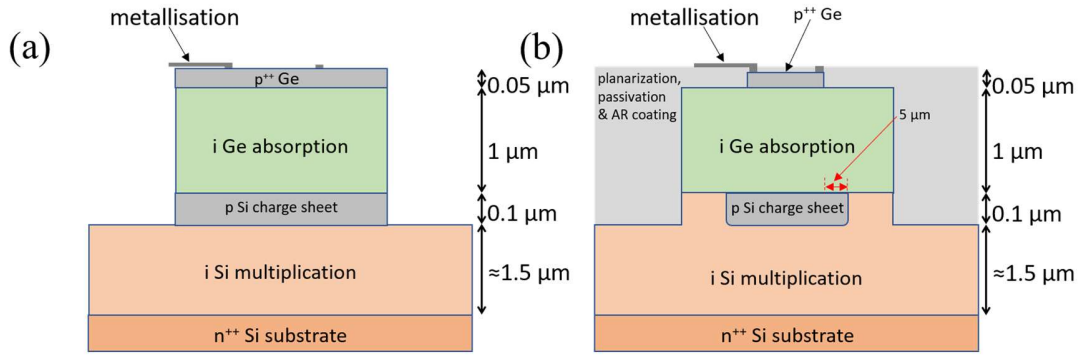


*Figure 5.2. Cross section diagram (not to scale) showing a single Ge-on-Si SPAD device in a (a) mesa geometry and (b) planar geometry layout. The planar structure required two epitaxial stages to allow the charge sheet to be formed using ion implantation before the separate growth of the Ge layers.*

The top contact of the device is formed by the $p^{++}$ Ge layer. The i Ge layer acts as an absorber for incident photons that enter the device through the active area defined by the width of the charge sheet. The Ge absorption layer is what gives the device its optical detection capabilities within the SWIR as this is where the incident photon is absorbed and ionises the initial electron. The charge sheet defines the strength of the electric field across the silicon multiplication region where impact ionisation takes place under a high electric field. Finally, $n^{++}$ Si substrate which the device is grown onto acts as a ground contact.

The first step in the fabrication is to epitaxially grow a Si multiplication region, on top of a $n^{++}$ 150 mm Si substrate, using reduced pressure chemical vapour deposition, this process aims to produce uniformity across the substrate. The charge sheet regions are then defined using photolithography, and this region is then implanted with boron acceptors at an energy of 10 keV, positively doping it to a density pre-decided during the modelling stage. The boron is then activated at 950 °C for 30 seconds using a rapid thermal annealer, dopants need to be activated to produce the desirable electronic qualities. Different doping levels were used to vary the electric-field profile of the Ge which allowed for experimentation to find optimal parameters. It is then cleaned and the Ge absorption layer, and Ge top contact layer (50 nm $p^{++}$) are grown on top of the Si layer again using reduced pressure chemical vapour deposition. The thickness of the Ge absorption layer varied between 1 µm and 2 µm depending on the batch, but this is specified for each set of devices produced. The top Ge contact layer is etched using photolithography and a fluorine inductively coupled plasma reactive ion etch (ICP-RIE). This process is repeated to electrically isolate the SPADs from each other. The distance from the edge of the charge sheet to the sidewall of the device is decided by the superpixel width which varied between 5 µm and 15 µm. Finally, the devices are planarized with hydrogen silsesquioxane and passivated with $SiO_2$, to form protection against corrosion. A metallic 'sandwich' consisting of titanium and aluminium is then evaporated onto the bottom of the devices to form the back contact and photolithography was used to form the top contact of the same material, and a silicon nitride anti-reflection coating is added to prevent any light being reflected into undesired locations [52]. The process required for mesa devices only requires a single etch and so the alignment and uniformity of mesa geometry devices are easier to achieve. The planar SPADs used in this

thesis are manufactured from the same wafer and a similar method as reported by P. Vines *et al.* [40], however they differ slightly as they were produced with varying super pixel widths, and $SiO_2$ is used as the passivation material instead of $GeO_2$. This approach was used to attempt to fabricate more robust SPAD detectors with smaller diameters, to take advantage of the performance enhancement predicted for the smaller device volumes.

### 5.3 Ge-on-Si SPAD Characterisation Set-up

In the Ge-on-Si SPAD detectors used in this Chapter, the epitaxial layers were grown commercially to our specification. The photolithography and etching were performed at the University of Glasgow, and the ion implantation was performed by a commercial supplier. We fabricated 3 sets of planar Ge-on-Si SPADs varying in active area from 26 to 200 µm diameter on the same wafer, all with a 1 µm thick layer of germanium absorber. The width by which the Ge absorber extends past the charge sheet is referred to as the width of the superpixel, as highlighted in Figure 5.2.

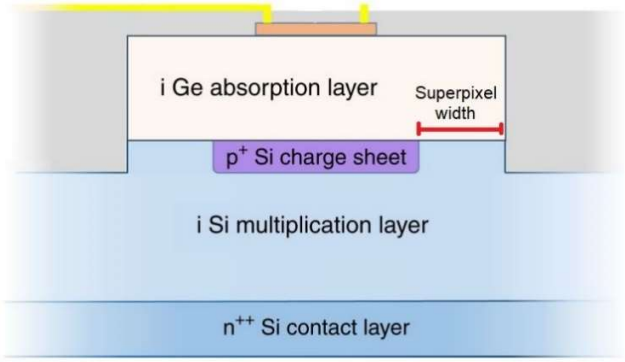


*Figure 5.2. Schematic of the planar geometry Germanium on Silicon SPAD cross section, showing the generic microstructure of the device, where the width of the superpixel is depicted.*

Of the 3 sets of devices produced by the University of Glasgow quadrant 1 (Q1) had a 5 µm superpixel width, quadrant two (Q2) had a 10 µm superpixel and quadrant 3 (Q3) had a 15 µm superpixel. The wafer was then cut using a diamond blade circular saw into 4 sections

and each section subsequently cut in half with 26 µm and 50 µm diameter devices on one half, and 100 µm and 200 µm diameter devices on the other. Both halves are pictured below in Figure 5.3.

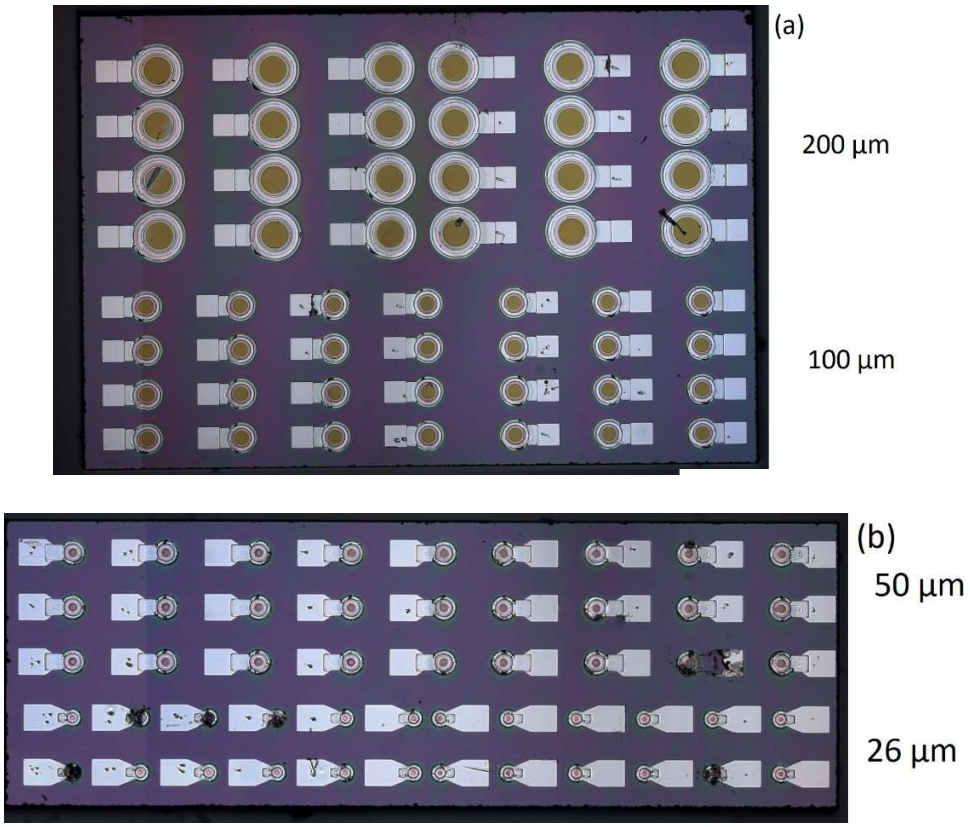


*Figure 5.3. Microscope image at ×5 Magnification of (a) 100 and 200 µm diameter, and (b) 50 and 26 µm diameter Ge-on-Si SPADs after acetone and isopropanol cleaning process.*

The samples were cleaned using acetone and isopropanol and dried in between using compressed nitrogen. This process was repeated multiple times to clean the sample. When not in use the devices were kept in a vacuum chamber to help preserve their longevity.

Before a full TCSPC characterisation was carried out it was important to identify the best devices to characterise. To do this, the current-voltage (IV) characteristics of all devices were measured by means of a cryogenic probe station. The best SPADs will have a low dark

current, multiplication after punchthrough when illuminated and a sharp breakdown. Punchthrough occurs when the electric field extends into the absorption region, allowing the photogenerated electrons to drift into the multiplication region. It has been previously demonstrated that avalanche diodes with low dark currents have lower DCR and this is desirable for a low noise detector [53].

The probe station used to perform IV characterisation of the devices was a JANIS ST-500 low vibration (± 25 nm) model held under a vacuum of the order of $1x10^{-5}$ mbar. This set-up allowed for quick probing of multiple devices without the need for time consuming permanent bonding or soldering processes. A camera and microscope system was employed to view the devices within the probe station and so allowed for accurate probe placement. The probe station therefore needed to be low vibration as accurate alignment between the contact pads of the devices and the probing needle was essential. The system was cooled using liquid nitrogen to approximately 77 K with a cooling rate of no more than 1 degree per minute to prevent uneven reduction/expansion within the device. As the devices are made up of several materials with different expansion coefficients, rapid cooling could potentially lead to cracks within the device. For the characterisation of the devices the IV characteristics of samples from all 3 quadrants and all 4 different sizes were investigated. We applied a reverse bias voltage up to the device breakdown voltage ($V_B$), which was between -38 V and -42 V, over each device in turn and recorded the resultant current. Figure 5.4 shows an example of the IV characteristics that were recorded for an applied reverse bias. The forward bias characteristics was also investigated, an example of which is shown in Figure 5.5. Whilst performing the reverse and forward bias voltage measurements, the maximum current allowed to be received by the device was limited to 0.1 mA and 1 mA respectively. This limit was used to prevent the device overheating and risking irreparable damage.

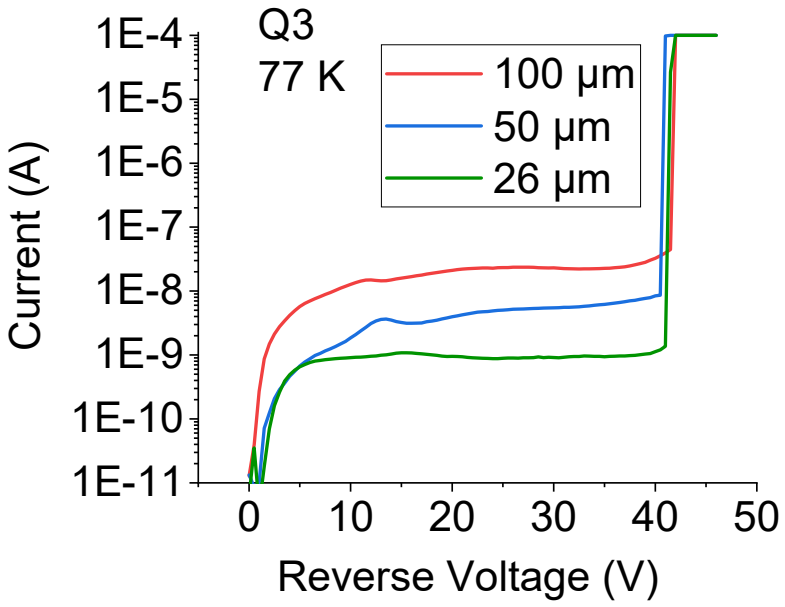


*Figure 5.4. An example of the reverse biased IV curves for 26, 50 and 100 µm diameter devices produced at 78 K in the probe station. Showing the increasing dark current with diameter of device.*

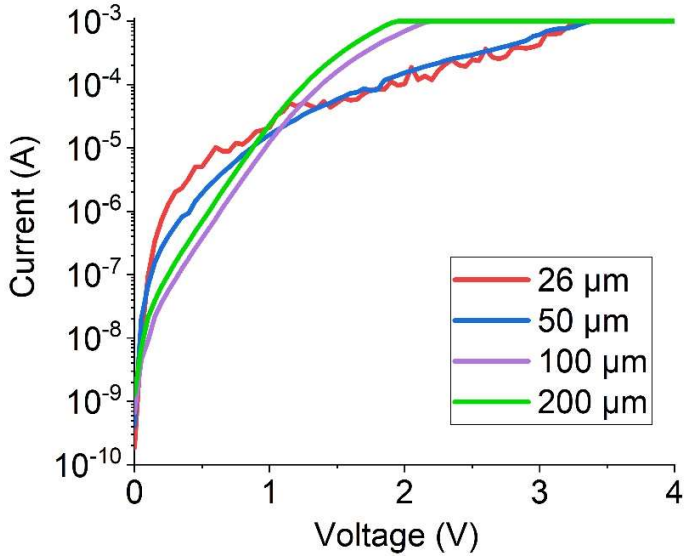


*Figure 5.5. An example of the forward biased IV curves for 26, 50, 100 and 200 µm diameter devices produced in the probe station. Showing similar relationships between the two smaller and two larger devices.*

This procedure allowed us to analyse the best devices. Q1 was discarded due to low yield, approximately 50 % of the devices were either open circuits, short circuits or did not breakdown within a reasonable voltage limit (~ 60 V) and the other 50 % had a dark current approximately a factor of 10 higher than Q2 and Q3. The best 26 µm and 50 µm diameter devices in Q2 and 100, 50 and 26 µm devices in Q3 had a much higher rate of successful fabrication and more repeatable results. The devices with the lowest dark current before breakdown and the sharpest breakdown curve were favourable. The best devices of every size from each quadrant were ranked, so the best two or three devices could then be bonded. The chips were mounted onto a gold electronic package using silver conductive paint and the individual devices were ultrasonic wire bonded to provide electrical connections. Figure 5.6 shows the device after being attached to the package before being wire bonded. The best devices of each size were then used for full characterisation. When undergoing full testing a different cryostat was used which was aligned into the experimental set-up and allowed the devices electrically connected in a lower noise configuration than the probe station would allow. The package was mounted on a cold finger, wired up and placed inside an Oxford instruments OptistatDN cryostat with an intelligent temperature controller. The inner chamber was held at pressure of ~ $10^{-2}$ mbar and the outer chamber was reduced to a higher vacuum of $10^{-5}$ mbar. Helium gas constantly flowed into the inner chamber acting as a transfer gas over the temperature gradient between liquid nitrogen cooled outer chamber and the SPADs housed inside the inner chamber. The cryostat allowed for testing at temperatures between 293 K and 78 K. Initially, an IV characteristic was taken for the selected device, before commencing testing, to check consistency in the devices characteristics and breakdown voltage.

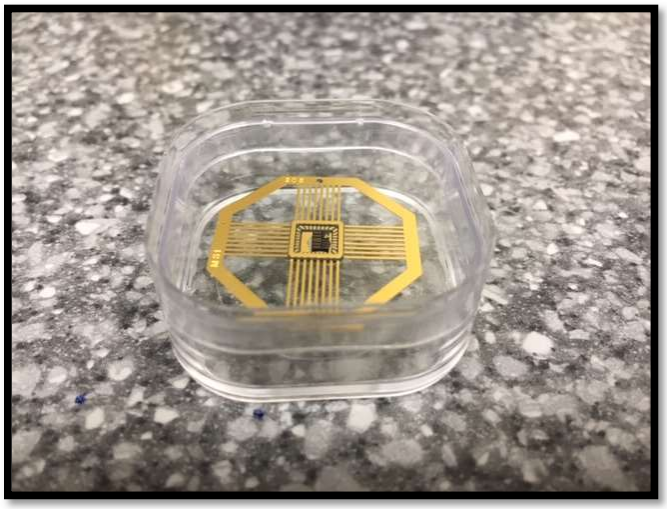

*Figure 5.6. Ge-on-Si SPAD chip mounted onto a gold electrical package using silver conductive paint, ready to be wire bonded for further characterisation.*

Measurements were performed using a basic time-correlated single-photon counting (TCSPC) set-up an example of which is shown in Figure 5.7.

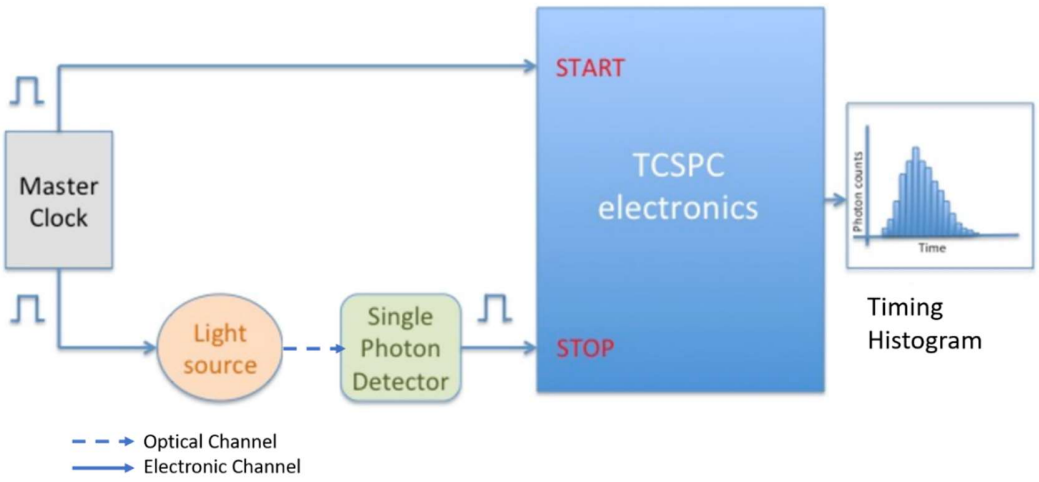


*Figure 5.7. Basic TCSPC set-up depicting the start pulse initiated by the master clock and the stop pulse caused by the detection of a single-photon. The time between the start and stop pulse is measured and recorded in a histogram [49].*

The main purpose of a TCSPC set-up is to measure the arrival times of single-photons with reference to an initial laser pulse. By using this type of experiment, we can gather multiple readings quickly, making our results more statistically reliable. The experimental set-up we used is shown in Figure 5.8.

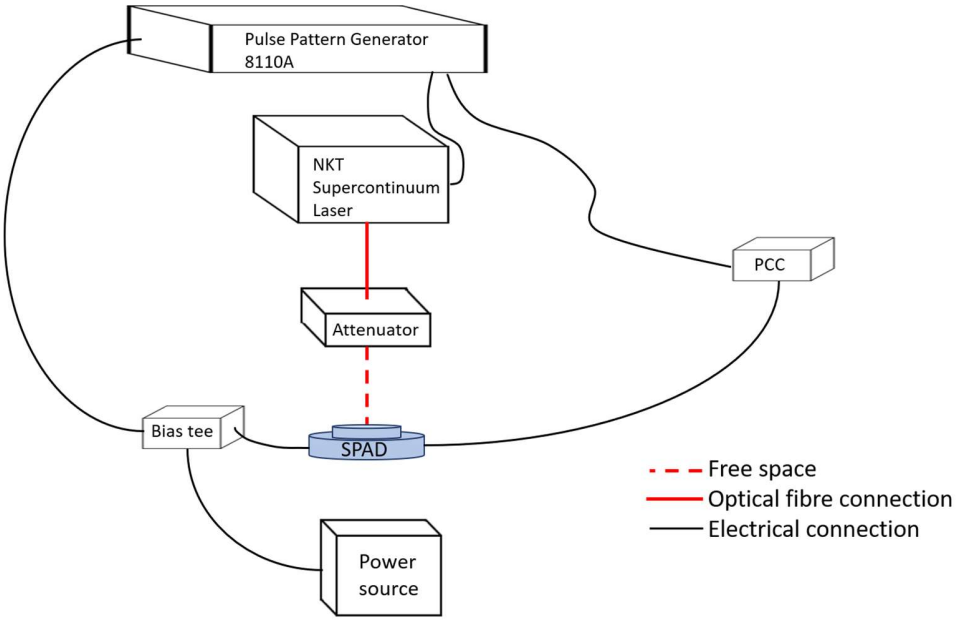


*Figure 5.8. Experimental set-up used to characterise Ge-on-Si SPADs for SPDE, DCR and jitter. This includes a wavelength tuneable NKT supercontinuum laser source, and a pulse pattern generator providing timing for the photon counting card (PCC) which is the TCSPC module.*

The set-up used to find the DCR and SPDE consisted of an Agilent 81110A pulse pattern generator (PPG) which was used to produce an AC voltage, connected to a bias tee with a DC voltage source. When combined they biased the SPAD above breakdown and into Geiger mode operation and quenched it periodically. The NKT Supercontinuum laser was used at 1310 nm wavelength, at a suitable frequency; the laser also acted as the 'master clock' for the system. The pulse was coupled into a 50/50 optical fibre splitter which meant the power was known and could be monitored throughout the experiments. An attenuator was used to reduce the laser power to less than 1 photon per pulse so as to work well within

the single-photon regime (approximately 0.01 photons per pulse) and a free space set-up was used to align and collimate the beam onto the optical window of the cryostat housing the samples. A pellicle beam splitter was used to send an external white light source to an infrared camera and image the inside of the cryostat onto a monitor. The cryostat allows for micro-positioning in 3 degrees of movement, thus with the aid of the camera the samples can be accurately aligned with the laser light at normal incidence to the sample. Every laser pulse generates the START signal for the master clock and each photon detected generates a STOP signal. The time difference between the START-STOP sequence is recorded by a photon counting card (PCC) and plotted into histograms using T900 computer software. The electronics and cabling of the system also have a jitter contribution and a timing delay. The PCC had a built-in resistance of 50 Ω which converts the current produced by the SPAD into a detectable voltage.

The attenuation through the system was checked and adjusted accordingly before starting each set of measurements. At every temperature, before characterising the device, an IV measurement was performed to find the breakdown voltage, as this varied with temperature. Lower temperatures result in lower breakdown voltages as the number of phonons that have the potential to interact with the drifting carriers within the lattice are decreased. A DC voltage just below breakdown was applied and an AC voltage provided biases of 1% through to 6.5% over the breakdown voltage, reducing the maximum voltage when necessary as not to overload the detectors at higher temperatures. Multiphoton events within the START-STOP sequence distort the histogram because of a phenomenon called pulse pile-up. If the STOP rate becomes too high for the TCSPC electronics to register subsequent avalanches, then photon detections are lost which can lead to a higher photon event probability in the early part of the timing windows leading to an uneven probability of detection across the histogram window. Due to this phenomenon the STOP rate was limited to less than 10 % of the START rate [54]. It was also important to make sure the acquisition time was sufficient to have multiple counts in each bin of the histogram. A bin width of 195 ps was chosen to balance the acquisition time with the precision of the results.

A Keysight InfiniiVision 6000 oscilloscope with a 1 GHz bandwidth was used to check the SPAD was being biased in synchronisation with the laser pulse arrival. We were able to use a gating technique to quench the devices because the system is temporally aligned, and the arrival time of a photon is known. In other applications when the photon arrival time is unknown a different technique is required. Active quenching techniques can be utilised by using a fast comparator which can respond to an avalanche within nanoseconds [55, 56]. An example of a typical pulse after a 130 ns AC gate depicting an avalanche event can be seen in Figure 5.9. The peak voltage during the avalanche was also important to measure as this allowed us to choose the correct threshold voltage for the photon counting card which was needed for the readout. The minimum voltage threshold used was approximately 30 mV this was high enough to avoid any obvious noise in the system and small enough to detect breakdowns even at some of the lower excess biases I investigated. The width of the pulse is determined by the duration of the AC gate produced by the pulse pattern generator.

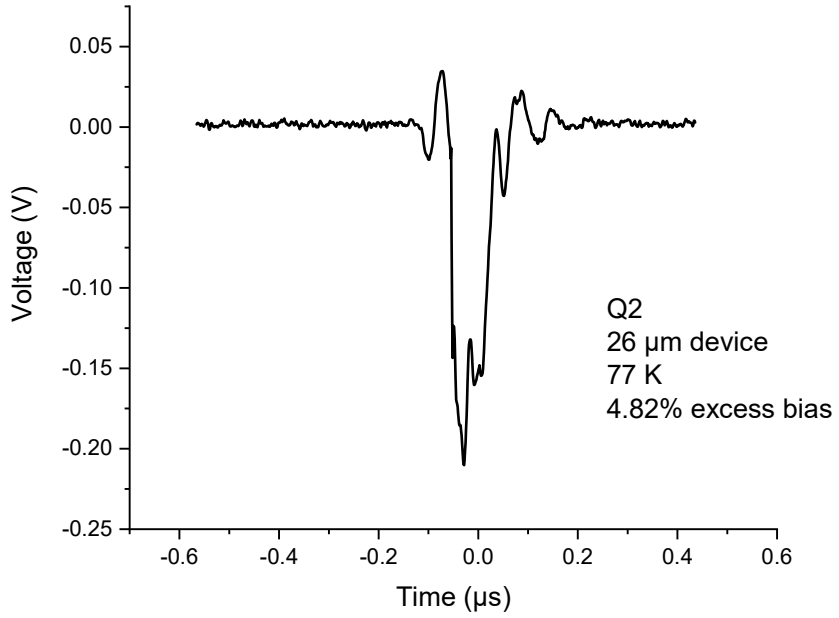


*Figure 5.9. A typical pulse as seen on the oscilloscope of a 26 μm diameter device breaking down, at peak breakdown voltage reaching over -200 mV.*

To perform SPDE measurements the laser beam was aligned with the active area of the device; the alignment was closely monitored throughout the testing process. To perform DCR measurements the laser was turned off and the optical window of the cryostat was

completely blocked to minimise ambient illumination. All the measurements for a single device were taken within the same day to help ensure accurate and reliable results and avoid any possible effects of the device aging. However, many of the devices were tested and temperature cycled almost daily with no effect on their IV characteristics or results. Measurement of the timing jitter of the devices required higher temporal accuracy. Therefore, a narrower bin width of 9.77 ps was set on the PCC, and as a result a longer acquisition time was required to take reliable results.

### 5.4 Ge-on-Si SPAD Characterisation Results

This subsection presents the TCSPC characterisation results obtained from the best performing Ge-on-Si SPADs fabricated with the process outlined in section 5.2, with active area diameters of 26 and 50 µm and a 15 µm superpixel. The breakdown voltage of SPADs is greater at higher temperatures because at elevated temperatures there is more thermal vibrations and therefore the carrier mean free path is shorter, this means a stronger electric field is required for carriers to the momentum required for impact ionisation to take place. An IV measurement was made on the same day as testing to ensure any temperature and devices variances were accounted for when calculating the voltage required to achieve certain excess biases. However, we found these devices to be impressively robust and had repeatable breakdown voltages at the same temperature after frequent temperature cycling and daily testing. The SPDE (%) versus excess bias (%) is shown in Figure 5.10, at 78, 100, 125 and 150 K. An impressive SPDE of 30 % at 125 K, 1310 nm wavelength was achieved by a 26 µm diameter SPAD with an excess bias of 6.5 %. This is higher than previous mesa geometry designed SPADs which typically achieved single-photon detection efficiencies of less than 5 % at a wavelength of 1310 nm [40, 47]. There was also significant improvement when compared to similar Ge-on-Si lateral avalanche photodiodes reported by Martinez *et al* in 2017 who reported an SPDE of 5.27% whereas at 78 K we are reporting SPDEs of up to 28 % [57]. It would have been possible to achieve higher SPDE from the 50 µm devices had large DCRs not prevented a higher bias being used. This was concluded after studying the SPDE plots in Figure 5.10.

It is thought that the 26 µm diameter devices were not collecting all the incident laser light as the spot size was of a similar size to that of the device active area which meant the active

area of the SPADs were not receiving the full Gaussian beam illumination and were more subject to misalignment during the experiments. A potential solution would be using a different collimation package to reduce the laser beam width.

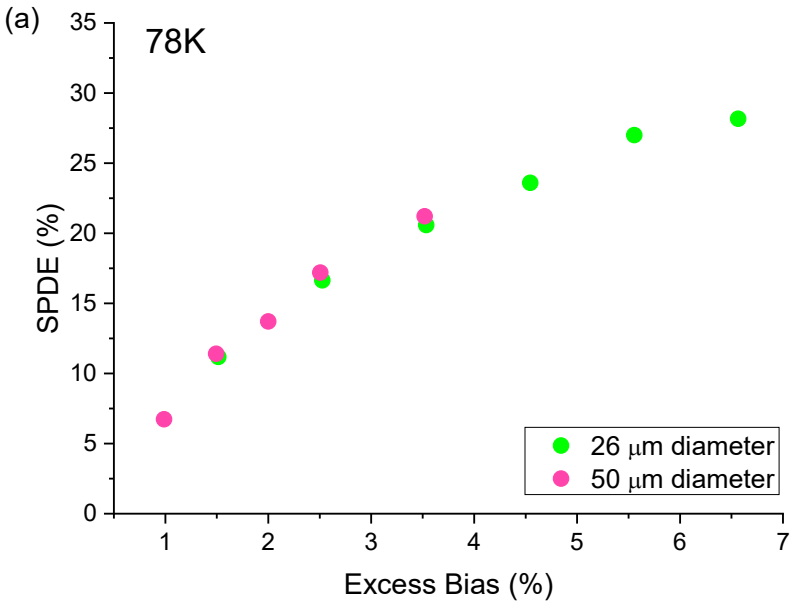


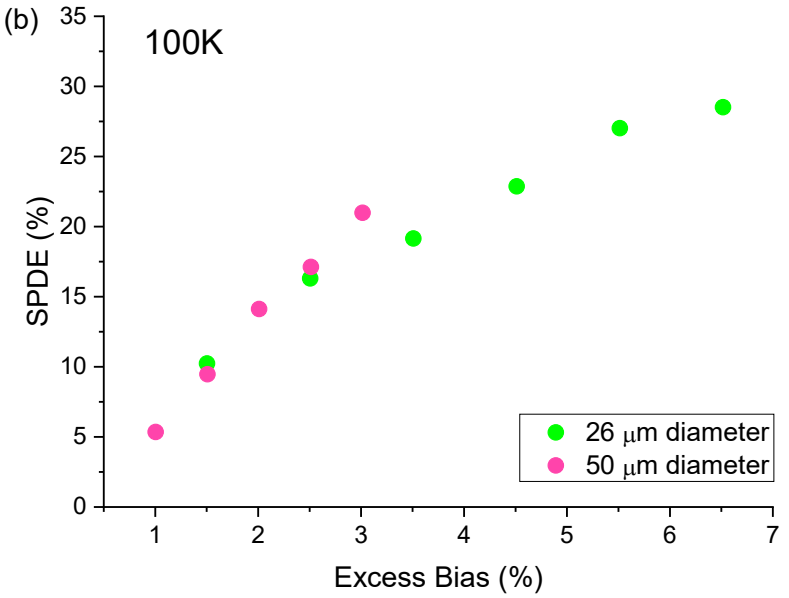

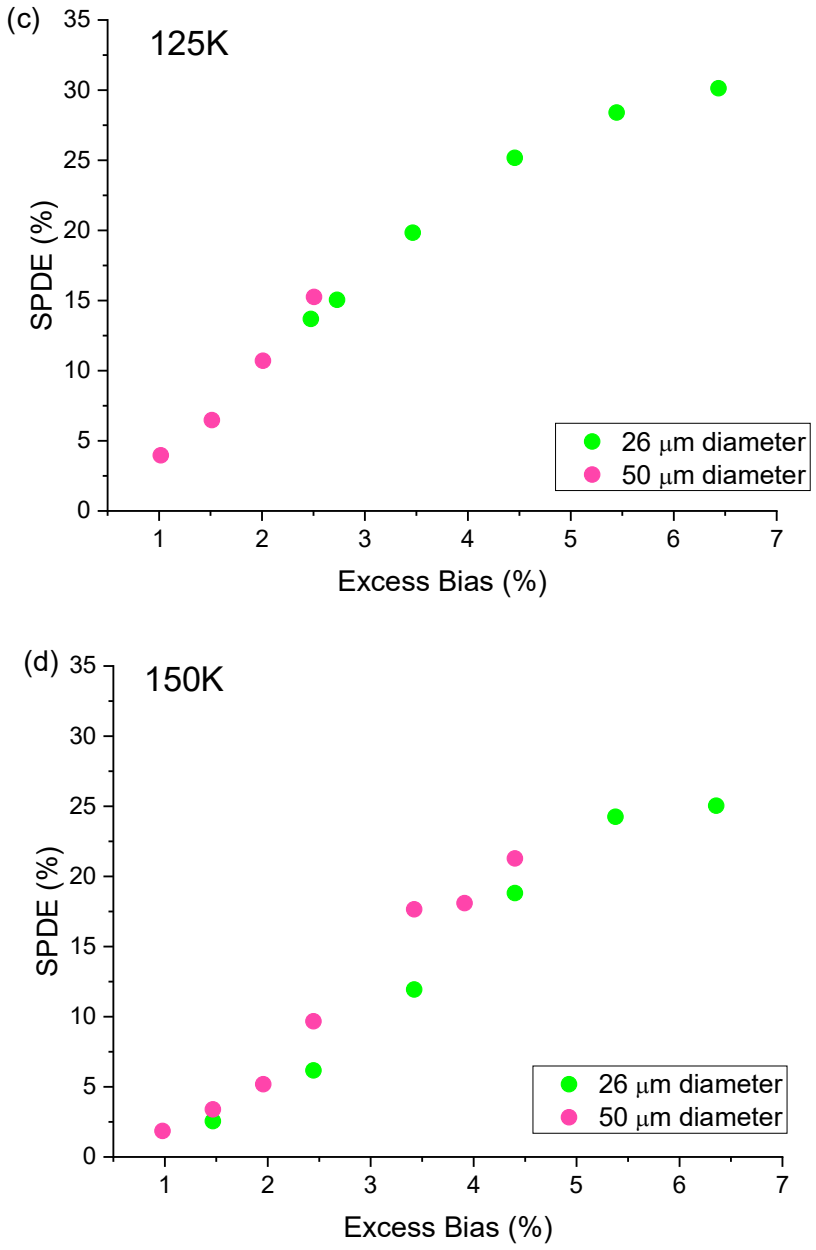


*Figure 5.10. SPDE plotted of a function of excess bias for both 26 μm and 50 μm diameter Ge-on-Si single-photon avalanche diodes at operating temperatures of: (a) 78 K;(b) 100 K; (c) 125 K; and (d) 150 K.*

The DCR results can be seen in Figure 5.11. As expected, the larger device has a considerably higher DCR at all temperatures. Further research is needed to identify whether the DCR is linearly proportional to the active area of the device although it has previously

been suggested that the DCR scales proportionally with device volume [52]. The DCR was highest at 78 K and 150 K. The two intermediate temperatures have a lower DCR; the 78 K result suffers most from afterpulsing and the 150 K result suffers from thermal excitation. Afterpulsing is maximised at low temperature as the carriers have less kinetic energy and therefore a longer lifetime. Whereas at higher temperatures the DCR is predominantly caused by carriers being thermally excited independent of laser illumination. Both devices showed DCRs in a range of a few thousands' cps.

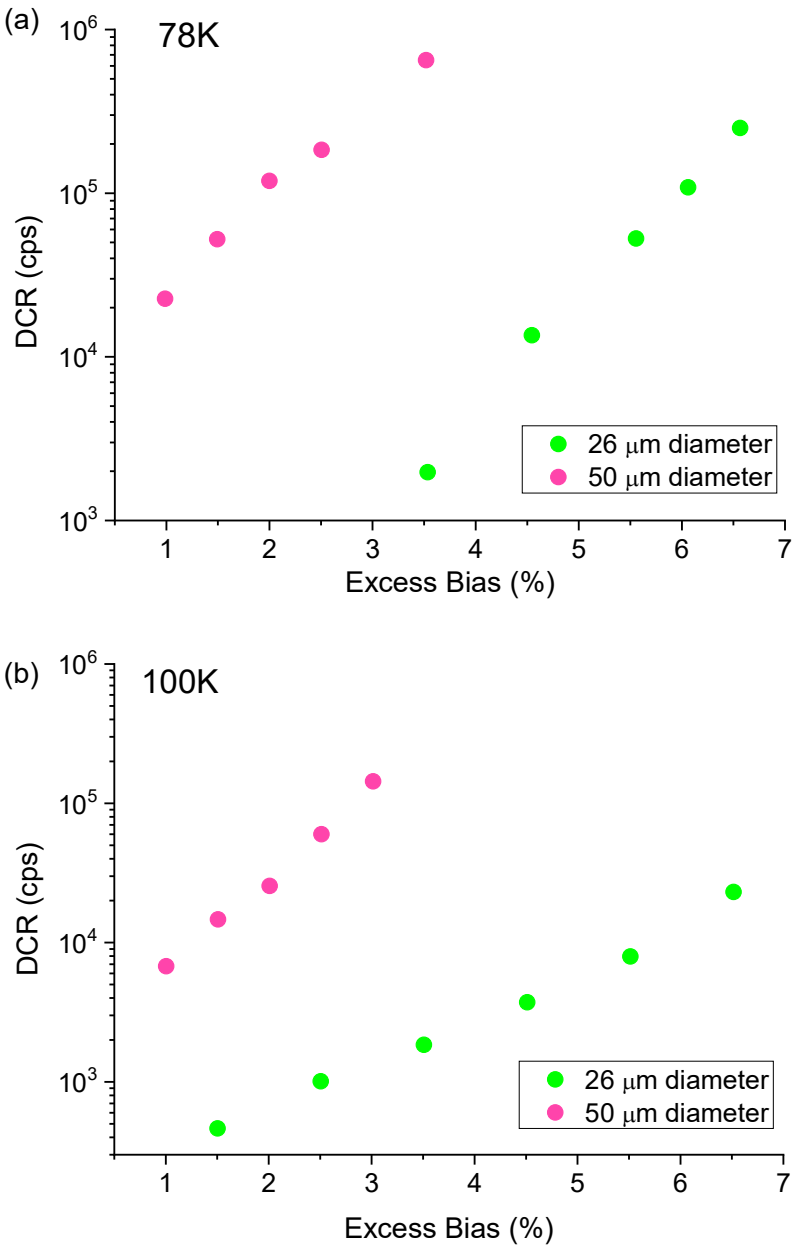

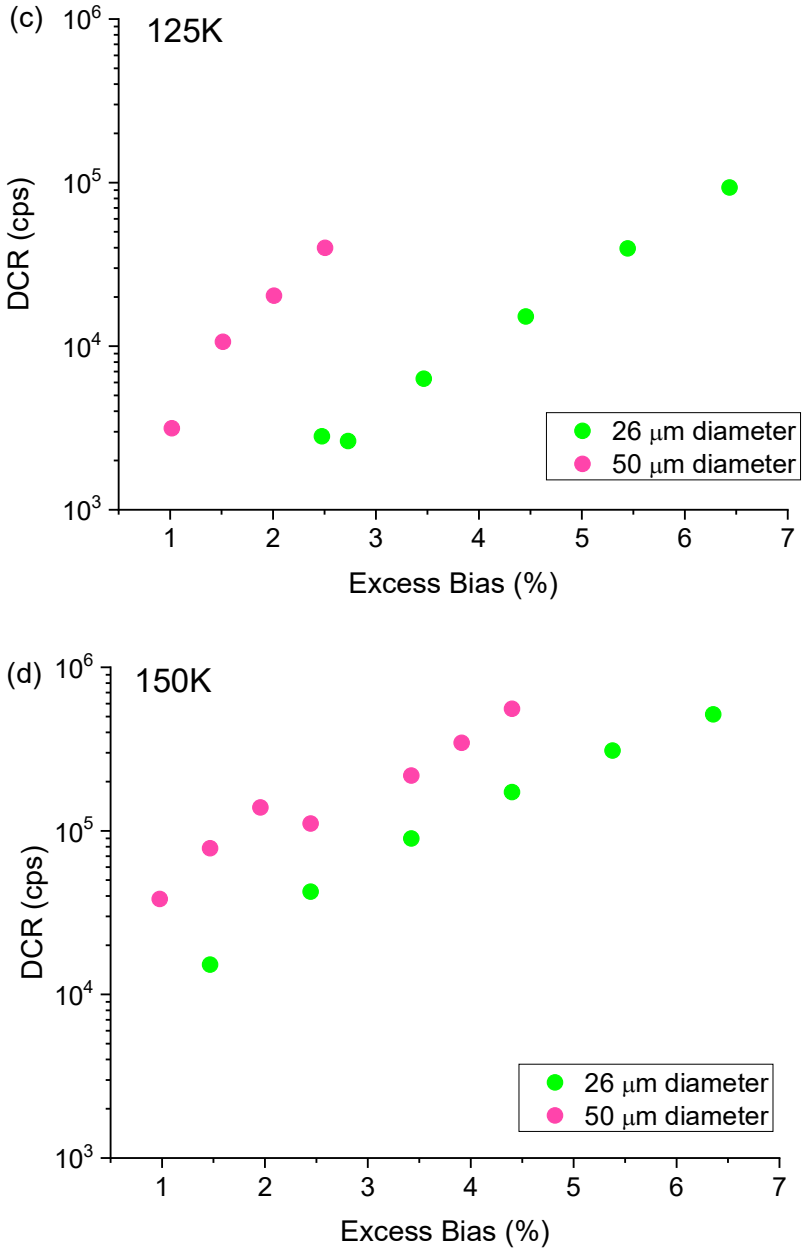


*Figure 5.11. Dark count rate plotted as a function of excess bias for both 26 μm and 50 μm Ge-on-Si single-photon avalanche diodes at operating temperatures of: (a) 78 K; (b) 100 K; (c) 125 K; and (d) 150 K.*

Figure 5.12 (a) shows the timing histogram that the jitter was calculated from using the FWHM value. The final calculated jitter results are presented in Figure 5.12 (b). The smallest jitter recorded was 126 ps at 150 K with an excess bias of 5.5 % which is comparable to commercially available InGaAs/InP SPAD detectors [38].

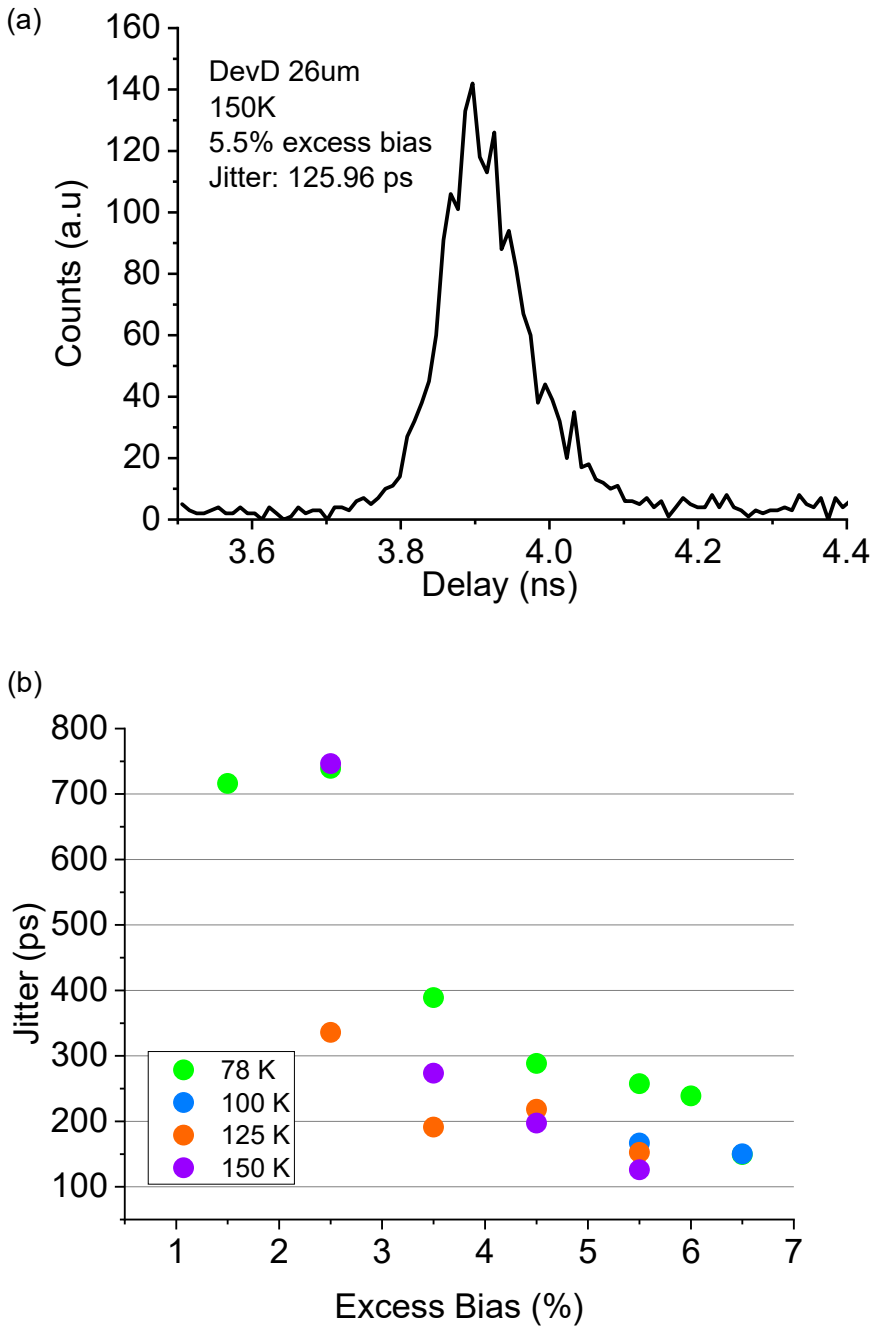


*Figure 5.12 (a) Jitter histogram with FWHM of 126 ps for a 26 µm diameter Ge-on-Si SPAD at 150 K and an excess bias of 5.5 %. (b) Jitter results from planar Ge-on-Si SPAD at temperatures between 77 and 150 K at a range of excess biases.*

The NEP results were calculated using equation 3.8 as detailed in Chapter 3 section 3.8: $NEP = \frac{hv}{SPDE} \times \sqrt{2 \times DCR}$. And impressive results as low as 4 x $10^{-17}$ $WHz^{-1/2}$ at 100 K with an excess bias of 2.5 % were achieved. This low NEP value was calculated from a SPDE of 16 % and a DCR of 1008 Hz and has been plotted on Figure 5.13 alongside other SPADs and APDs. Comparing this with previously reported results we can see clear improvement especially for mesa devices which show a factor of 1000 improvement [58].

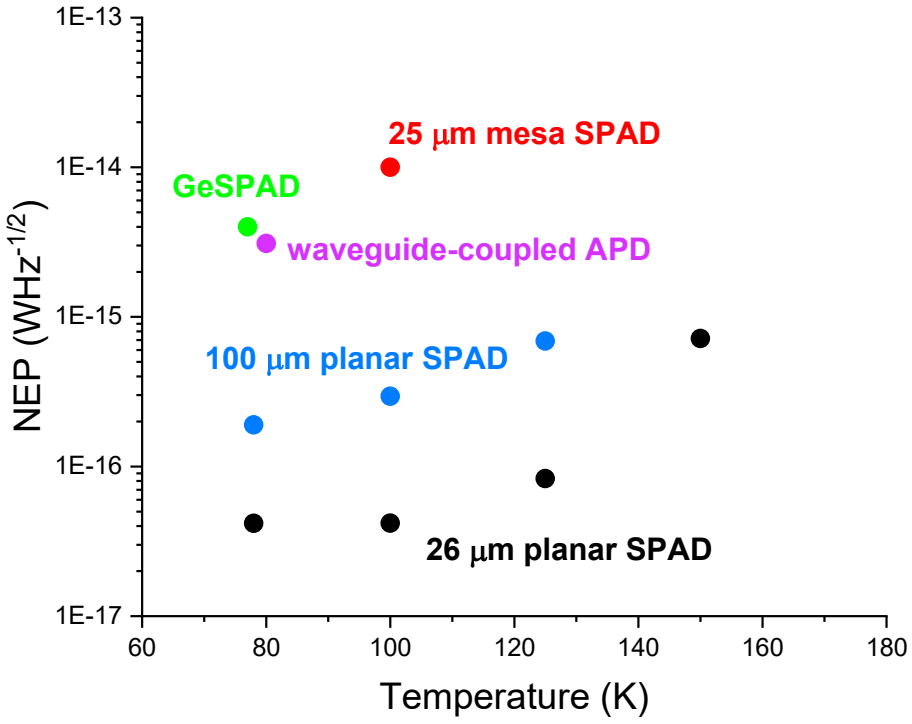


*Figure 5.13. The noise-equivalent-power as a function of temperature for a 25 μm mesa SPAD (red) [58], a Ge-SPAD (green) [48], waveguide-coupled Ge-on-Si SPAD (purple) [57], 100 μm planar Ge-on-Si SPAD (blue) [40] and the planar 26 μm Ge-on-Si SPAD reported in this thesis (black). Graph reproduced from [59].*

With such small device diameters, one of the largest source of error for the SPDE results originates from laser misalignment. The low temperature operation can lead to small misalignments as a result of thermal fluctuations in the mechanical mountings of the cryostat. This can move the laser out of focus or alignment with the active area of the SPAD

being tested. This is particularly evident when characterising the smallest area devices, in this case the 26 μm diameter SPADs, or detectors with non-uniform efficiency across their active area. To account for this, measurements were repeated multiple times adjusting the alignment as necessary to check for consistency. There are other sources of error which stem from the distribution of the counts recorded in the histograms. Because of this normal distribution there is a Poissonian error associated with the results. The standard deviation for a Poissonian distribution is equal to the square root of the number of data points. As the count rate was relatively high, it was found that the standard deviation was typically so small it would not have been visible by plotting error bars on the graphs. Another source of error originates from the disparity between the excess biases applied to the device when measuring the SPDE and the DCR. Since there is an uncertainty as to the exact voltage applied, combining the SPDE and DCR at marginally different voltages will lead to errors in the NEP value calculated from these numbers. To reduce the chances of this the SPDE and DCR readings for a set excess bias were done immediately after each other. There is also an error introduced by the calibration of the power meter, however this was mitigated by regular recalibration by the vendor. Power fluctuations by the laser also need to be accounted for, by allowing the laser output to stabilise before starting measurements, the severity of the fluctuations is reduced and by recording the power before and after taking measurements the laser intensity could be continually monitored.

Figure 5.14 shows that as the SPDE increases with excess bias and at all temperatures the SPDE is relatively similar. At 175 K only two low excess biases were measured to avoid the risk of the device overheating and becoming damaged due to the high DCRs. At high excess bias the SPDE tapers off, we believe this is due to an increase in DCR limiting the ability to keep the STOP rate below 10 % of the START rate. Figure 5.15, reiterates this consistency between SPDE and temperature. However, the efficiency drop at 150 K is not consistent with the other temperature results, this measurement was repeated multiple times and was constantly lower than expected, this could be due to misalignment initially or more likely damage to the device.

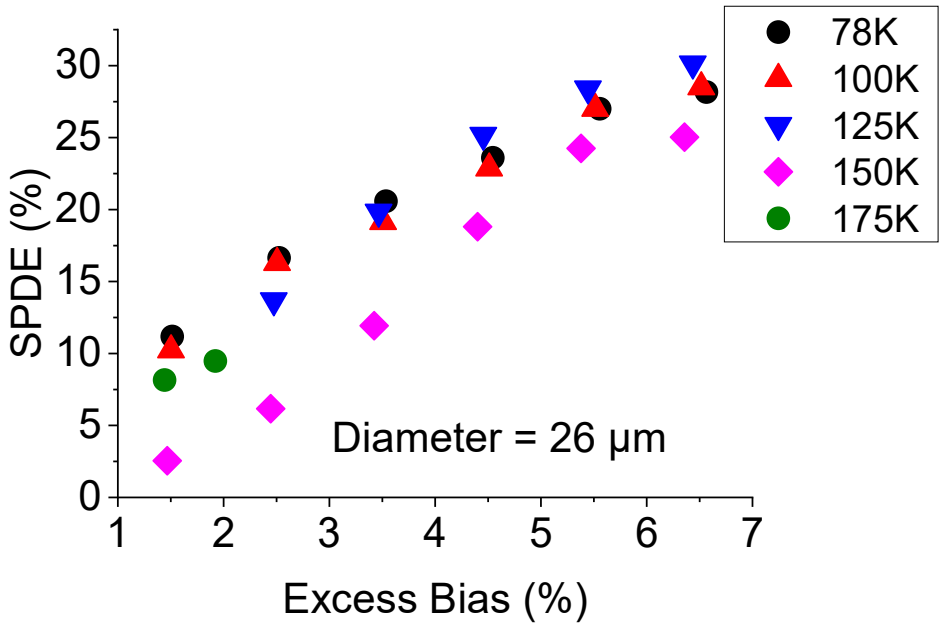


*Figure 5.14. SPDE for a 26 µm diameter planar Ge-on-Si SPAD plotted as a function of excess bias at temperatures from 78 K to 175 K.*

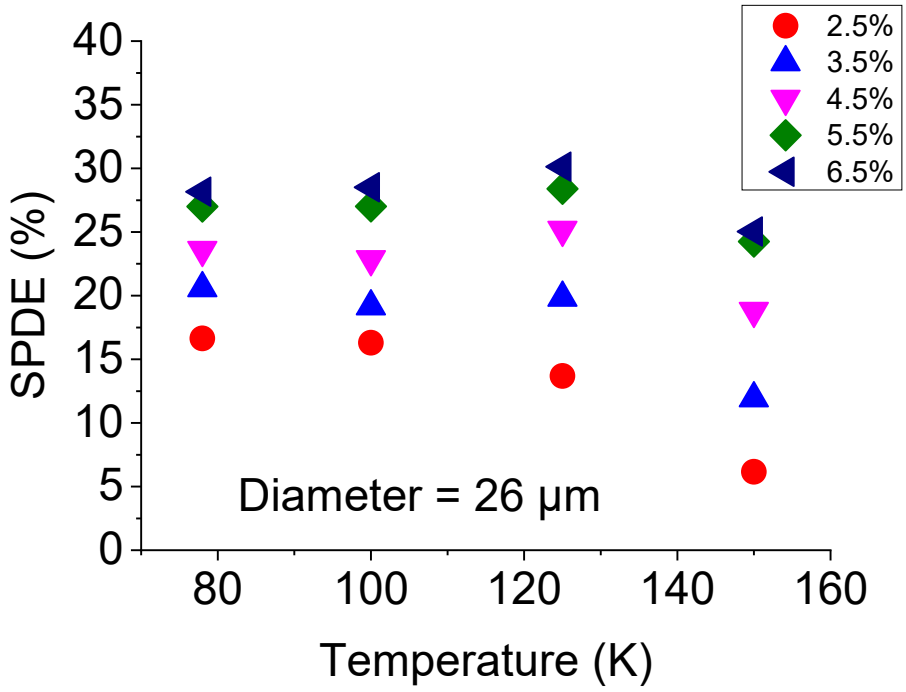


*Figure 5.15. SPDE as a function of temperature at excess biases of 2.5 % - 6.5 % for a 26 µm diameter planar Ge-on-Si SPAD.*

The effect of excess bias on DCR can be seen in Figure 5.16. The DCR has a clear dependence on the excess bias. Given that the energy of a carrier is proportional to the voltage squared and that DCR is caused by thermal excitations within the device, the DCR may be expected to be proportional to $V^2$. However, no such graph fitting has been performed yet and this should be examined as future research.

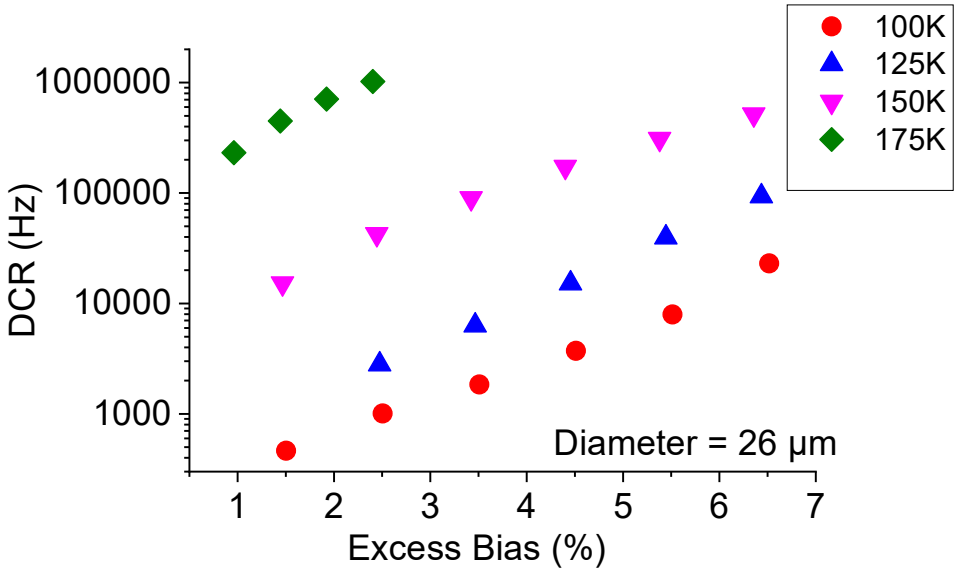


*Figure 5.16. DCR of a 26 µm diameter planar Ge-on-Si SPAD plotted against excess bias at temperatures from 100 to 175 K.*

Figure 5.17 shows the DCR increasing with temperature as more thermal excitation takes place. However, it is clear that at the lowest temperature (78 K) the DCR results do not appear to fit the rest of the trend. This is because at 78 K the device is suffering from more afterpulsing effects which are magnified at lower temperatures, hence skewing the graph. At 100 K it does not appear to significantly affect the DCR, with thermal excitation dominating the graph shape.

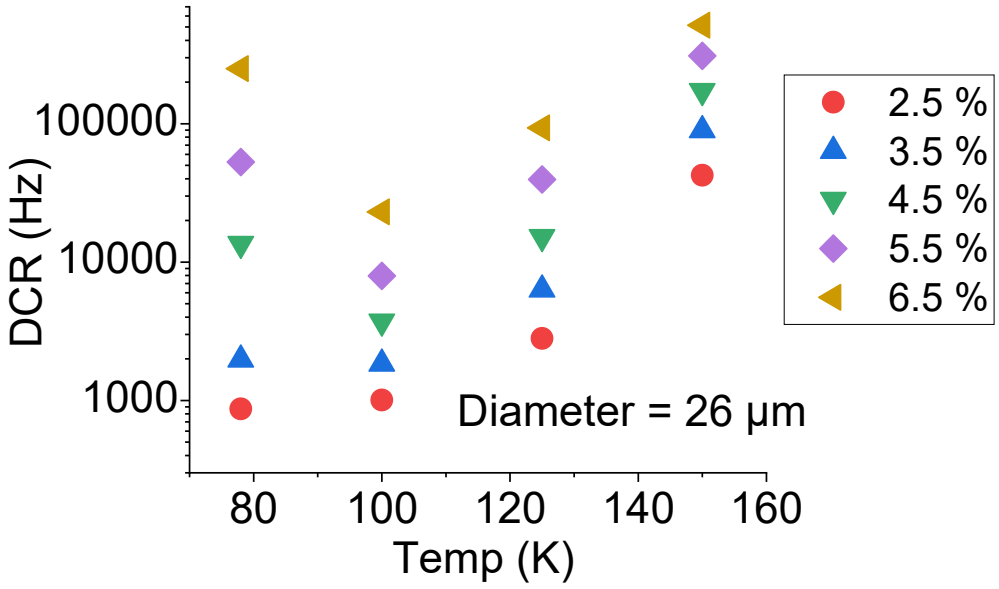


*Figure 5.17. DCR as a function of temperature at excesses biases of 2.5 % - 6.5 % for the 26 µm diameter planar Ge-on-Si SPAD.*

Another characteristic that can be extracted from studying the DCR of a device is the activation energy. This is the energy of the traps within the device, as they contribute to the dark counts through their thermal activation. This information can be used to isolate which material or boundary within the device is predominantly contributing to the DCR. This will allow us to improve fabrication of further devices. Figure 5.18 shows an Arrhenius plot of the DCR versus excess excess bias. From this one can extract the gradient at each excess bias and hence calculate the activation energy. However, at the lowest temperature the relationship is skewed, potentially due to afterpulsing. It is possible that at this lowest operating temperature that the charge sheet was beginning to encounter the effects of dopant freeze-out, thus altering the electric field distribution throughout the device.

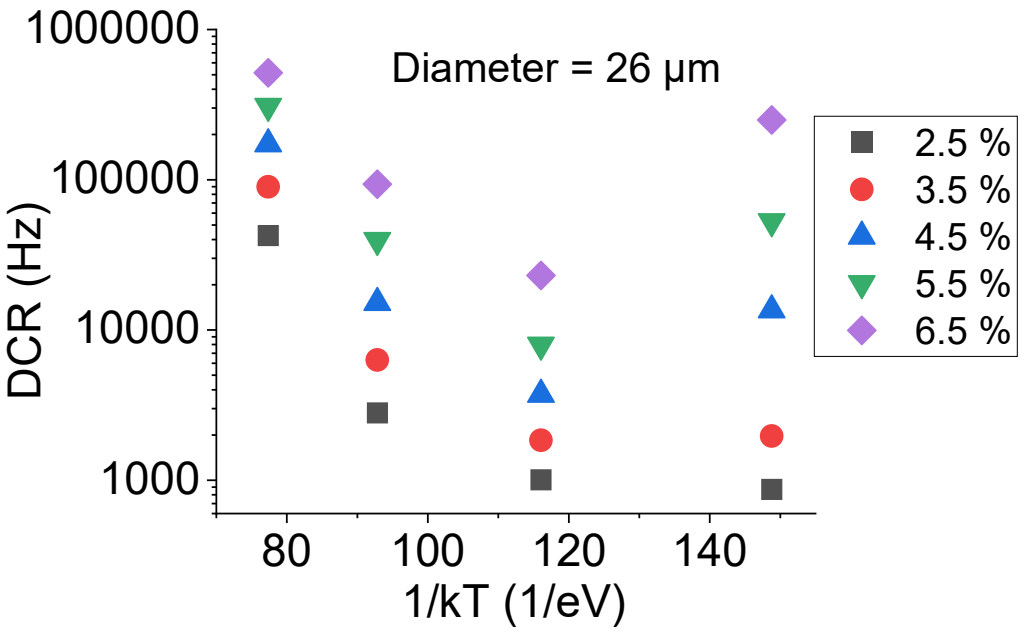


*Figure 5.18. Arrhenius DCR plot used to calculate activation energy of a planar Ge-on-Si.*

By separating the three highest temperatures and discarding the lowest temperature point, activation energies for all the excess biases have been calculated, the gradient and conversely the activation energies for the dominant mechanisms between the temperatures 100 and 150 K (77- 116 $eV^{-1}$) were as follows:

| Excess Bias (%) | Activation Energy (meV) |
|---|---|
| 2.5 | 40.2 |
| 3.5 | 42.0 |
| 4.5 | 41.8 |
| 5.5 | 40.2 |
| 6.5 | 34.2 |

Table 5.1. *Activation energy at different excess biases from 2.5 – 6.5 %, for a Ge-on-Si SPAD using an Arrhenius plot of the DCR to calculate values.*

While it is difficult to draw any strong reliable conclusions with only three different temperatures, we can see that the values are of the same order of tens of meVs for all biases and temperatures. By using the standard deviation formula in Equation 5.1:

$$\sigma = \sqrt{\frac{1}{N}\sum(x_i - \mu)^2} \tag{5.1}$$

Where N is the number of data values, $x_i$ is each value and $\mu$ is the mean of the values. We find the results have a standard deviation of 2.8, and so all excess biases fall within 2 standard deviations of the mean value (39.7 meV) making the results statistically significant if activation energy is not affected by excess bias. It may be expected that this value corresponds with lattice defects energy levels within Germanium, Silicon or their boundary, but given the activation energy of Germanium and Silicon is typically hundreds of meV it is unlikely there is a correlation [60, 61]. But, before drawing any sound conclusions from these results more research has to be done into the relative effect of the afterpulsing/thermal excitation ratio which produces the total DCR.

### 5.5 Higher Detection Efficiency Ge-on-Si SPAD Design

The University of Glasgow fabricated SPADs of different thickness germanium absorption layers to increase the absorption of incident light. The fabrication process was similar to that detailed in section 5.2; however, they had no optical access, the surface of the devices were metalized to act as a top contact. This meant a more rapid fabrication process as there was no etching of the top contact required and the devices did not have to be planarized. This also led to easier probing because of the larger contact area, in most cases. The purpose was to quickly check the fabrication process and form quick comparisons between the IV characteristics of the 1 µm SPADs characterised in section 5.4 and the new devices. These devices were fabricated with 1 µm, 1.5 µm and 2 µm thick germanium layers, to examine how the varying photon absorption affects detection efficiency and DCR. IV characteristics were performed for the different thicknesses and the results for 50 µm and 100 µm diameter devices are displayed in Figure 5.19. Clearly, many of the devices are not exhibiting the form of IV characteristics desired for SPAD operation, i.e. with a low dark current and sharp breakdown.

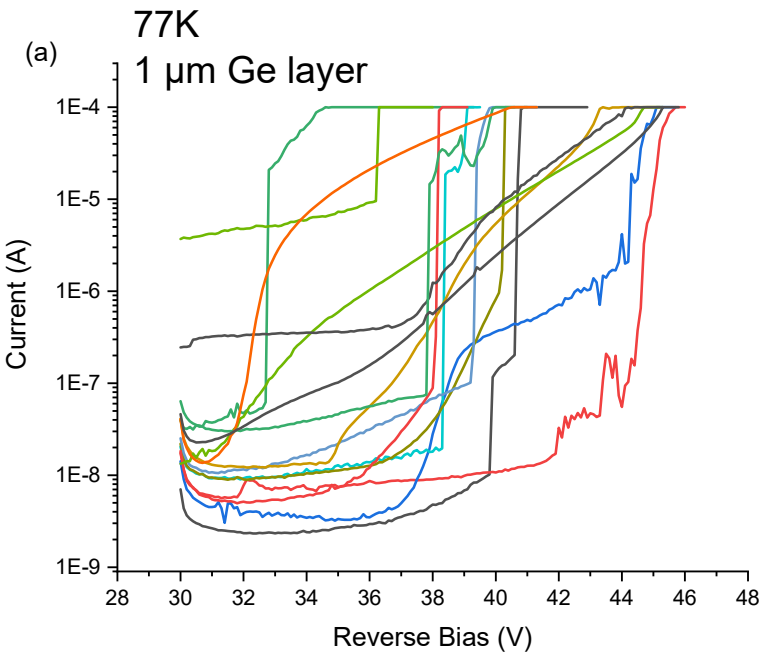
(a)
77K
1 μm Ge layer
Current (A)
1E-4
1E-5
1E-6
1E-7
1E-8
1E-9
28
30
32
34
36
38
40
42
44
46
48
Reverse Bias (V)

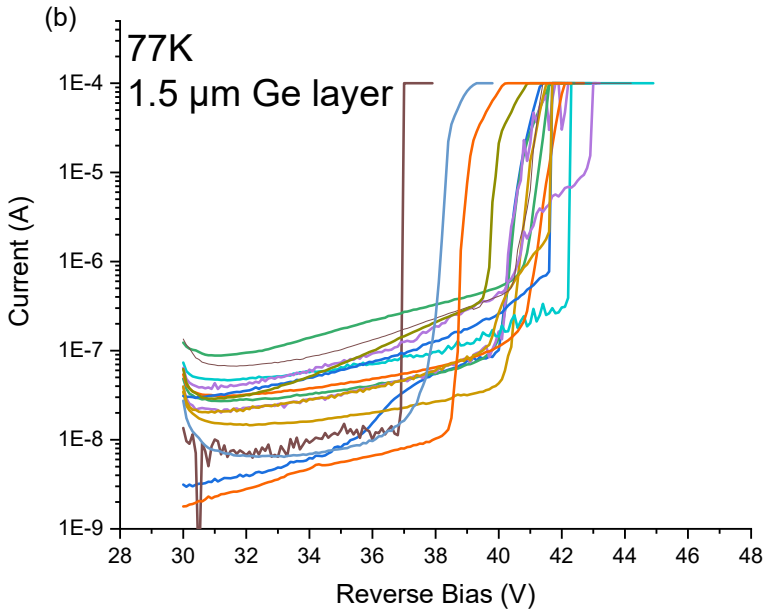
(b)
77K
1.5 μm Ge layer
Current (A)
1E-4
1E-5
1E-6
1E-7
1E-8
1E-9
28
30
32
34
36
38
40
42
44
46
48
Reverse Bias (V)

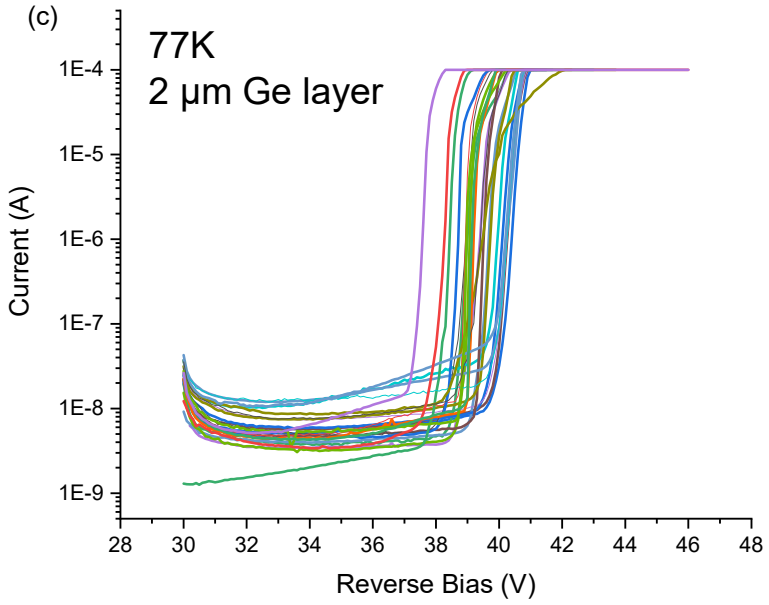


*Figure 5.19. Current-voltage characteristics for 50 µm and 100 µm diameter Ge-on-Si SPADs at 77 K, with (a) 1 µm, (b) 1.5 µm and (c) 2 µm thick germanium absorption layer.*

The yield of the 2 µm thick Ge devices was much higher than the other two thicknesses and showed stronger consistency in breakdown voltage. However, the 2 µm thick Ge devices did not survive the process of temperature cycling and when the devices were retested, they all showed open circuit behaviour. Nevertheless, we were still able to compare good IV characteristics from the 1 µm thick Ge device against a 2 µm device in Figure 5.20 and study the effect Ge thickness has on breakdown voltage and dark current. Because there was limited good IV data available, we cannot make accurate conclusions, but from the devices examined, the thicker Ge showed a lower dark current and similar breakdown voltage. Ideally a thicker Ge region would only increase the absorption and not adversely affect other characteristics of the device, and so having a similar breakdown voltage was desired, but a lower dark current was an unexpected improvement which should be investigated. This will help us to see whether the manufacturing process or the Ge thickness led to this result.

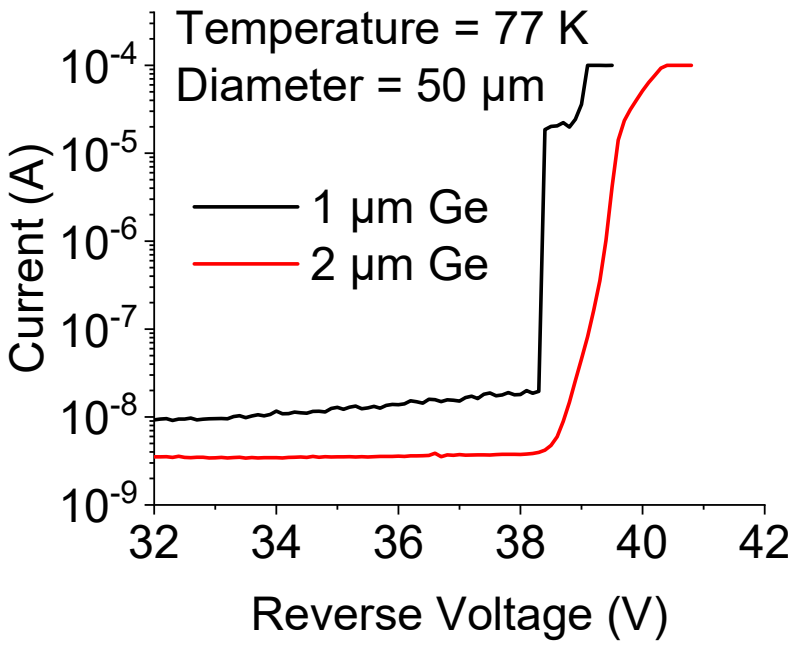


*Figure 5.20. Comparison between IV curves of 1 and 2 µm thick germanium absorber SPADs of 50 µm diameter.*

These findings indicated that another set of wafers were needed to be fabricated using longer etching times, as it is believed the lower yield and inconsistent IVs for the 1 and 1.5 µm thick Ge absorption layer SPADs was caused by insufficient etching causing shallow trenches.

The second set of different thickness Ge, Ge-on-Si SPADs was produced using a ground-signal-ground mesa design. Whereby a second ground contact is used on the surface of the device. These were fabricated using a similar method outlined in section 5.2 for a mesa design SPAD, the mesa design meant they could be produced more rapidly. To allow for a second top contact the methodology required to form the bottom contact is repeated on the top surface. The charge sheet doping is $3 \times 10^{12} cm^{-2}$.

Again 1, 1.5 and 2 µm thick germanium absorber layer Ge-on-Si SPADs were produced, with active area diameters of 200, 100, 50 and 26 µm. They are labelled 1B005, 2B005 and

3B005 corresponding with the 1, 1.5 and 2 µm thick germanium absorber layers. These were tested in the probe station to get an idea of the quality of devices and consistency in the fabrication process. They showed inconsistent IVs and early breakdown.

This information was fed back to the University of Glasgow in order to iterate the design and fabrication process. The purpose of the ground-signal-ground devices is to reduce the jitter in later stages of testing. The bottom of the wafer still acts as a ground contact and was used in our IV testing, but it is believed that by having a ground contact on the surface of the device the time taken between a photon hitting the active layer and an avalanche taking place will be reduced - thus, producing a quicker device and therefore reducing the jitter. When attempting to wire bond some of the better devices on the wafer we experienced further issues aside from the inconsistency in the devices. The contact pad on the surface of the devices was not securely attached which meant when wire bonding applying enough pressure to bond to the aluminium surface was enough to permanently damage the contact pad. This was confirmed by three separate companies specialising in wire bonding. This issue is believed to have come from a 'faulty batch' and not a fundamental issue with the template design.

When we are provided with a wafer of better fabricated ground-signal-ground devices, they will undergo the full characterisation and the improvement in jitter from using a standard top and bottom contact device like the previous SPAD which was characterised in section 5.4, will be quantified. We will also need to investigate whether the location of the ground contact has any effect on the SPDE, DCR and afterpulsing.

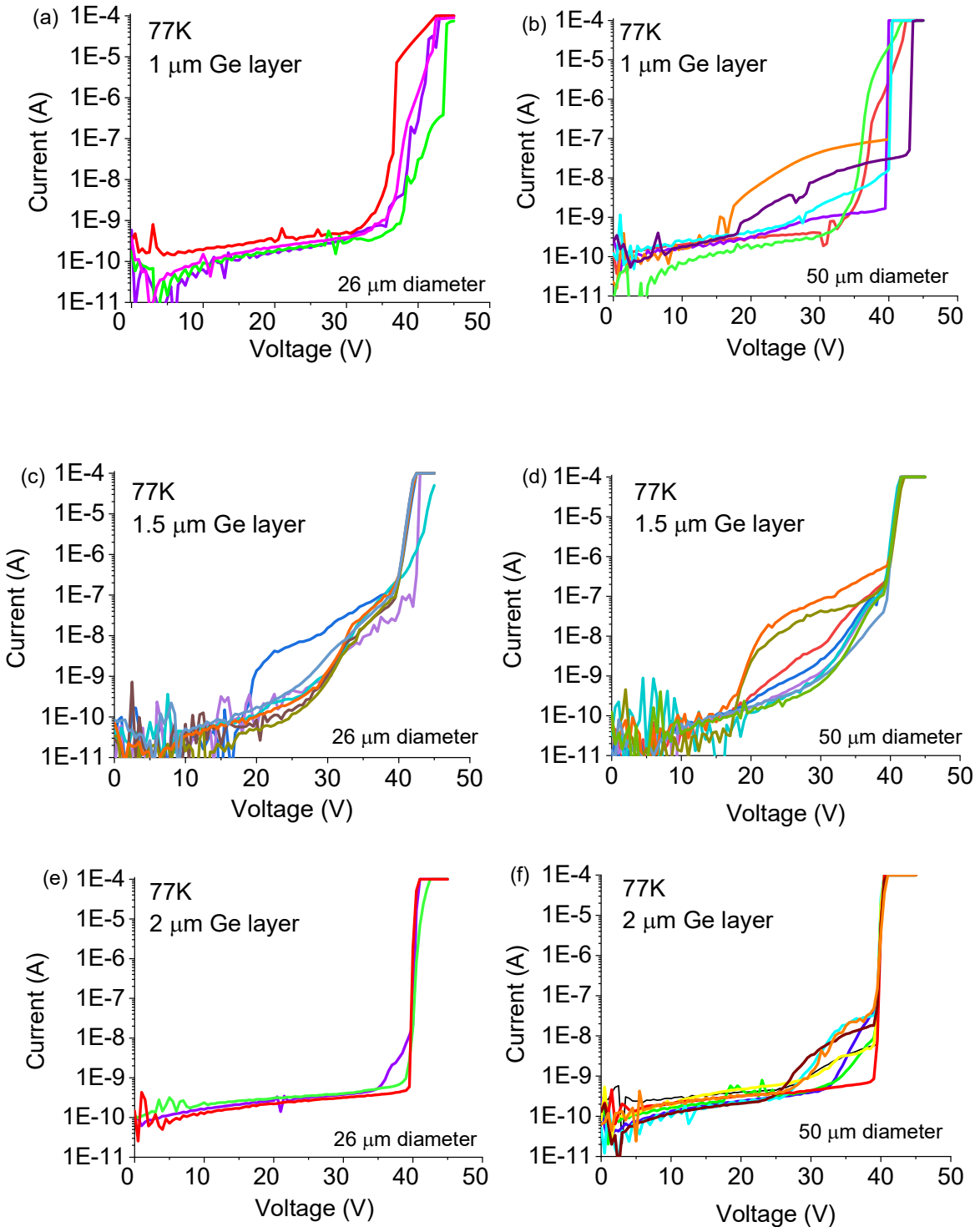


*Figure 5.21. IVs of 1, 1.5 and 2 μm thick Ge absorber layer Ge-on-Si SPADs with 26 and 50 μm diameters at 77 K.*

By comparing an IV characteristic from a previously successful 26 µm diameter device with a 1 µm Ge layer, to the best 26 µm device IV from the wafer with a 2 µm Ge layer, it is clear that although manufactured using slightly different methods at different times, the device with a Ge absorber layer twice the thickness produces IVs that are remarkably similar, as can be seen in Figure 5.22.

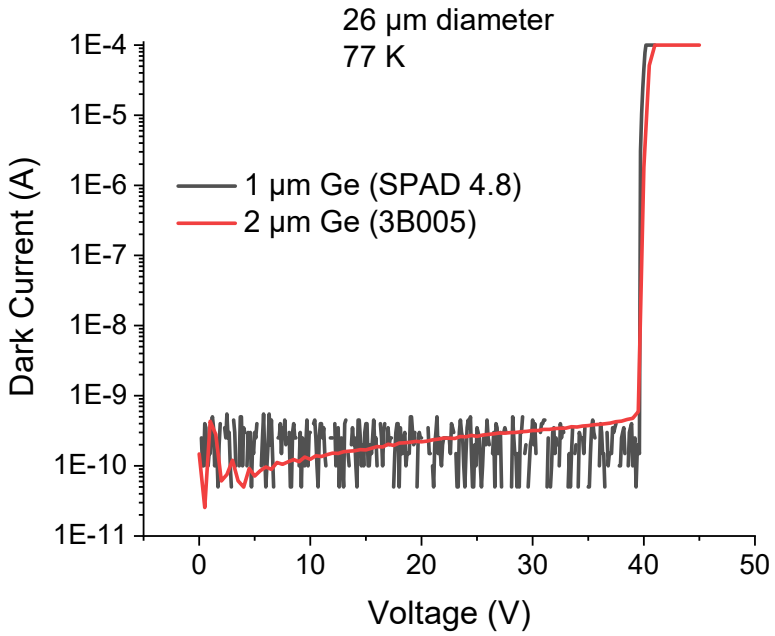


*Figure 5.22. Comparison between two differently manufactured SPADs, SPAD 4.8 has a 1 µm thick absorption layer (IV performed in cryostat) whereas 3B005 has twice the thickness Ge absorption layer (IV performed in probe station), the graph shows both IVs are similar.*

The University of Glasgow provided us with a final batch of 2 µm thickness Ge SPADs. These have a Germanium absorption layer of 2 µm thickness, a superpixel width of 15 µm and the charge sheet is doped with a boron ion implantation density of $3.0 \times 10^{12}$ $cm^{-2}$. Upon receiving the devices, the preliminary tests were performed where the best devices were gauged from running IV characteristics in dark conditions. These devices showed more consistent, and IVs that showed lower dark currents than the previous set of devices, Figure 5.23. However, the $V_{bd}$ is still the same as the 1 µm thick Ge devices.

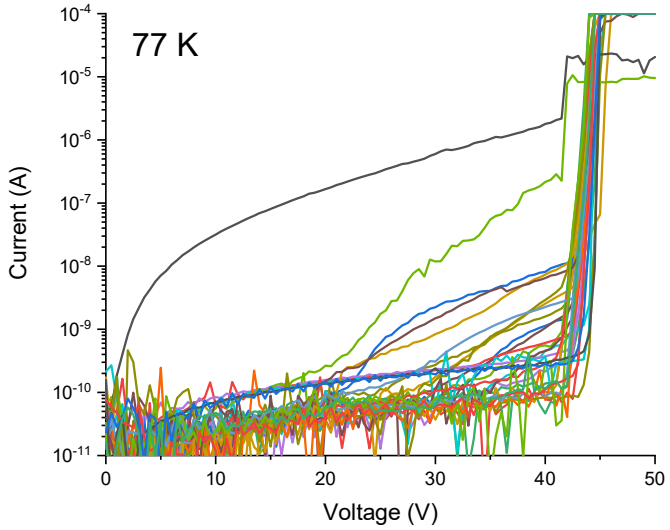


*Figure 5.23. Ge-on-Si SPAD with 2 µm thickness IVs taken in a probe station at 77K.*

These SPADs also showed a good photoresponse when illuminated with 1310 nm wavelength light from the supercontinuum laser, Figure 5.24. The photoresponse needs to be compared to that of the 1 µm thick Ge SPAD to see the improvement from the thicker absorption region.

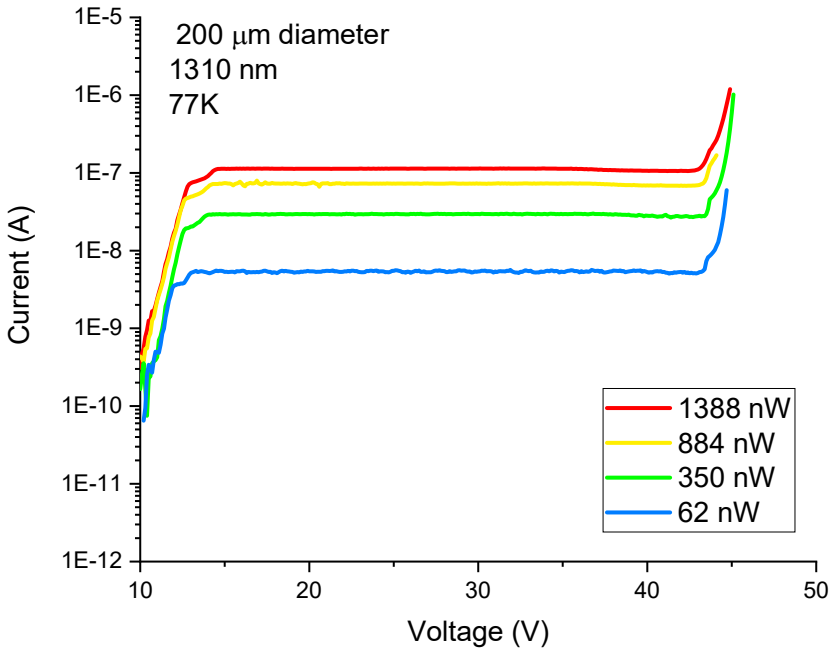


*Figure 5.24. The photoresponse of 2 μm thick Ge, Ge-on-Si SPAD after 1310 nm wavelength illumination at different power levels .*

We also looked at the forward bias for a few devices which showed the resistance was approximately millions of ohms.

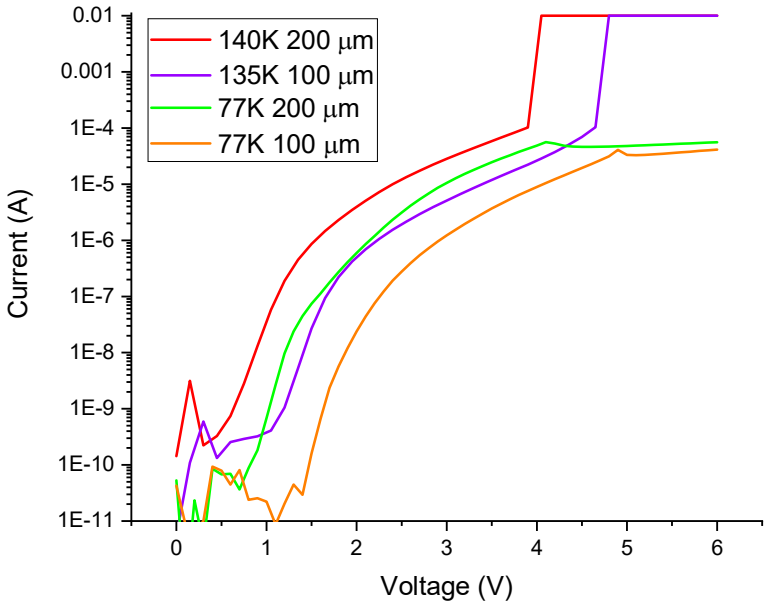

*Figure 5.25 Forward bias IV characteristics of two planar Ge-on-Si devices with a 2 µm thick Ge absorption layer and an active area diameter of 100 and 200 µm, at different temperatures.*

The resistance of the S4_3 FP_HD S39662 devices were considerably higher than the resistance found in the commercial Si SPAD which we also tested and found to have a resistance of approximately 1000s Ω (Silicon Geiger Mode Avalanche Photodiode, Laser Components). This can be seen in Figure 5.26.

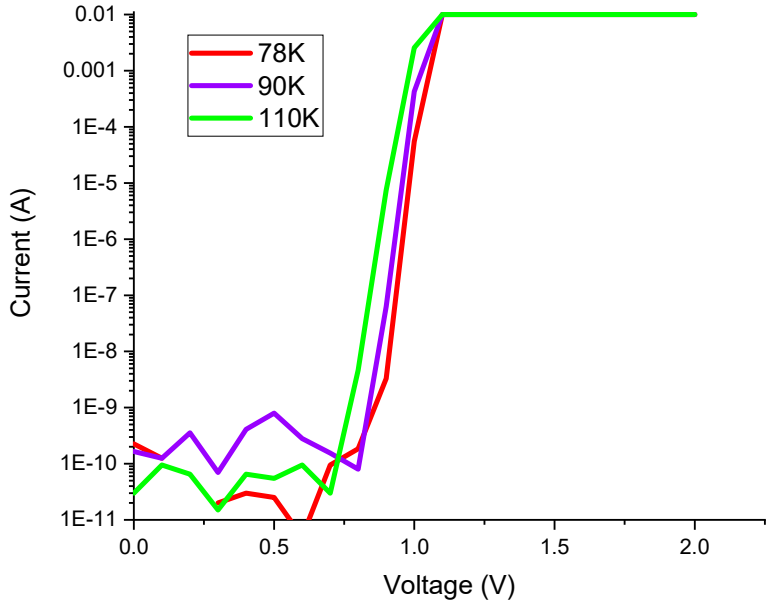


*Figure 5.26. Forward bias IV characteristics of a commercial Si SPAD at 78 K, 90 K and 110 K.*

Although many devices short circuited after temperature cycling some survived long enough to attempt to perform a SPDE and DCR measurement however the constant degradation of the devices meant collecting any reliable results was unfortunately unsuccessful.

### 5.6 Investigation of Spectral Responsivity

As extending the wavelength of operation of standard silicon SPADs whilst maintaining their CMOS compatibility is the main aim of this research into Ge-on-Si, it was necessary to perform photoresponse measurements on different APD and SPAD materials to show the effect incorporating a Ge absorption layer onto a Si multiplication region has when compared to different devices. With the aim of showing the improvement in the operating wavelength range when compared to an all-silicon device, and the potential that thicker Ge layers have to increase the operating range when compared to an all-germanium device. As InGaAs/InP is the main competition for a Ge-on-Si SPAD it was worth investigating the spectral photoresponse to see if our Ge-on-Si devices compares with the of InGaAs/InP devices. Because SPAD 4.8 with 1 μm Ge layer and 15 μm superpixel, which we performed our DCR and SPDE measurements on initially, had degraded, we used a 100 μm active area device from a different quadrant with a 5 μm superpixel to measure the photoresponse, as these devices had been stored separately and under vacuum. Although its IV characteristics showed it had a higher dark current and less consistency across the devices. We were able to find a handful of promising devices.

As these devices have a 1 μm thick Ge layer, this device was hypothesised to absorb less than 50% of incident photons due to the inadequate thickness of the Ge absorption layer, and with a 2 μm thick layer, using Beer-Lamberts law the absorption should increase to at least 70 % [40]. Which prompted the fabrication of SPADs with a 2 μm thick Ge layer, we used a 200 μm active area Ge-on-Si SPAD for photoresponse testing as this size of device was most robust. By performing the photoresponse of these two devices we can study the effect of thickening the Ge. As mentioned, it would also form a good point of reference to use a Ge APD (Germanium Photodiode, Optoelectronics [62]) and Si SPAD (Laser components [63]) device to demonstrate the increased wavelength sensitivity as an improvement from pure silicon whilst the Ge device would show the potential wavelengths that could be achieved with a thicker absorption layer. Both will give a good marker of the progression of our Ge-on-Si devices. The Ge APD has an active area of 40 μm whilst the Si SPAD has an active area of 500 μm, both large enough for the laser light to be completely incident on the device so whilst the devices are vastly different sizes it should not affect the number of

photons incident on them. We also investigated the spectral response of an InGaAs/InP device produced by Princeton Lightwave with an 80 μm active area, as this material device forms the main competition for our Ge-on-Si devices with its photoresponse ranging between 900 and 1700 nm. And so, a comparison would be a good measure of whether our Ge-on-Si SPADs have a competitive photoresponsivity.

To perform the experiment as reliably as possible we measured the photoresponse at the same range of temperatures and using a voltage where the gain of the device was set to unity. For the Ge, Si, InGaAs/InP this was at 10 V, 25 V and 39 V respectively. And for the 1 μm Ge layer and 2 μm Ge layer Ge-on-Si SPADs this was at 25 V for both. Most of the photoresponse measurements were taken by illuminating the device with light from a supercontinuum laser in a dark room and measuring an IV. A power meter was used to calculate the attenuation of the system at different wavelengths and measure the power throughout the experiment. Then by reading the current off the IV at the previously chosen voltage we could use the data to calculate the response of the device. For devices with a higher dark current or higher temperature readings where it was difficult to see the effect light exposure was having on the current from the IV, we used a lock-in-amplifier. This was connected across the device and read the voltage in real time, by using a 50/50 chopper it removed the contribution of the dark current. To analyse the results the following equation was used Equation 5.2. Where I is photocurrent and P, the incident optical power.

$$Responsivity = \frac{I}{P} \tag{5.2}$$

When analysing the lock-in-amplifier results the voltage was divided by 10,000, corresponding to the 10 kΩ resistor used, and divided again by a factor of 0.45 to account for the shape of the signal wave within the lock-in-amplifier. The results are shown below in Figures 5.27 - 5.31.

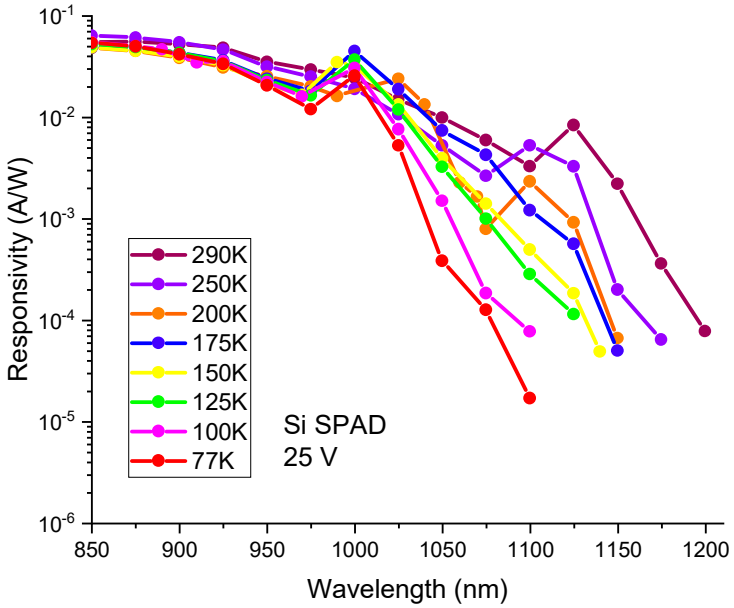


*Figure 5.27. Spectral responsivity of a commercial Si SPAD at temperatures from 290 K – 77 K. Taken at a voltage of 25 V with gain = 1.*

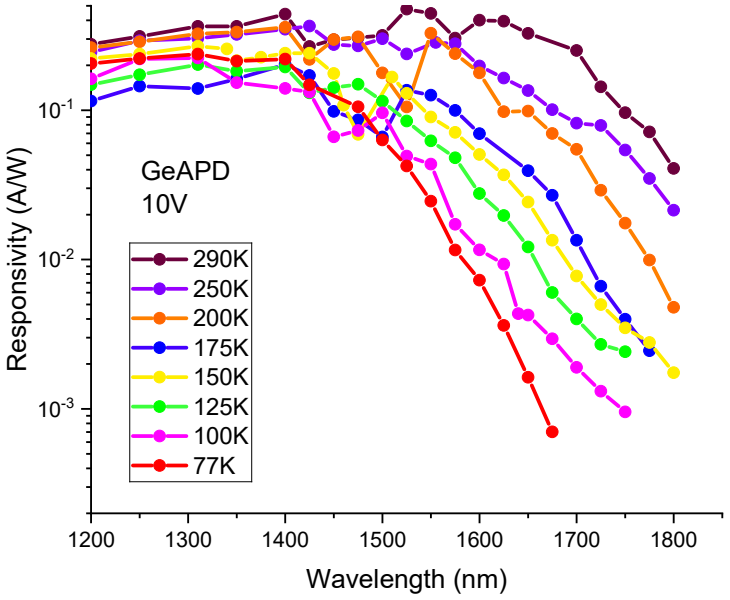


*Figure 5.28. Spectral responsivity of a commercial Ge APD at temperatures from 290 K – 77 K. Taken at a voltage of 10 V with gain = 1.*

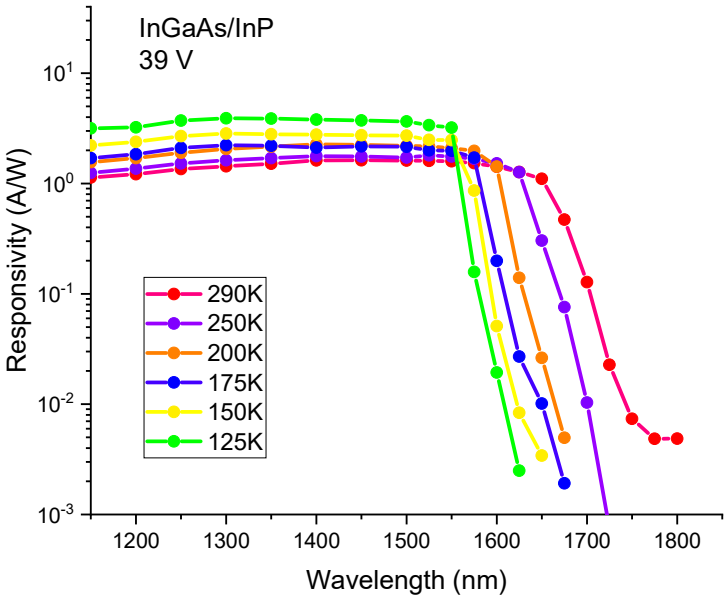


*Figure 5.29. Spectral responsivity of a prototype InGaAs/InP APD at temperatures from 290 K – 125 K. Taken at a voltage of 39 V with gain = 1.*

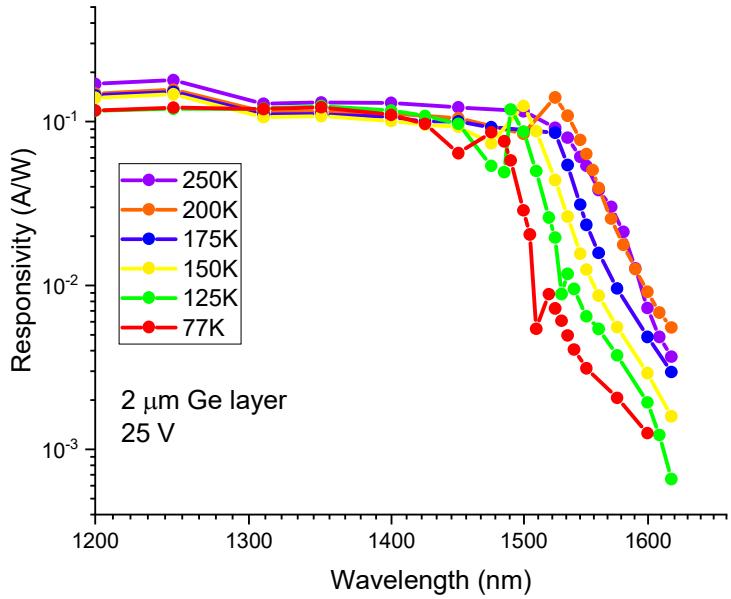


*Figure 5.30. Spectral responsivity of a Ge-on-Si SPAD with a 2 μm thick Ge absorption region at temperatures from 250 K – 77 K. Taken at a voltage of 25 V with gain = 1.*

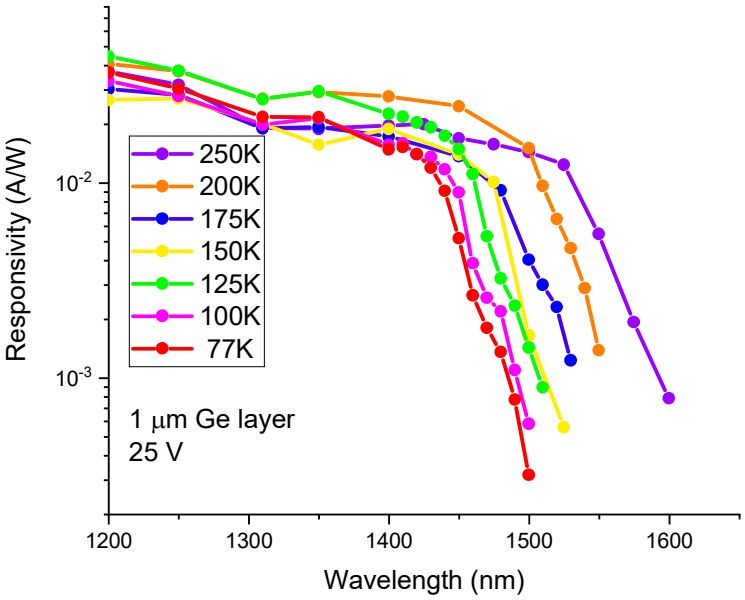


*Figure 5.31. Spectral responsivity of a Ge-on-Si SPAD with a 1 μm thick Ge absorption region at temperatures from 250 K – 77 K. Taken at a voltage of 25 V with gain = 1.*

The manufactures of the Si SPAD indicate approximately 30-40 A/W at a gain of approximately 100 [63], so these results are roughly consistent with the expected responsivity. To compare the results the photoresponse of the devices at different temperatures they are plotted in Figure 5.32 (a)-(b), excluding the Si SPAD as it cuts off before 1200 nm which is the starting point for the other devices. The results have also been normalised to give a fairer comparison as though the devices have similar efficiencies, which allows us to isolate the comparison, to just the effect the absorption material and thickness has on the photoresponse.

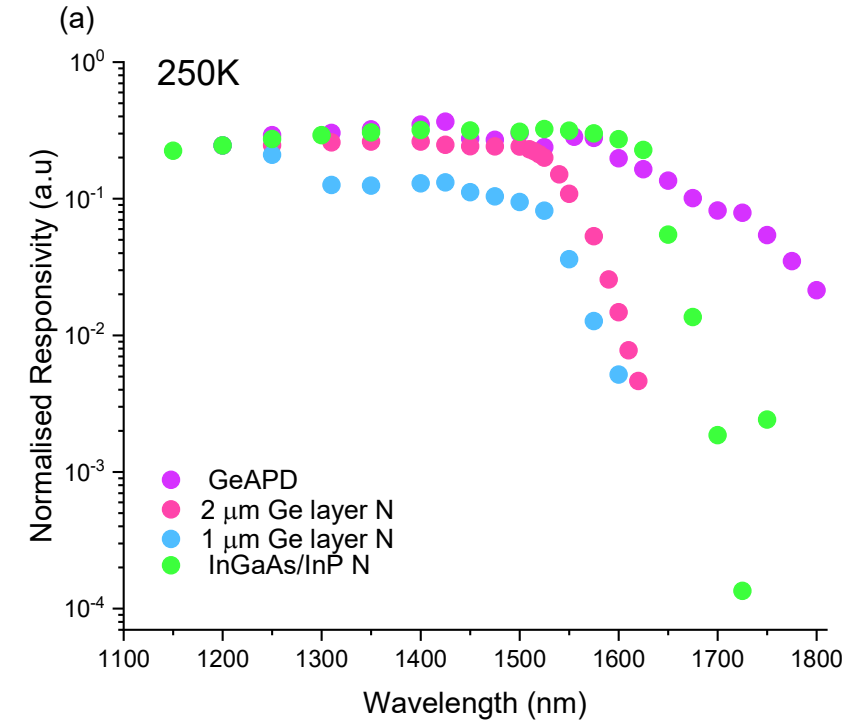
(a)
250K
Normalised Responsivity (a.u)
Wavelength (nm)
GeAPD
2 μm Ge layer N
1 μm Ge layer N
InGaAs/InP N

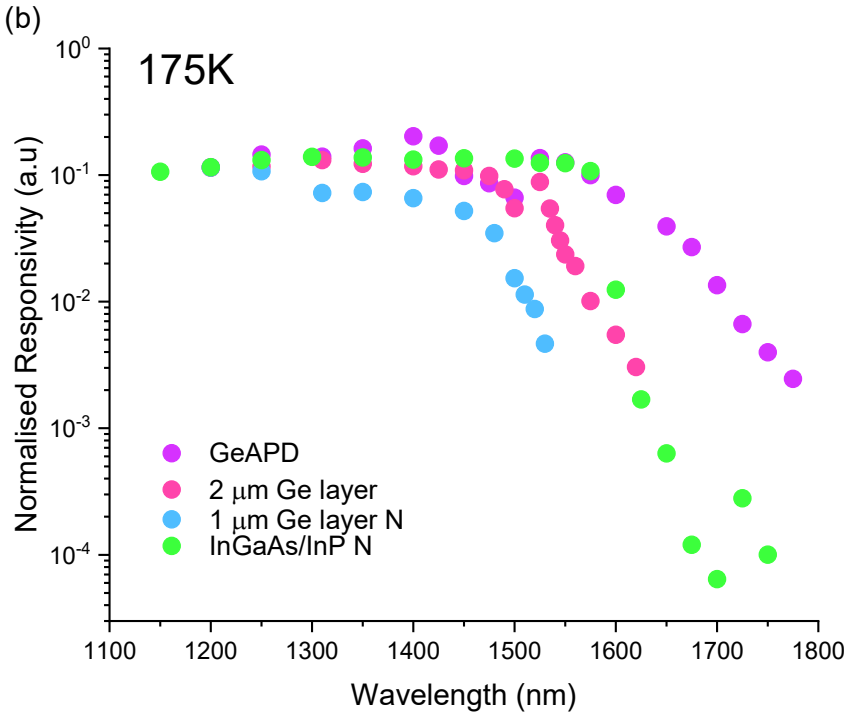
(b)
175K
Normalised Responsivity (a.u)
Wavelength (nm)
GeAPD
2 μm Ge layer
1 μm Ge layer N
InGaAs/InP N

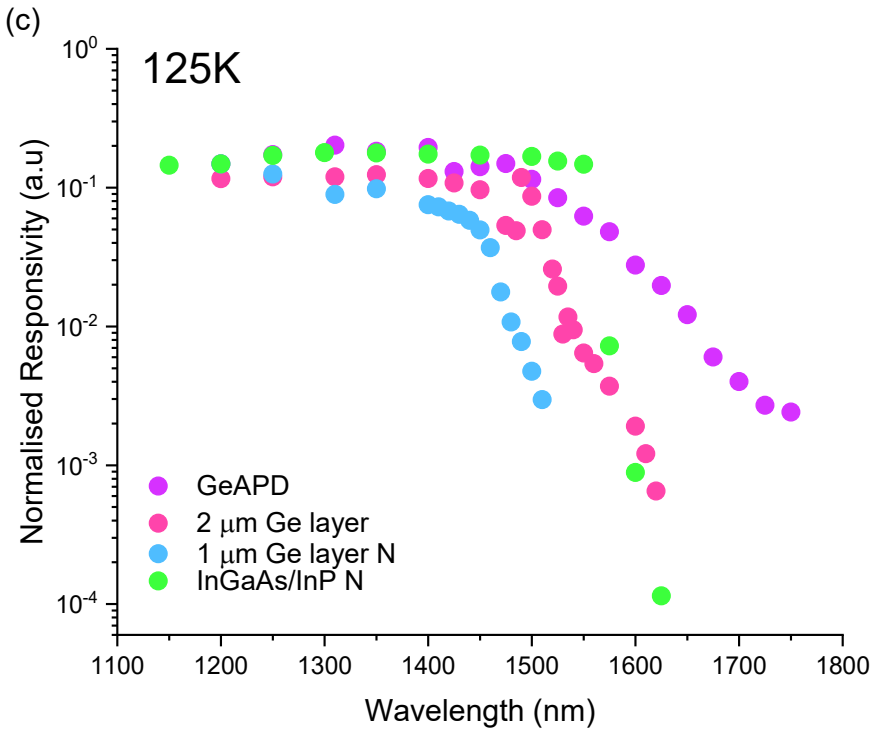


*Figure 5.32. Photoresponse comparison between Ge, Si and Ge-on-Si APDs and SPADs at different temperatures with gain = 1, normalised to the Ge APD results, with an N following the device name to dictate the results which have been adjusted.*

From these results we can conclude, firstly, that regardless of the Ge thickness, Ge-on-Si devices showed a considerable improvement from pure Si in wavelength responsivity above 1200 nm with both the 1 µm and 2 µm Ge layer Ge-on-Si SPADs showing no decline in responsivity well up to 1400 nm. Although there was limited information available on the Ge APD it is a reach through design and it is probable that it has a highly doped Ge junction which has contributed to an increase in wavelength responsivity for the Ge APD, as excessive doping leads to degenerate semi-conductor behaviour and bandgap narrowing as well as excess noise. So, whilst the pure Ge APD showed the best responsivity at longer wavelengths, as expected, we were surprised to see such a vast improvement between the 1 µm and 2 µm Ge layer SPADs, bringing the 2 µm Ge layer device results almost in-line with the InGaAs/InP device. This shows we can get a similar wavelength detection range from our Ge-on-Si devices with a thicker Ge layer and shows promise that the compatibility and

cost will make the Ge-on-Si devices much more desirable than the currently popular InGaAs/InP devices.

### 5.7 Conclusions and Future Work

In this chapter the design, fabrication and characterisation of planar Ge-on-Si SPADs are reported. Ge-on-Si devices with a 1 μm thick Ge layer were characterised, their IVs, SPDE and DCR and Jitter were calculated at temperatures from 77 K to 150 K for both 26 μm and 50 μm devices. The highest SPDE achieved was 30 % at a wavelength of 1310 nm at 125 K and an excess bias of 6.5 %. The DCRs under these conditions were typically between $1 \times 10^3$ and $1 \times 10^6$ cps, with the lowest DCRs at 100 K. The lowest jitter observed was 126 ps at 150 K and an excess bias of 5.5 %. The smallest NEP value was calculated to be $4 \times 10^{-17} WHz^{-1/2}$ at a wavelength of 1310 nm. This successfully demonstrated the improvement on previous mesa design as the planar Ge-on-Si achieved higher SPDE, lower DCR and smaller NEP values than reported for previous Ge-on-Si mesa devices which were reported to have an SPDE of 4% at $\lambda = 1310$ nm, DCR of $6 \times 10^6$ cps or higher and an NEP of $1 \times 10^{-14} WHz^{-1/2}$ [58]. At the time of writing, these devices presented in this Chapter have demonstrated the lowest NEP and jitter in the short-wave infrared of any Ge-on-Si SPAD.

When compared to InGaAs/InP technology the SPDEs are in a similar range, with InGaAs/InP based SPADs typically ranging from 20 % to 55 % in the SWIR, however InGaAs/InP SPADs worked at temperatures over 220 K [36-40]. Whereas the planar Ge-on-Si SPADs investigated in this Chapter were unable to be operated and therefore characterised reliably over 175 K. Using the DCR Arrhenius plot the mean activation energy of the Ge-on-Si SPADs calculated was 39.7 meV. This did not correspond with the activation energies one expects from silicon or germanium which are typically hundreds of meVs [60, 61, 64]. Except it is known that growing Ge onto Si introduces a strain at the interface and therefore the traps contributing to the activation energy may be altered by this strain, it is also known that the direction of crystal growth effects the activation energy too [65]. Thus, it is difficult to conclude the activation energy expected from these devices and more research into the methodology used to calculate the activation energy is discussed in Chapter 6.

The characterisation of the 1 μm thick Ge layer SPADs was performed at 1310 nm and to improve the efficiency of Ge-on-Si SPADs at this and longer wavelengths, thicker Ge absorption layers were used in a new set of devices this allowed a photoresponse comparison to be made between 1 and 2 μm thick Ge absorption layer Ge-on-Si SPADs. The photoresponse of Si, Ge and InGaAs/InP photodetectors were also investigated, and it was found that whilst the Ge-on-Si devices did not exhibit the same responsivity as a Ge APD there was a notable improvement between the responsivity of the 1 μm and the 2 μm thick Ge layer SPADs, bringing the 2 μm Ge layer SPADs into competition with a typical InGaAs/InP APDs photoresponse. And given InGaAs/InP devices perform well into the SWIR this suggests our 2 μm Ge-on-Si devices might be suitable for high efficiency detection above 1310 nm [36-40]. The next steps in improving Ge-on-Si SPADs would be performing further testing on a planar Ge-on-Si SPAD with 2 μm thick Ge, with optical access, good quality bond pads, consistent IVs and one which can survive temperature cycling. When we receive such devices, the following tasks should be prioritised. The characterisation of a working Ge-on-Si SPAD at different wavelengths; it is proposed that this is performed at wavelengths of 1550, 940 and 905 nm. The previously mentioned experiments and results were all performed at 1310 nm wavelength with only 1 μm Ge layer and the next stage of research should be repeating the measurements at a range of wavelengths which would enable us to identify the effect of wavelength on the DCR and SPDE. Studying the devices' performance at $\lambda = 1550$ nm would help us to predict the devices potential for longer wavelength applications such as low loss optical fibre communication. At 905 nm and 940 nm wavelength their potential for use in automobile sensors can also be studied.

From the photoresponse results it is clear that our Ge-on-Si devices do not have the same detection range as pure Ge, it would be fascinating to see the maximum thickness of Ge we could use before it stopped being the limiting factor for the responsivity of the device. Using an even thicker germanium layer could also lead to a considerable improvement in operational wavelength due to increasing the tensile strain of the device, this is due to the difference in thermal expansion coefficients at the interface. Which has the effect of

decreasing the bandgap of the materials involved [66]. It is clear there are many aspects of Ge-on-Si SPAD design that can be fruitfully researched in the coming years.

**References**


[1] R. Tobin, A. Halimi, A. McCarthy, M. Laurenzis, F. Christnacher, G.S. Buller, *Three-dimensional single-photon imaging through obscurants*, Opt. Express, 27 (2019) 4590-4611.

[2] V. Fathipour, S. Wheaton, W.E. Johnson, H. Mohseni, *Modeling of a sensitive time-of-flight flash LiDAR system*, International Society for Optics and Photonics, pp. 99740N.

[3] N. Gisin, R.T. Thew, *Quantum communication technology*, Electronics letters, 46 (2010) 965-967.

[4] S.M. Johnson, E. Dial, M. Razeghi, *High-speed free space optical communications based on quantum cascade lasers and type-II superlattice detectors*, International Society for Optics and Photonics, pp. 1128814.

[5] M. Planck, *On an Improvement of Wien's Equation for the Spectrum*, Verhandlungen der Deutschen Physikalischen Gesellschaft, 2 (1900).

[6] M. Planck, *On the Theory of the Energy Distribution Law of the Normal Spectrum,* Verhandlungen der Deutschen Physikalischen Gesellschaft, 2 (1900).

[7] A. Einstein, *On a heuristic point of view concerning the production and transformation of light*, Annalen der Physik, 17 (1905) 132-148.

[8] R. Daniel, R. Almog, A. Ron, S. Belkin, Y.S. Diamand, *Modeling and measurement of a whole-cell bioluminescent biosensor based on a single photon avalanche diode*, Biosens Bioelectron, 24 (2008) 888-893.

[9] C. Bruschini, H. Homulle, I.M. Antolovic, S. Burri, E. Charbon, *Single-photon avalanche diode imagers in biophotonics: review and outlook*, Light: Science & Applications, 8 (2019) 87.

[10] M.A. Karami, M. Ansarian, *Neural Imaging Using Single-Photon Avalanche Diodes*, Basic Clin Neurosci, 8 (2017) 19-26.

[11] S. Bellis, C. Jackson, A. König, *Photon counting sensors for medical and biophotonic applications*, Laser+Photnik, 5 (2005) 34-38.

[12] R.H. Hadfield, *Single-photon detectors for optical quantum information applications*, Nature Photonics, 3 (2009) 696-705.
[13] R.J. Collins, R. Amiri, M. Fujiwara, T. Honjo, K. Shimizu, K. Tamaki, M. Takeoka, E. Andersson, G.S. Buller, M. Sasaki, *Experimental transmission of quantum digital signatures over 90 km of installed optical fiber using a differential phase shift quantum key distribution system*, Opt. Lett., 41 (2016) 4883-4886.
[14] R.J. Collins, R. Amiri, M. Fujiwara, T. Honjo, K. Shimizu, K. Tamaki, M. Takeoka, M. Sasaki, E. Andersson, G.S. Buller, *Experimental demonstration of quantum digital signatures over 43 dB channel loss using differential phase shift quantum key distribution*, Scientific Reports, 7 (2017) 3235.
[15] B. Korzh, C.C.W. Lim, R. Houlmann, N. Gisin, M.J. Li, D. Nolan, B. Sanguinetti, R. Thew, H. Zbinden, *Provably secure and practical quantum key distribution over 307 km of optical fibre*, Nature Photonics, 9 (2015) 163-168.
[16] E. Diamanti, H.-K. Lo, B. Qi, Z. Yuan, *Practical challenges in quantum key distribution*, npj Quantum Information, 2 (2016) 16025.
[17] A. Pljonkin, P.K. Singh, *The Review of the Commercial Quantum Key Distribution System*, 2018 Fifth International Conference on Parallel, Distributed and Grid Computing (PDGC)2018, pp. 795-799.
[18] P. Kok, W.J. Munro, K. Nemoto, T.C. Ralph, J.P. Dowling, G.J. Milburn, *Linear optical quantum computing with photonic qubits*, Reviews of Modern Physics, 79 (2007) 135-174.
[19] E. Knill, R. Laflamme, G.J. Milburn, *A scheme for efficient quantum computation with linear optics*, Nature, 409 (2001) 46-52.
[20] J.L. Brien, *Optical Quantum Computing*, Science, 318 (2007) 1567.
[21] Q. Zhao, L. Xia, C. Wan, J. Hu, T. Jia, M. Gu, L. Zhang, L. Kang, J. Chen, X. Zhang, P. Wu, *Long-haul and high-resolution optical time domain reflectometry using superconducting nanowire single-photon detectors*, Scientific Reports, 5 (2015) 10441.
[22] J.C. Christopher, D. Ivo Pietro, K. Stefan, M. Ingmar, G.S. Alastair, *Metrology of single-photon sources and detectors: a review*, Optical Engineering, 53 (2014) 1-17.
[23] A.M. Pawlikowska, A. Halimi, R.A. Lamb, G.S. Buller, *Single-photon three-dimensional imaging at up to 10 kilometers range*, Opt. Express, 25 (2017) 11919-11931.

[24] R. Tobin, A. Halimi, A. McCarthy, X. Ren, K. McEwan, S. McLaughlin, G. Buller, *Long-range depth profiling of camouflaged targets using single-photon detection*, Optical Engineering, 57 (2017) 031303.
[25] J. Tachella, Y. Altmann, N. Mellado, A. McCarthy, R. Tobin, G.S. Buller, J.-Y. Tourneret, S. McLaughlin, *Real-time 3D reconstruction from single-photon lidar data using plug-and-play point cloud denoisers*, Nature Communications, 10 (2019) 4984.
[26] X. Ren, P.W.R. Connolly, A. Halimi, Y. Altmann, S. McLaughlin, I. Gyongy, R.K. Henderson, G.S. Buller, *High-resolution depth profiling using a range-gated CMOS SPAD quanta image sensor*, Opt. Express, 26 (2018) 5541-5557.
[27] A. Maccarone, F. Mattioli Della Rocca, A. McCarthy, R. Henderson, G.S. Buller, *Three-dimensional imaging of stationary and moving targets in turbid underwater environments using a single-photon detector array*, Opt. Express, 27 (2019) 28437-28456.
[28] I. Takai, H. Matsubara, M. Soga, M. Ohta, M. Ogawa, T. Yamashita, *Single-Photon Avalanche Diode with Enhanced NIR-Sensitivity for Automotive LIDAR Systems*, Sensors, 16 (2016) 459.
[29] S. Chan, A. Halimi, F. Zhu, I. Gyongy, R.K. Henderson, R. Bowman, S. McLaughlin, G.S. Buller, J. Leach, *Long-range depth imaging using a single-photon detector array and non-local data fusion*, Scientific Reports, 9 (2019) 8075.
[30] A. Arnulf, J. Bricard, E. Curé, C. Véret, *Transmission by Haze and Fog in the Spectral Region 0.35 to 10 Microns**, J. Opt. Soc. Am., 47 (1957) 491-498.
[31] R. Tobin, A. Halimi, A. McCarthy, P.J. Soan, G.S. Buller, *Robust real-time 3D imaging of moving scenes through atmospheric obscurant using single-photon LiDAR*, Scientific Reports, 11 (2021) 11236.
[32] U.o. Leicester, *The Speed of Sound in Air*.
[33] A.M. Wallace, A. Halimi, G.S. Buller, *Full waveform LiDAR for adverse weather conditions*, IEEE Transactions on Vehicular Technology, (2020) 1-1.
[34] F. Thorburn, X. Yi, Z. Greener, J. Kirkoda, R. Millar, L. Huddleston, D. Paul, G. Buller, *Ge-on-Si single-photon avalanche diode detectors for short-wave infrared wavelengths*, Journal of Physics: Photonics, (2021).
[35] A. Lacaita, S. Cova, F. Zappa, P.A. Francese, *Subnanosecond single-photon timing with commercially available germanium photodiodes*, Opt. Lett., 18 (1993) 75-77.

[36] S. Pellegrini, R.E. Warburton, L.J.J. Tan, N. Jo Shien, A.B. Krysa, K. Groom, J.P.R. David, S. Cova, M.J. Robertson, G.S. Buller, *Design and performance of an InGaAs-InP single-photon avalanche diode detector*, IEEE Journal of Quantum Electronics, 42 (2006) 397-403.
[37] J.C. Campbell, W. Sun, Z. Lu, M.A. Itzler, X. Jiang, *Common-Mode Cancellation in Sinusoidal Gating With Balanced InGaAs/InP Single Photon Avalanche Diodes*, IEEE Journal of Quantum Electronics, 48 (2012) 1505-1511.
[38] A. Tosi, N. Calandri, M. Sanzaro, F. Acerbi, Low-Noise, *Low-Jitter, High Detection Efficiency InGaAs/InP Single-Photon Avalanche Diode*, IEEE Journal of Selected Topics in Quantum Electronics, 20 (2014) 192-197.
[39] L.C. Comandar, B. Fröhlich, J.F. Dynes, A.W. Sharpe, M. Lucamarini, Z.L. Yuan, R.V. Penty, A.J. Shields, *Gigahertz-gated InGaAs/InP single-photon detector with detection efficiency exceeding 55% at 1550 nm*, Journal of Applied Physics, 117 (2015) 083109.
[40] P. Vines, K. Kuzmenko, J. Kirdoda, D.C.S. Dumas, M.M. Mirza, R.W. Millar, D.J. Paul, G.S. Buller, *High performance planar germanium-on-silicon single-photon avalanche diode detectors*, Nature Communications, 10 (2019) 1086.
[41] Z.L. Yuan, A.R. Dixon, J.F. Dynes, A.W. Sharpe, A.J. Shields, *Gigahertz quantum key distribution with InGaAs avalanche photodiodes*, Applied Physics Letters, 92 (2008) 201104.
[42] C. Yu, M. Shangguan, H. Xia, J. Zhang, X. Dou, J.-W. Pan, *Fully integrated free-running InGaAs/InP single-photon detector for accurate lidar applications*, Opt. Express, 25 (2017) 14611-14620.
[43] J. Liu, Y. Xu, Z. Wang, Y. Li, Y. Gu, Z. Liu, X. Zhao, *Reducing afterpulsing in InGaAs (P) single-photon detectors with hybrid quenching*, Sensors, 20 (2020) 4384.
[44] A. McCarthy, X. Ren, A. Della Frera, N.R. Gemmell, N.J. Krichel, C. Scarcella, A. Ruggeri, A. Tosi, G.S. Buller, *Kilometer-range depth imaging at 1550 nm wavelength using an InGaAs/InP single-photon avalanche diode detector*, Opt. Express, 21 (2013) 22098-22113.
[45] J. Zhang, M.A. Itzler, H. Zbinden, J.-W. Pan, *Advances in InGaAs/InP single-photon detector systems for quantum communication*, Light: Science & Applications, 4 (2015) e286-e286.

[46] A.Y. Loudon, P.A. Hiskett, G.S. Buller, R.T. Carline, D.C. Herbert, W.Y. Leong, J.G. Rarity, *Enhancement of the infrared detection efficiency of silicon photon-counting avalanche photodiodes by use of silicon germanium absorbing layers*, Opt. Lett., 27 (2002) 219-221.
[47] R.E. Warburton, G. Intermite, M. Myronov, P. Allred, D.R. Leadley, K. Gallacher, D.J. Paul, N.J. Pilgrim, L.J.M. Lever, Z. Ikonic, R.W. Kelsall, E. Huante-Cerón, A.P. Knights, G.S. Buller, *Ge-on-Si Single-Photon Avalanche Diode Detectors: Design, Modeling, Fabrication, and Characterization at Wavelengths 1310 and 1550 nm*, IEEE Transactions on Electron Devices, 60 (2013) 3807-3813.
[48] A. Tosi, A.D. Mora, F. Zappa, S. Cova, Germanium and InGaAs/InP SPADs for single-photon detection in the near-infrared, SPIE2007.
[49] S. Butera, *InAs avalanche photodiodes*, (2015).
[50] K. Kuzmenko, P. Vines, A. Halimi, R.J. Collins, A. Maccarone, A. McCarthy, Z.M. Greener, J. Kirdoda, D.C.S. Dumas, L.F. Llin, M.M. Mirza, R.W. Millar, D.J. Paul, G.S. Buller, *3D LIDAR imaging using Ge-on-Si single-photon avalanche diode detectors*, Opt. Express, 28 (2020) 1330-1344.
[51] J. Kirdoda, *Germanium on silicon single photon avalanche detectors*, (2019).
[52] F.E. Thorburn, L.L. Huddleston, J. Kirdoda, R.W. Millar, L. Ferre-Llin, X. Yi, D.J. Paul, G.S. Buller, *High efficiency planar geometry germanium-on-silicon single-photon avalanche diode detectors*, International Society for Optics and Photonics, pp. 113860N.
[53] E.A.G. Webster, R.K. Henderson, *A TCAD and Spectroscopy Study of Dark Count Mechanisms in Single-Photon Avalanche Diodes*, IEEE Transactions on Electron Devices, 60 (2013) 4014-4019.
[54] J.B. Pawley*, Handbook of Biological Confocal Microscopy Springer US*, Boston MA, 2006.
[55] F. Zappa, M. Ghioni, S. Cova, C. Samori, A.C. Giudice, *An integrated active-quenching circuit for single-photon avalanche diodes*, IEEE Transactions on Instrumentation and Measurement, 49 (2000) 1167-1175.
[56] R. Mita, G. Palumbot, G. Fallica, *A fast active quenching and recharging circuit for single-photon avalanche diodes*, Proceedings of the 2005 European Conference on Circuit Theory and Design, 2005.2005, pp. III/385-III/388 vol. 383.

[57] N.J.D. Martinez, M. Gehl, C.T. Derose, A.L. Starbuck, A.T. Pomerene, A.L. Lentine, D.C. Trotter, P.S. Davids, *Single photon detection in a waveguide-coupled Ge-on-Si lateral avalanche photodiode*, Opt. Express, 25 (2017) 16130-16139.
[58] R.E. Warburton, G. Intermite, M. Myronov, P. Allred, D.R. Leadley, K. Gallacher, D.J. Paul, N.J. Pilgrim, L.J. Lever, Z. Ikonic, *Ge-on-Si single-photon avalanche diode detectors: design, modeling, fabrication, and characterization at wavelengths 1310 and 1550 nm*, IEEE Transactions on Electron Devices, 60 (2013) 3807-3813.
[59] L.F. Llin, J. Kirdoda, F. Thorburn, L.L. Huddleston, Z.M. Greener, K. Kuzmenko, P. Vines, D.C.S. Dumas, R.W. Millar, G.S. Buller, D.J. Paul, *High sensitivity Ge-on-Si single-photon avalanche diode detectors*, Opt. Lett., 45 (2020) 6406-6409.
[60] J. Tauc, *Determination of the optical activation energy of germanium by the method of photoelectric lines*, Cechoslovackij fiziceskij zurnal, 4 (1954) 311-314.
[61] V.V.N. Obreja, A.C. Obreja, *Activation energy values from the temperature dependence of silicon PN junction reverse current and its origin*, physica status solidi (a), 207 (2010) 1252-1256.
[62] GDP Optoelectronics Corps.
[63] Laser Components.
[64] S.K. Estreicher, D.J. Backlund, C. Carbogno, M. Scheffler, *Activation Energies for Diffusion of Defects in Silicon: The Role of the Exchange‐Correlation Functional,* Angewandte Chemie International Edition, 50 (2011) 10221-10225.
[65] G.S. Hubbard, *Electrical properties of dislocations in ultra-pure germanium*, (1979).
[66] Y.S. Li, J. Nguyen, *Tensilely Strained Ge Films on Si Substrates Created by Physical Vapor Deposition of Solid Sources*, Scientific Reports, 8 (2018) 16734.

# Chapter 6. Afterpulsing

## 6.1 Introduction to Afterpulsing

Afterpulsing is an undesirable phenomenon found in SPADs in which an event – possibly caused by an incident photon – leads to a further false event at some time after the initial detection. During a detection event, the avalanche current results in a large number of carriers flowing through the device. Some of these carriers will be trapped in states in the forbidden energy gap and are then released at a later time, initiating a subsequent avalanche which is the so-called afterpulsing event [1, 2]. Afterpulsing is more obvious at lower temperatures because the carriers are trapped for longer before being released. If the trapped carrier lifetime is comparable to, or larger than, the repetition period the device is operating at, then the released carriers can trigger breakdown events during the subsequent detection periods resulting in a significant increase in the dark count rate when compared to lower repetition rates [3]. This afterpulsing phenomenon can severely restrict the maximum count rate of a SPAD, because if the traps are not depopulated quickly enough the device would need to be operated at a lower repetition rate to eliminate this effect. At higher temperatures where the effects of afterpulsing are less obvious as the trap lifetime is reduced, the DCR is generally greater since due to band-to-band thermal excitation of carriers initiating avalanche events. Hence, when choosing an operating temperature for SPADs a compromise must be reached between reducing the thermally induced DCR and increasing the afterpulsing effects, or vice versa. Another compromise must be made when choosing an excess bias to apply across devices, as the greater the charge that flows through the device, the greater the probability of carriers occupying traps within the device, those of which have the potential to contribute to afterpulsing [4, 5]. Because the charge through the device depends on the excess bias, a higher bias which can lead to increased detection efficiency and this must be offset by the increase in afterpulsing contributing to noise and increasing the NEP of the device as well as the limiting effect it has on the repetition frequency of device operation [6].

One can reduce the effects of afterpulsing by altering the quenching techniques and CMOS circuitry used [7-9] which serve to minimise the charge passing through the device per avalanche. However, it is important to understand the origin of the traps in a SPAD in order to better address the issue.

Although a lot of research has been performed into statistically modelling of afterpulsing based on de-trapping times, other factors such as thermal agitation, trap-assisted tunnelling and band to band tunnelling mechanisms all need to be considered when studying the effects of afterpulsing [10, 11]. Afterpulsing analysis has been performed on InGaAs/InP, Si and Ge SPADs, however the approaches vary and there is no universal agreement that fully explains the physical significance [11-13].

## 6.2 Activation Energy

The activation energy of an avalanche diode refers to the minimum thermal energy required to excite a carrier from a trap within the lattice and is therefore closely related to the DCR and afterpulsing characteristics of a device. The specific activation energy of the traps corresponds to a particular material and so by calculating the activation energy or energies one can locate the dominant trap states. To date, there have been several ways to calculate this value with the most conventional method being an Arrhenius plot [14-16]. The conventional method can be performed using the Arrhenius equation, Equation 6.1, and is found by plotting the natural logarithm of the dark current against 1/kT at a pre-determined over-bias and either extracting the gradient or gradients depending on whether there are multiple mechanisms dominating at different temperature ranges. Or measuring the time at which the afterpulsing probability falls to 10 % of the devices DCR which has been implemented with promising results [15, 17].

$$I_{dark}(Amperes) = Ae^{-\frac{E_a}{kT}} \tag{6.1}$$

Whereby $E_a$ is the activation energy of the trap, A is an arbitrary constant, k is the Boltzmann constant and T is the temperature. By multiplying the DCR by electron charge it would then also be possible to calculate the activation energy from a DCR Arrhenius plot. Another method for calculating activation energy incorporates afterpulsing rates and uses the time constant for calculations. An example of an afterpulsing decay on a InGaAs/InP avalanche diode is shown in Figure 6.1 (a) and an example of the activation energy Arrhenius plot derived from it is shown in Figure 6.1 (b) [18].

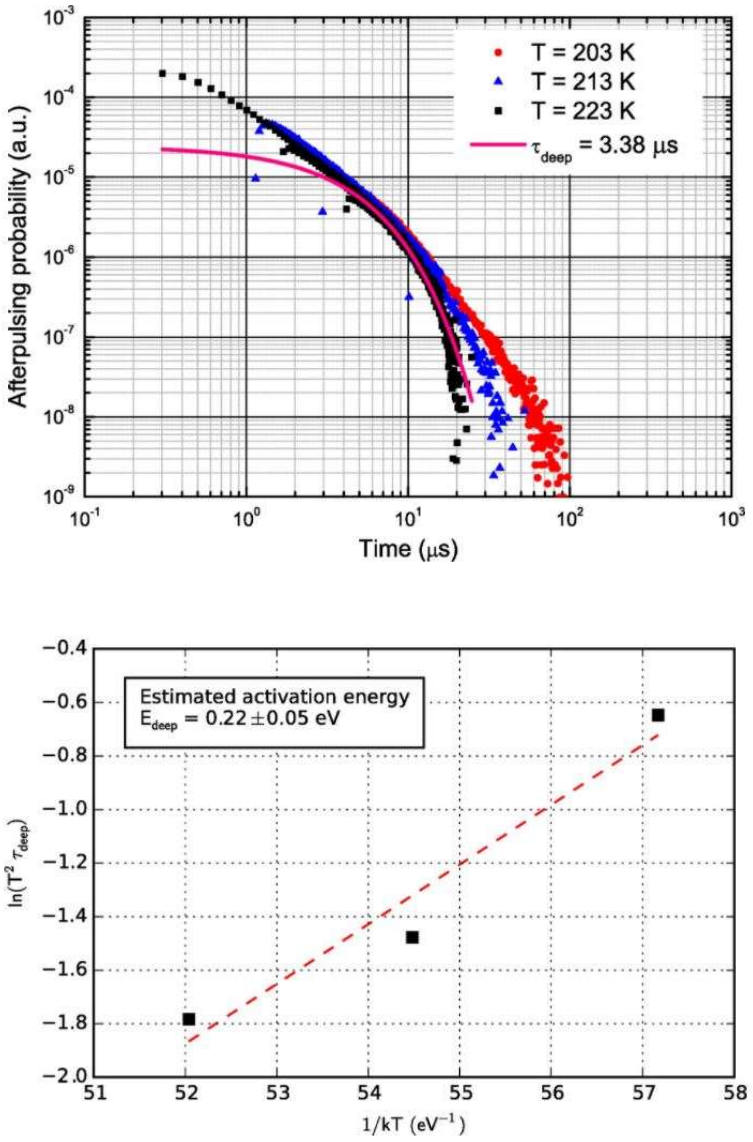


*Figure 6.1. (a) Afterpulsing results at 203, 213 and 223 K in a InGaAs/InP SPAD. (b) The Arrhenius plot of time constants used in estimation of activation energy from these afterpulsing decay [18].*

### 6.3 InGaAs/InP SPAD Afterpulsing

Ge has been a popular choice for linear mode APD detectors in the NIR/SWIR bands and has been comprehensively researched for decades [19, 20]. APD detectors have been biased above the breakdown voltage, called Geiger mode APDs, and used successfully as SPADs.

However, one major drawback of Ge SPADs was that they needed to be operated at cryogenically cooled temperatures to reduce the effect of thermally generated carriers, this meant the quantum efficiency would significantly drop for 1550 nm wavelength detection [21, 22]. Another material system with a similar range of wavelength detection is InGaAs/InP. Although InGaAs/InP APDs have been operated as photon counting devices since the 1980s [23], their separate absorption and multiplication design contains at least three different semiconductor materials, making them more difficult to fabricate than a homojunction APDs, such as Ge. However, the high noise levels observed in Ge APDs led to further interest in InGaAs/InP, which showed relatively improved dark count performance. Also, cryogenically cooled Ge SPADs showed lower detection efficiency at the strategically important 1550 nm wavelength than InGaAs/InP SPADs at the same wavelength. A study performed in 1998 compared InGaAs/InP with Ge APDs and showed that at equal quantum detection efficiencies, InGaAs/InP APDs had lower noise equivalent power and at a higher temperatures (test performed at 123 K) the dark-count probability was more than 1 order of magnitude higher for the Ge APD [12]. However, InGaAs/InP APDs suffer from afterpulsing effects which limits their operational characteristics at lower temperatures. When compared to a simple Ge homojunction APD, a InGaAs/InP detector is a more complex heterostructure, containing several heterointerfaces and a high density of traps which leads to high afterpulsing probabilities. Compared to a Si homojunction [6], InGaAs/InP SPADs have very high afterpulsing probabilities.

Many research groups have focused on measuring the afterpulsing using different methods, some suggest the detection efficiency can be used to characterise the devices and others use the DCR [3]. Jensen *et al* who studied a InGaAs/InP APD and found the activation energy to be 110 meV [24], whereas Liu *et al* found multiple traps at 340 and 370 meV [25]. And although different fabrication methods and devices may have different trap states, one of the largest issues with calculating the activation energy is proving its validity. An important discovery towards isolating the origin of the impurities within APD and SPADs was made in 2007 by Buller *et al* when they successfully calculated the activation energy of two devices, both designed and grown by themselves, one a InGaAs/InP SPAD and the other a InP only device, fabricated under identical conditions with only with the InGaAs absorption region removed [26]. The activation energies were calculated using the 10 % method mentioned in

Section 6.2. The InGaAs/InP SPAD had an activation energy of 275 meV, compared to the activation energy of a InP only device which had an activation energy of 247 meV. Buller *et al.* believed these results were sufficiently similar to suggest the dominant traps causing afterpulsing are likely to be located in the wide-gap InP multiplication layer [17], which is under a high electric field.

In 2012 Itzler *et al.* [13] investigated the analysis of afterpulsing in both InGaAs/InP and Si SPADs. Hoping to identify the physical origin of the traps by using different analysis approaches of the afterpulsing decays. Both power law and exponential decay fits were used. It was hypothesised that if a few dominant traps were present in the device, theoretically it should show an exponential decay, as seen in Equation 6.2 [13], with each time constant from each exponential term representing a different trap level, exponential decay behaviour was assumed to be an accurate model of afterpulsing for many years [11]. However, the data appeared to fit a power law decay more reliably, and this implied it might be more physically meaningful to develop a model which incorporates de-trapping from a broad spectrum of trap levels as is expected in InP materials [27]. The power law decay takes the form of the following Equation 6.2. Where Y(t) is the afterpulsing probability, t is the delay time and α is some integer as seen in the following equation:

$$Y(t)(a.u) = At^{(-\alpha)} \tag{6.2}$$

The theory behind this conclusion is analysed in more detail in section 6.7. At present InGaAs/InP SPAD modules are commercially available from companies such as ID Quantique and MPD that operate at Peltier-cooled temperature, up to around 230 K. Operating at this temperature significantly reduces the effects of afterpulsing which allows operation at frequencies up to 133 MHz [28, 29]. Keeping InGaAs/InP SPADs as a practical choice for single-photon detection in the SWIR region. However, there remains major operational issues with the use of InGaAs/InP SPADs, mostly resulting from the high afterpulsing probability.

### 6.4 Ge-on-Si Afterpulsing Experimental Set-up

To complete the characterisation of our Ge-on-Si SPADs an afterpulsing analysis was performed, this would allow us to compare the results with InGaAs/InP SPADs and also help understand the origin of the afterpulsing effects. A different experimental set-up was needed to perform afterpulsing measurements than the one used in the SPDE, DCR and jitter measurements described in the previous Chapter. The NKT Photonics SuperK Extreme Supercontinuum laser was replaced with a PDL800 Picoquant pulsed laser diode. A Stanford research system R400 two channel gated photon counter was introduced and a second pattern generator; a HP 8112A pulse pattern generator was used to form the afterpulsing experimental set-up as shown in Figure 6.2.

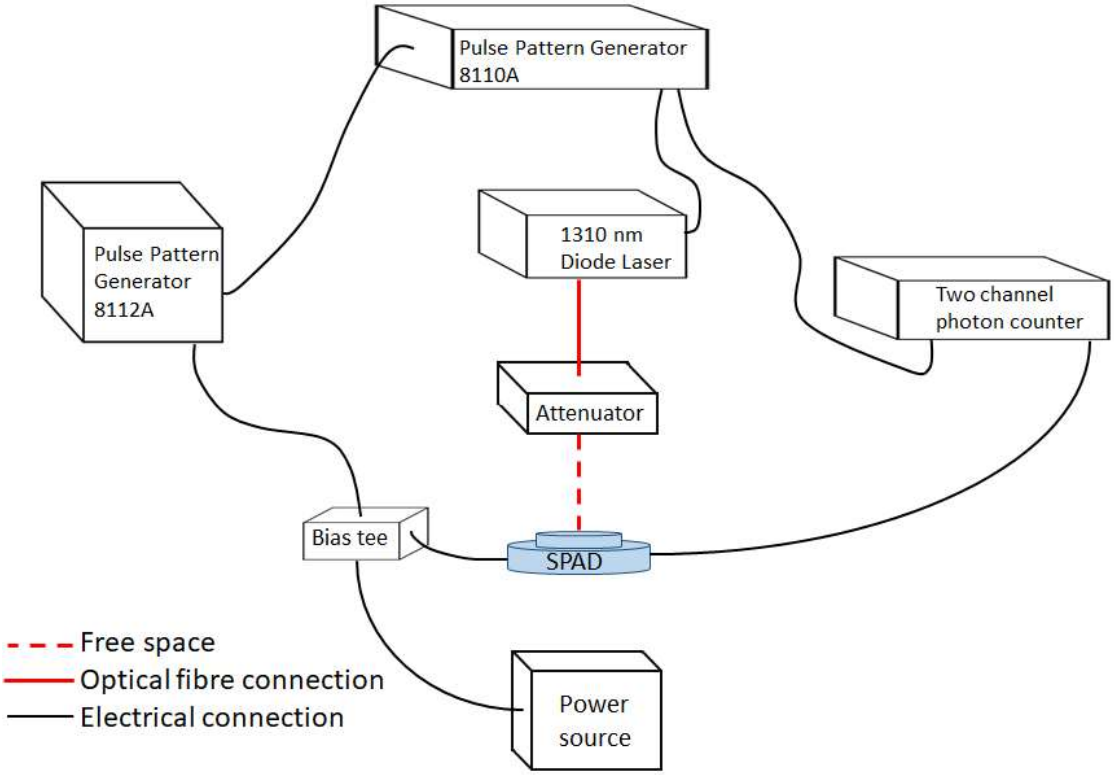


*Figure 6.2. Set-up used for afterpulsing measurements using a two-channel photon counter to monitor the dark count rate at a delay time after an intentional avalanche event, a DC power supply paired with an AC supply from the pulse pattern generator to quench the device and a 1310 nm wavelength diode laser providing illumination.*

The two-channel photon counter was set-up so that the initial avalanche caused a count in the first channel and the second channel collected the counts at varying time intervals after the initial avalanche. The delay on the second channel was controlled using a LabVIEW program. The laser was driven at a low frequency of 100 Hz in order that the afterpulsing had fully decayed before the next event was triggered. Data from 1000 laser pulses was collected before the delay in the second channel was increased, therefore each measurement took 10 s. The AC pulse from the Pulse Pattern Generator 8112A lasted 50 ns with a trailing and leading edge of 10 ns. The second channel started at a delay of approximately 0.2 ns after the first channel and the final reading was taken at a delay of 10 µs. Intervals between time delays were not constant but chosen to allow the most relevant information to be collected. Figure 6.3 shows how the device is gated with the first pulse timed to intentionally cause an avalanche and the second to monitor subsequent avalanches. The same set of Ge-on-Si SPADs with a 1 µm thick Ge absorber mentioned in Chapter 5 were used and results for both the 26 µm and a 50 µm diameter devices were obtained. Again, readings at different biases and temperatures were performed.

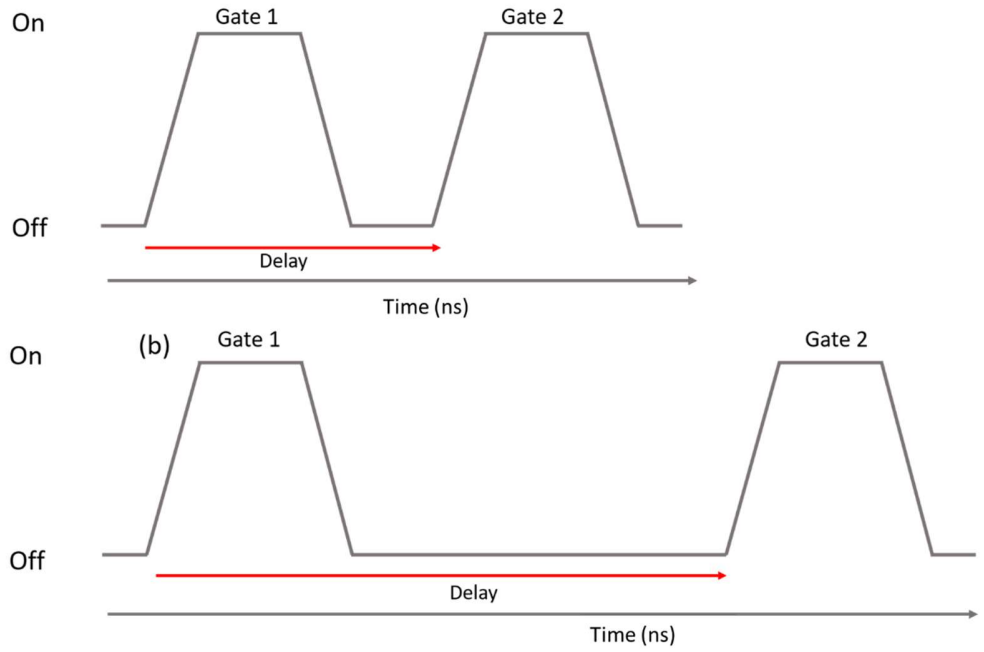


*Figure 6.3. Timing diagram showing the electrical gating of the SPAD where channel 1 is used to intentionally induce an avalanche in the SPAD, and the second gate is used to monitor subsequent events, delayed after the first avalanche.*

The results were plotted on exponential graphs at 78, 100, 125, 150 and 175 K. To avoid damaging the device higher temperatures were avoided, and maximum excess biases were adjusted accordingly this was also dependent on the size of the device as larger devices had larger DCR. Examples of the afterpulsing results with a 50 ns gate width at different temperatures, over a range of biases for both the 26 µm and the 50 µm diameter devices are displayed in Figure 6.4 and Figure 6.5 respectively. The count rate drops off exponentially with respect to time at a range of excess biases from 0.5 - 5.5 %.

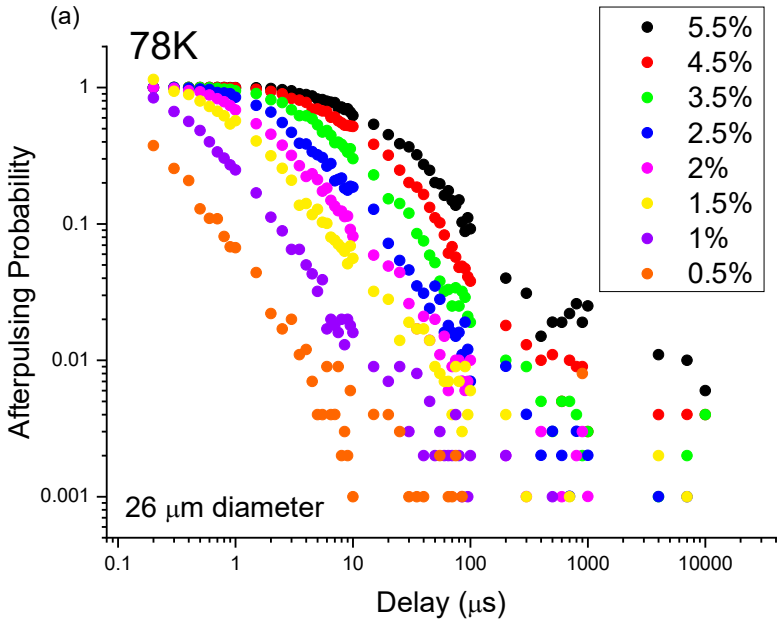

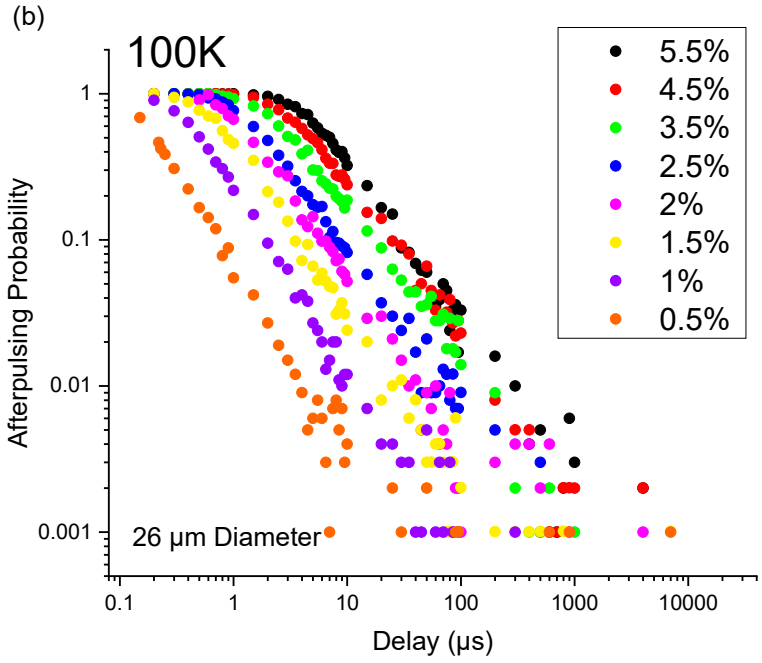
(b)
100K
5.5%
4.5%
3.5%
2.5%
2%
1.5%
1%
0.5%
Afterpulsing Probability
1
0.1
0.01
0.001
26 µm Diameter
0.1
1
10
100
1000
10000
Delay (µs)

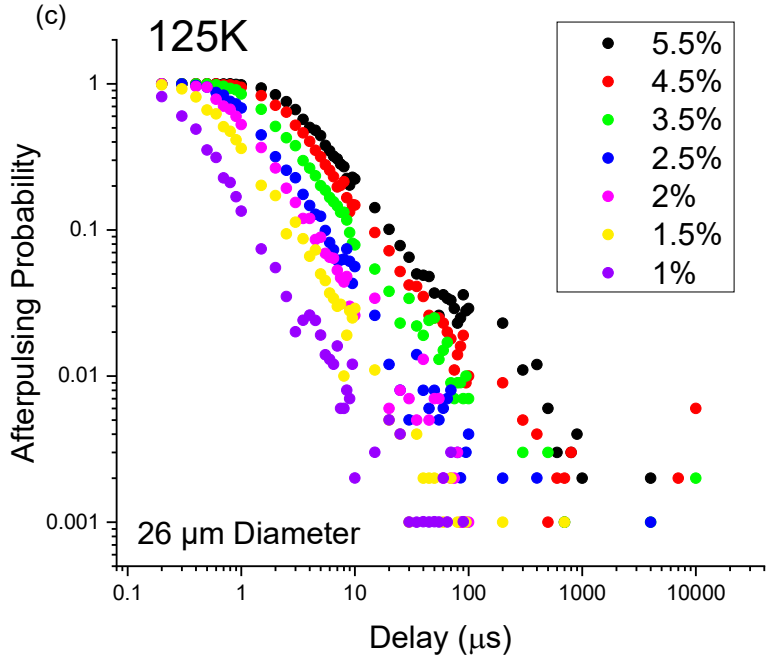
(c)
125K
5.5%
4.5%
3.5%
2.5%
2%
1.5%
1%
Afterpulsing Probability
1
0.1
0.01
0.001
26 µm Diameter
0.1
1
10
100
1000
10000
Delay (µs)

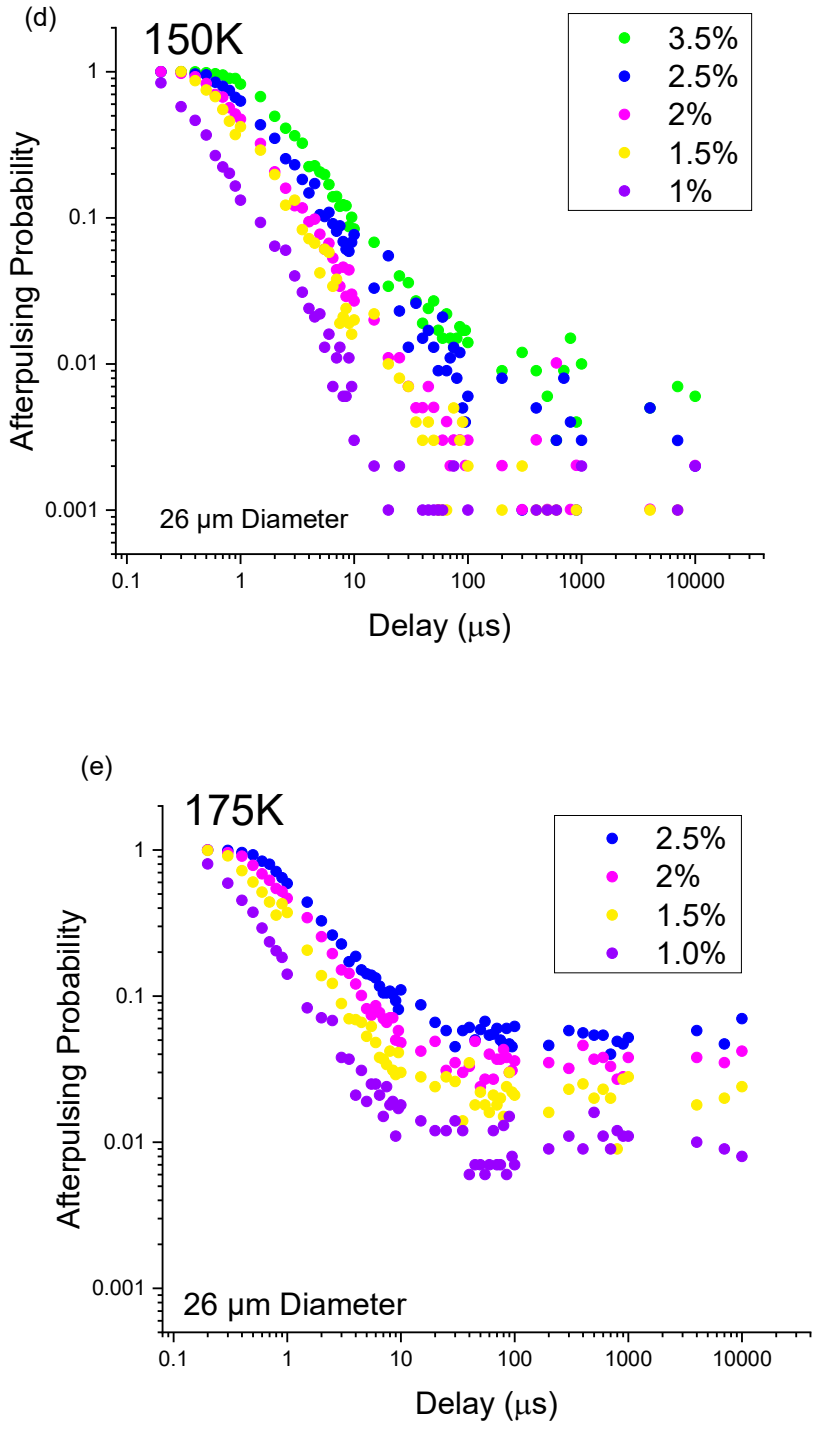


*Figure 6.4. Absolute afterpulsing probability with respect to delay at 78 K, 100 K, 125 K, 150 K and 175 K at different excess biases for a 26 µm diameter Ge-on-Si SPAD.*

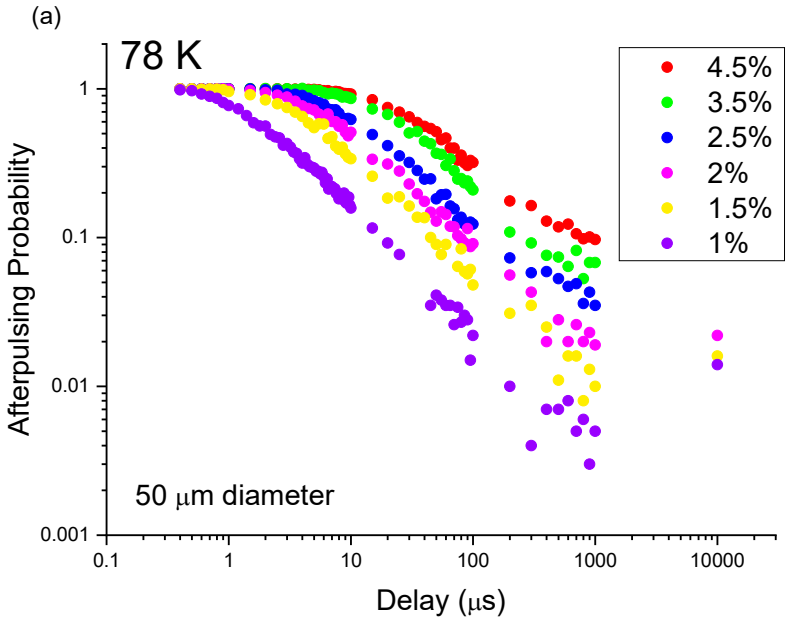
(a)
78 K
4.5%
3.5%
2.5%
2%
1.5%
1%
Afterpulsing Probability
1
0.1
0.01
0.001
50 μm diameter
0.1
1
10
100
1000
10000
Delay (μs)

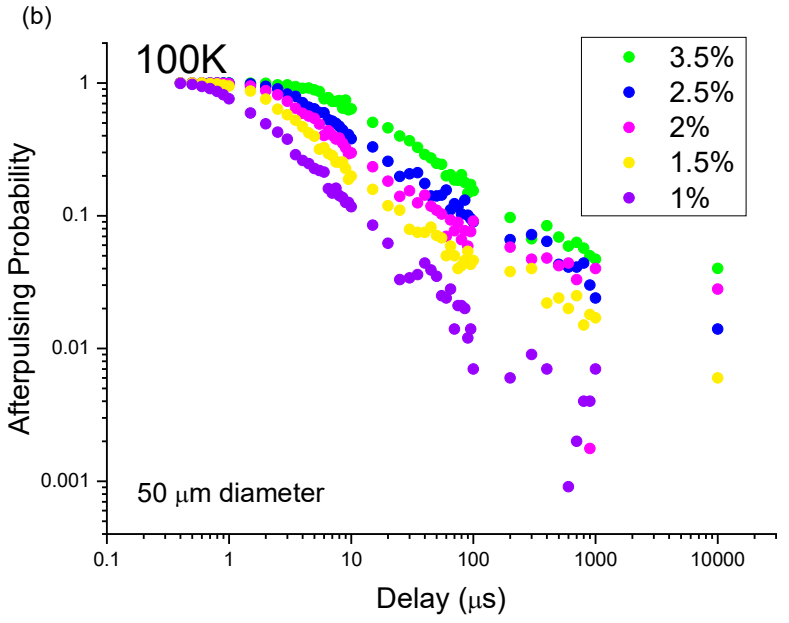
(b)
100K
3.5%
2.5%
2%
1.5%
1%
Afterpulsing Probability
1
0.1
0.01
0.001
50 μm diameter
0.1
1
10
100
1000
10000
Delay (μs)

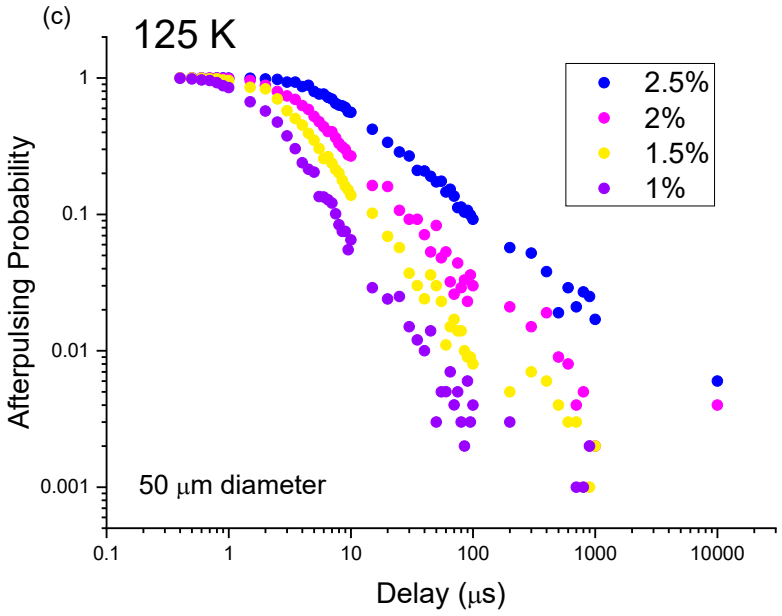


*Figure 6.5. Absolute afterpulsing probability with respect to delay at 78 K, 100 K and 125 K at different excess biases for a 50 μm diameter Ge-on-Si SPAD.*

Figure 6.6 and 6.7 shows the afterpulsing probability as a function of delay for a range of temperatures and excess bias. This shows a clearer picture of the effect of temperature on the devices afterpulsing characteristics at the same excess bias.

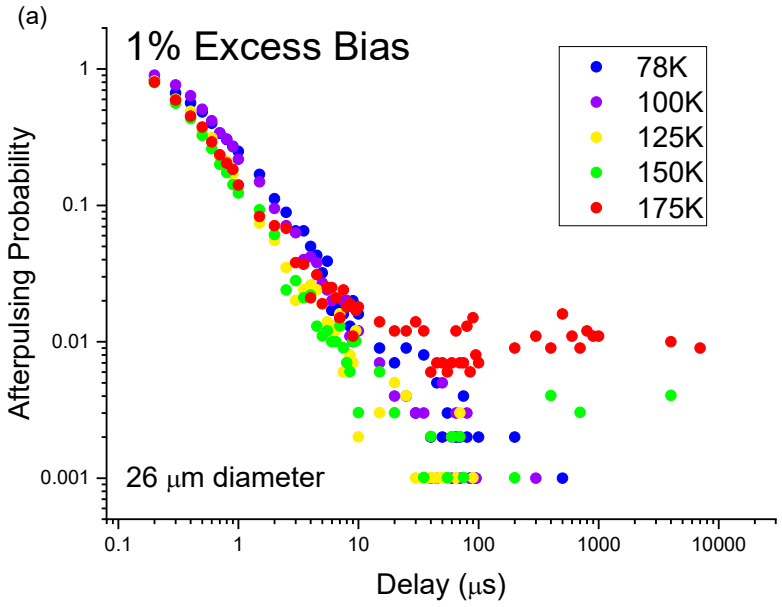
(a)
1% Excess Bias
78K
100K
125K
150K
175K
Afterpulsing Probability
1
0.1
0.01
0.001
26 μm diameter
0.1
1
10
100
1000
10000
Delay (μs)

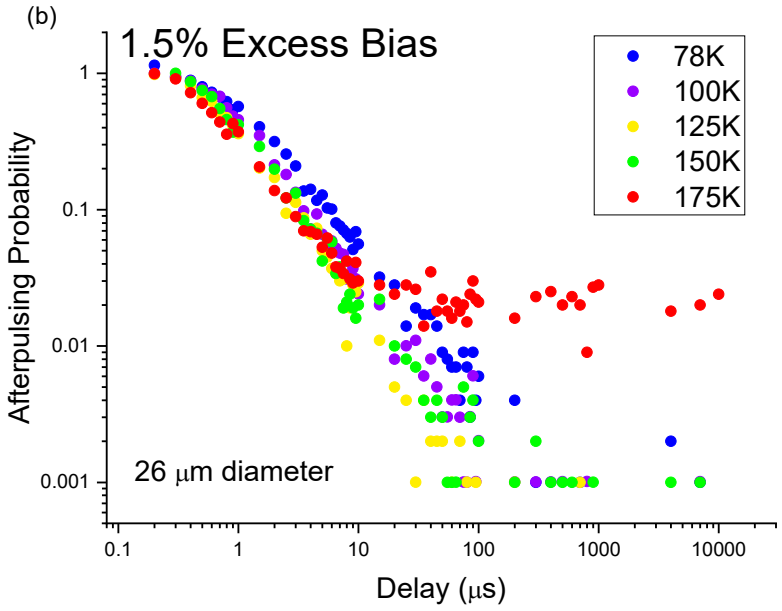
(b)
1.5% Excess Bias
78K
100K
125K
150K
175K
Afterpulsing Probability
1
0.1
0.01
0.001
26 μm diameter
0.1
1
10
100
1000
10000
Delay (μs)

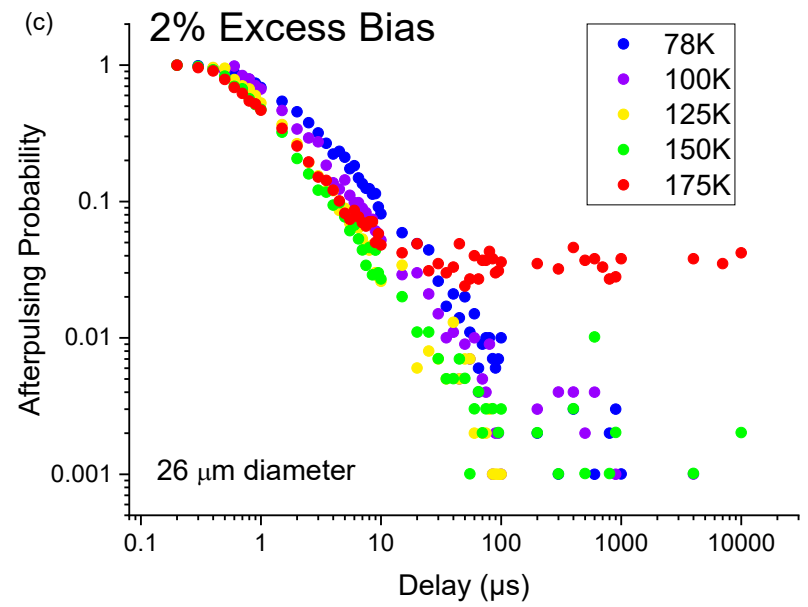


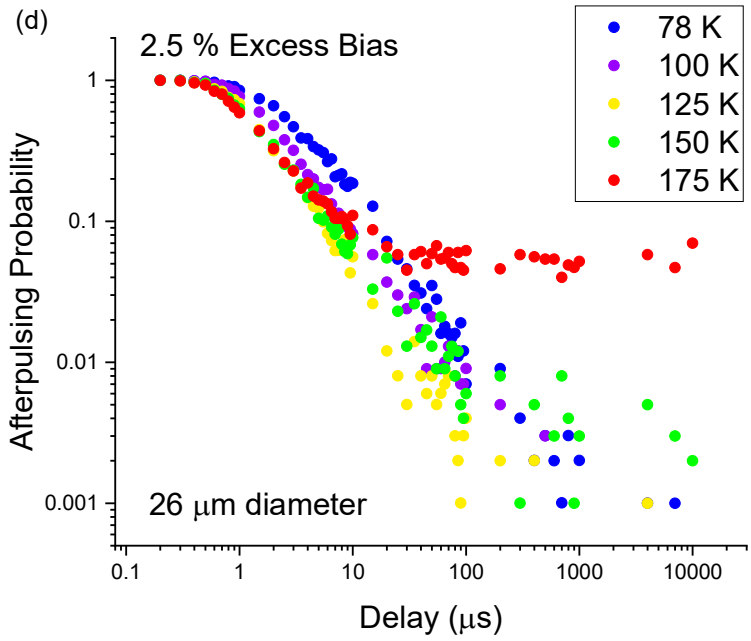


*Figure 6.6. Absolute afterpulsing probability with respect to delay at 1 %, 1.5 %, 2 % and 2.5 % excess bias at different temperatures for SPAD 4.8, 26 μm Ge-on-Si SPAD.*

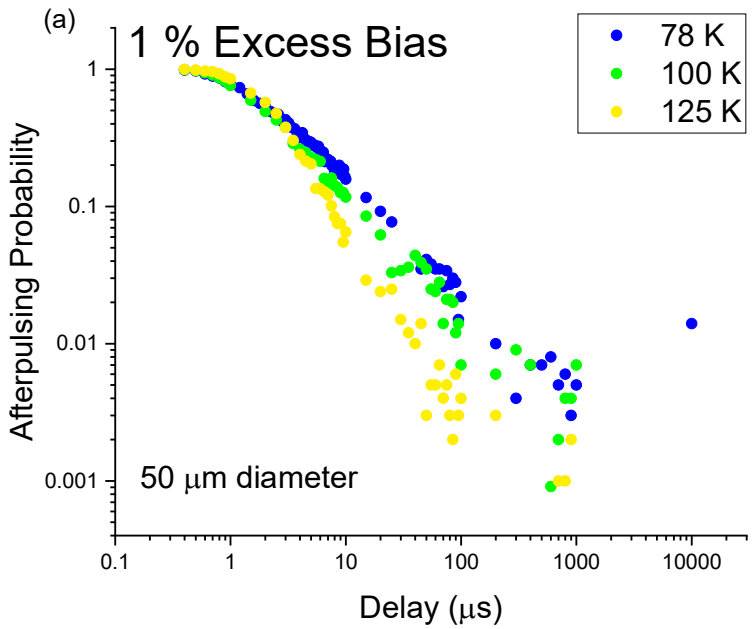
(a)
1 % Excess Bias
78 K
100 K
125 K
Afterpulsing Probability
1
0.1
0.01
0.001
50 μm diameter
0.1
1
10
100
1000
10000
Delay (μs)

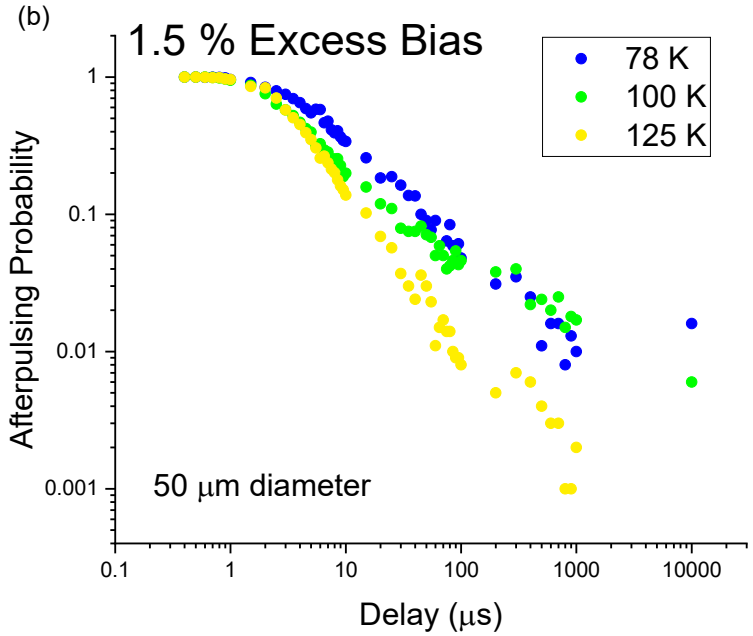
(b)
1.5 % Excess Bias
78 K
100 K
125 K
Afterpulsing Probability
1
0.1
0.01
0.001
50 μm diameter
0.1
1
10
100
1000
10000
Delay (μs)

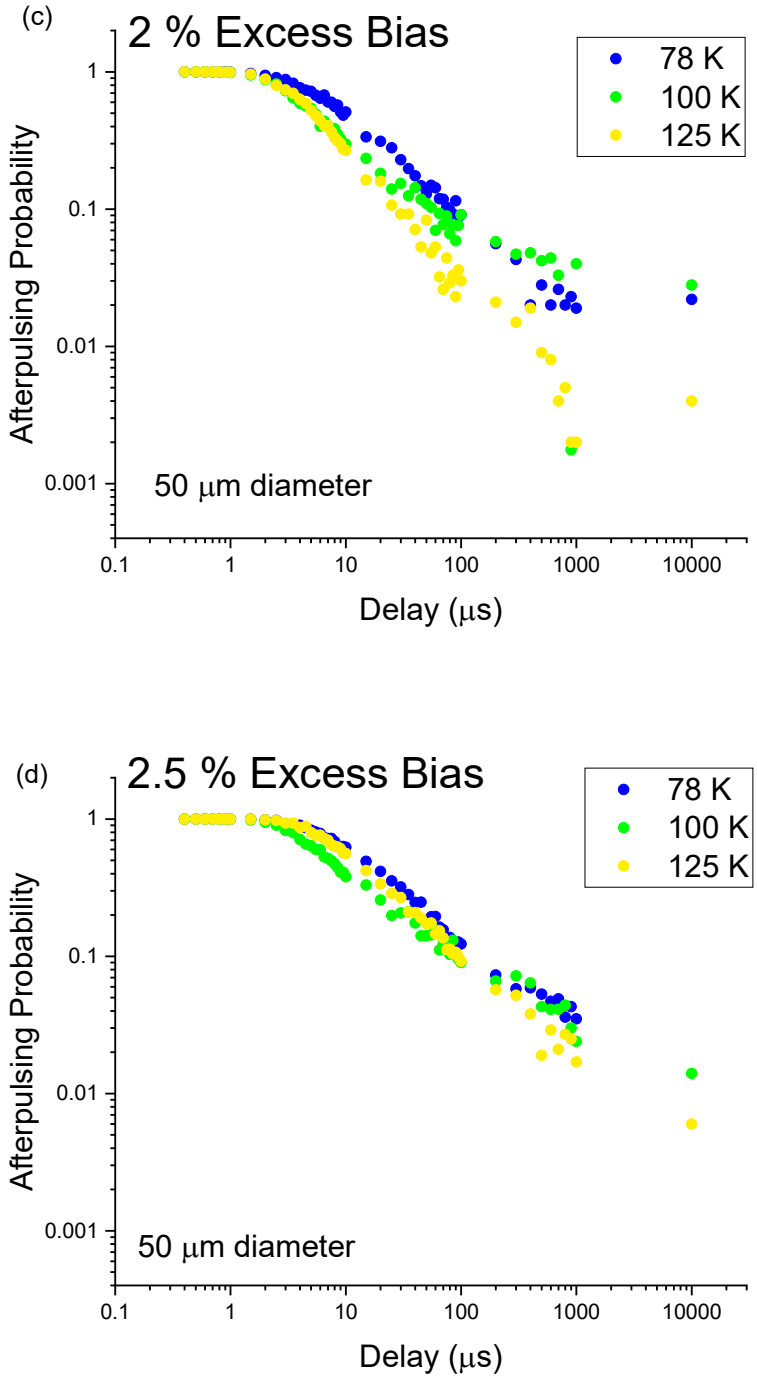


*Figure 6.7. Absolute afterpulsing probability with respect to delay at 1 %, 1.5 %, 2 % and 2.5 % excess bias at different temperatures for SPAD 4.8, 50 μm diameter Ge-on-Si SPAD.*

From Figures 6.6 and 6.7 we can see that the afterpulsing decay rate is relatively similar initially for all temperatures, as they all have similar shapes. With the noise floor only becoming a significant factor at 175 K. To characterise this decay rate, we need to describe the decay in terms of a time constant. The method we chose to obtain the time constant will be referred to as the '10 % method' in which the decay is analysed in terms of when the afterpulsing probability reaches 10 % of its original value is used [30]. The 10 % time constant is used to calculate the activation energy of traps by plotting it in an Arrhenius graph.

The time constants were calculated by fitting a single exponential decay fit to the afterpulsing results using OriginPro software, which uses a Levenberg Marquardt iteration algorithm and finding the 10 % value. The time constant was noted at different temperatures and this time constant was then plotted against 1/kT for all excess biases. The slope from this graph should then be used to calculate the activation energy which will enable us to understand the traps in planar Ge-on-Si SPADs. Figure 6.8 shows the time constant Arrhenius plot at different excess biases and it is clear there are two very different gradients present for lower and higher temperatures as well as some higher excess biases missing graph points. High temperature and high bias measurements were avoided in order to risk damage to the SPAD by passing too high a current through it which could lead to localised heating.

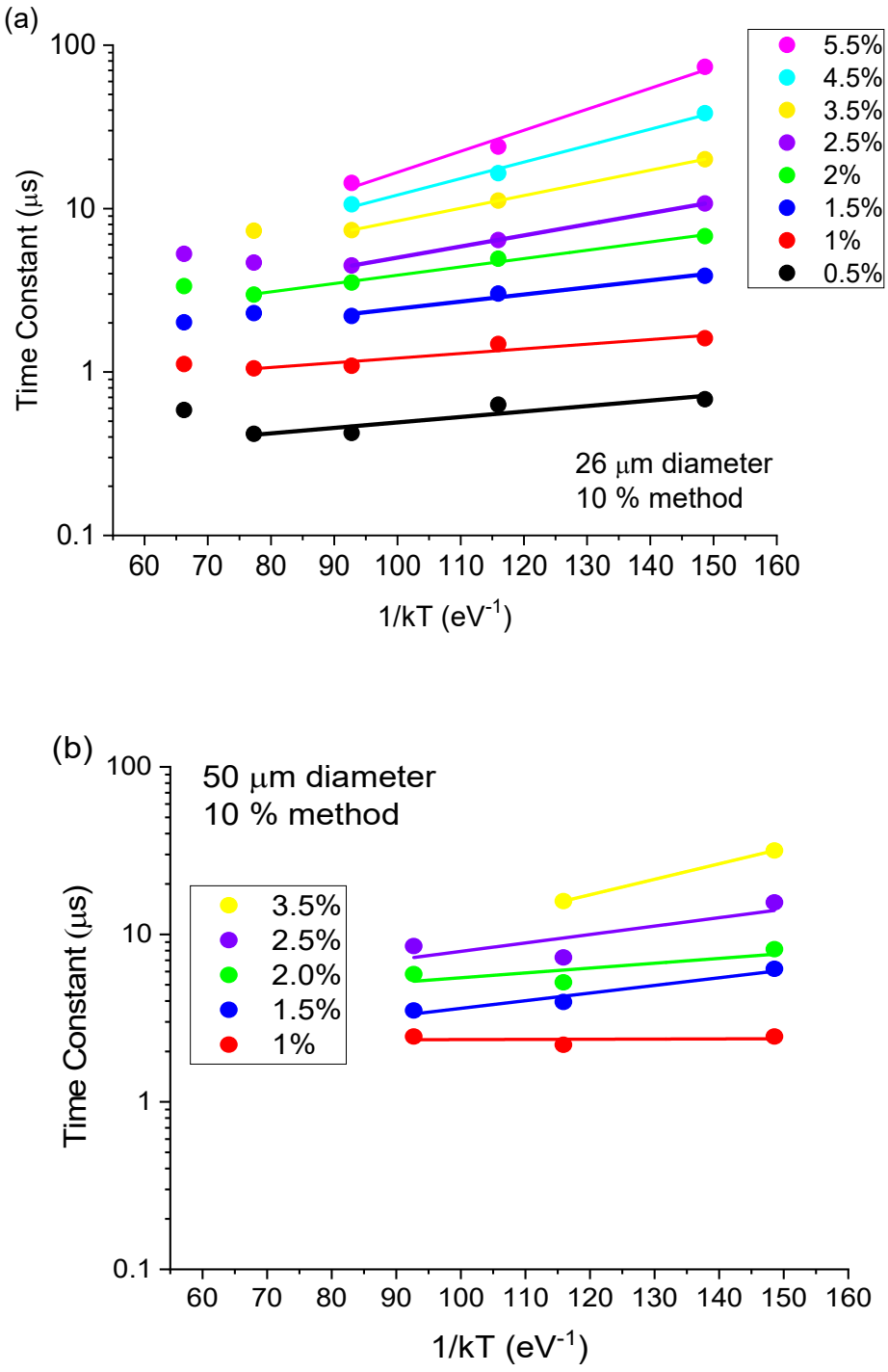


*Figure 6.8. Arrhenius plot of afterpulsing time constant at different excess biases from 0.5% up to 5.5 % for the (a) 26 μm and between 1 % and 3.5 % for the (b) 50 μm diameter device. The linear fit used to determine the gradient of the results shown as a solid line.*

In Figure 6.8 a linear fit has been used to determine the gradient of the Arrhenius plots at different excess biases. As demonstrated, some higher temperature results have been omitted from the fit as we believed they were not representative of the afterpulsing due to the excess thermally generated dark events at higher temperatures. The error associated with the time constants is too small to be visible on the figures but an error analysis has been performed by fitting the lowest temperature two and three results and calculating the difference in activation energy. At the lower voltages in particular the error is much less than 1 %. The error at higher voltages increases to ± 5 %, however it should be noted that the thermally generated noise also substantially increases at these overbias levels.

Using the data show in Figure.6.8, further analysis of the gradients gave the following values for activation energies shown in Figure 6.9.

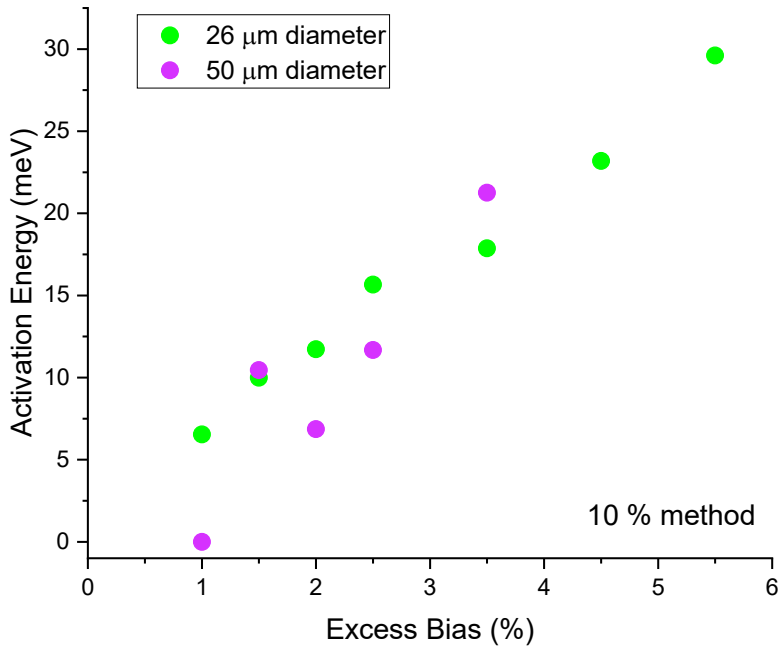


*Figure 6.9. Activation energy at different excess biases from 1 – 5.5 %, for a Ge-on-Si SPAD of active area 26 µm (green) 50 µm (purple) using an Arrhenius plot of the time constants to calculate values.*

The activation energies calculated from the DCR of the 26 µm diameter device, reported in Chapter 5 indicate activation energies of between 34-42 meV depending on excess bias,

which is slightly higher than shown in Figure 6.9. From Figure 6.9 it appears that the activation energy is highly dependent on the overbias. The DCR measurements in Chapter 5 seemed to suggest that the activation energy was much less overbias dependent and even showed a decrease at the highest overbias levels. As the DCR measurements were able to be performed at higher biases this suggests that we were not able to illustrate the flattening of the activation energy with overbias, since the dynamic range in overbias was not available in these high DCR devices. We believe using the afterpulsing decay method illustrated in Figure 6.9 is more reliable, as it is less likely to have other mechanisms contributing significantly to the activation energy. There appears to be a linear relationship between the activation energy and the excess bias which may help narrow down the potential defect material causing the afterpulsing. As previous results were calculated only using selected temperature data further testing was needed to investigate the effect of changing the ratio of DC to AC current applied to the devices as this could have distorted the results at certain temperatures and biases.

### 6.5 Commercial Si SPAD Afterpulsing Analysis

To isolate the origin of the traps contributing to the dominant cause of afterpulsing in Ge-on-Si SPADs, a commercial Si SPAD was examined. By characterising the afterpulsing of an all-silicon SPAD we could then calculate and compare the activation energy of it, to that of our Ge-on-Si SPAD and see any similarities. Two similar activation energies would imply the same source of afterpulsing and therefore suggest that the Si layers in the Ge-on-Si SPAD are the location of the traps.

We used a Silicon Geiger Mode Avalanche Photodetector from Laser Components with an active area of 500 μm and a maximum spectral responsivity at 650 nm [31]. DCR and SPDE measurements were first performed to check the device was working at the low temperature. However, the DCR was so low at the temperatures we looked at (sub 120 K) that we were not able to get the minimum of one count per histogram bin required to reliably calculate a DCR in a reasonable amount of time, this was expected as the DCR quoted by Laser components was 10,000 counts per second (cps) at 295 K. The results for the SPDE with

illumination a wavelength of 600 nm are shown in figure 6.10. As expected, increasing the excess bias increased the SPDE due to the increasing electric field within the device, the increasing SPDE starts to flatten out at maximum efficiency where the trigger probability approaches a maximum. The temperature also has a much more noticeable effect on SPDE than with our Ge-on-Si devices where the device appeared to be far less temperature sensitive.

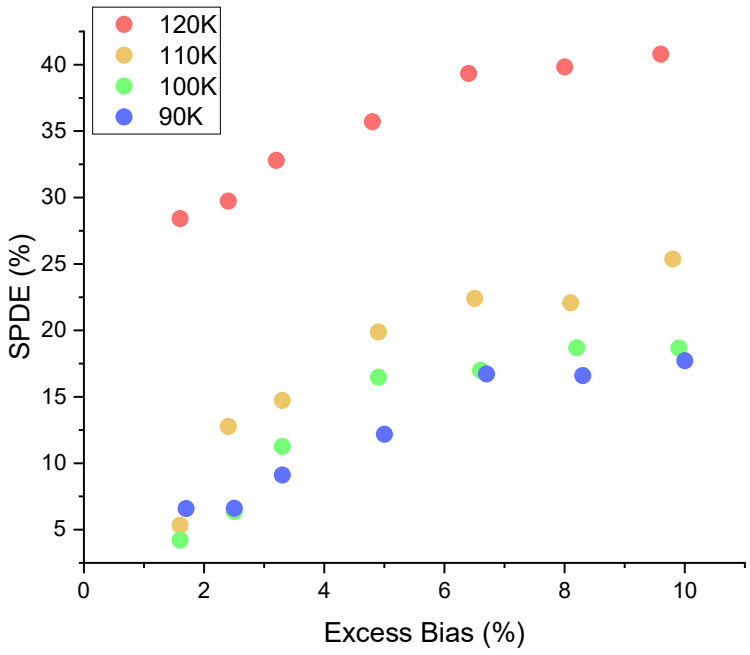


*Figure 6.10. The SPDE for a commercial Si SPAD at 120, 110,100 and 90 K at excess biases between 1.6 % and 10 % at a wavelength of 600 nm.*

Using the same method as outlined previously for the afterpulsing, we gathered results for temperatures between 78 K and 120 K. At excess biases from 1.6 % to 10 %. As shown in figure 6.11, this range of temperatures and excess biases allowed us to draw comparisons with the Ge-on-Si SPAD mentioned in Section 6.4.

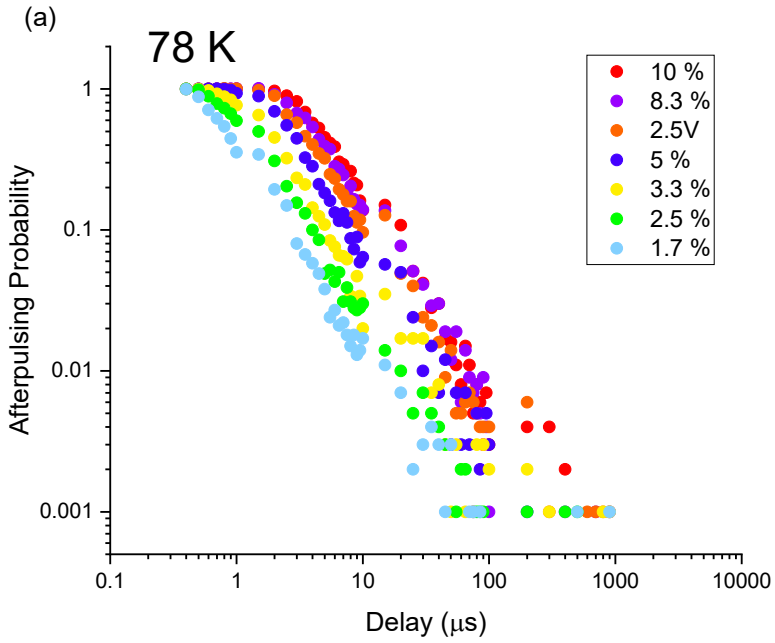
(a)
78 K
10 %
8.3 %
2.5V
5 %
3.3 %
2.5 %
1.7 %
Afterpulsing Probability
1
0.1
0.01
0.001
0.1
1
10
100
1000
10000
Delay (μs)

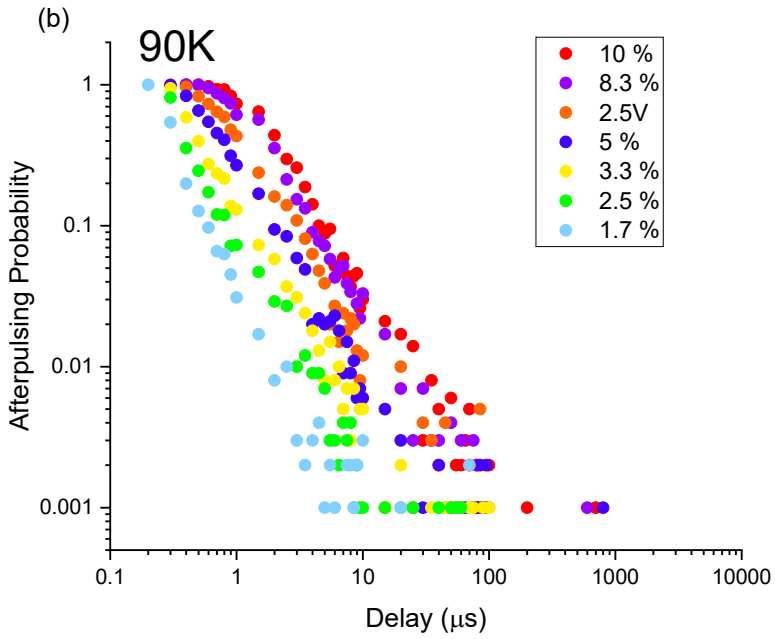
(b)
90K
10 %
8.3 %
2.5V
5 %
3.3 %
2.5 %
1.7 %
Afterpulsing Probability
1
0.1
0.01
0.001
0.1
1
10
100
1000
10000
Delay (μs)

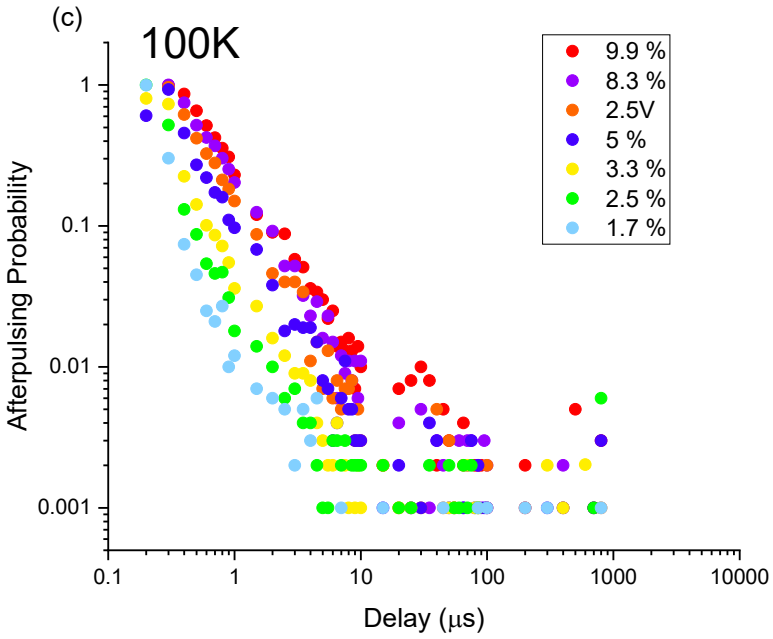
(c)
100K
9.9 %
8.3 %
2.5V
5 %
3.3 %
2.5 %
1.7 %
Afterpulsing Probability
1
0.1
0.01
0.001
0.1
1
10
100
1000
10000
Delay (μs)

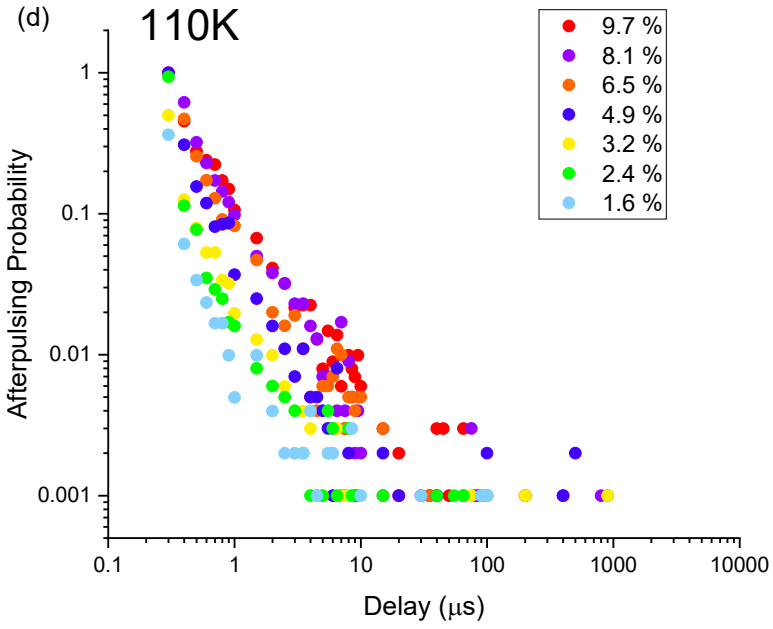
(d)
110K
9.7 %
8.1 %
6.5 %
4.9 %
3.2 %
2.4 %
1.6 %
Afterpulsing Probability
1
0.1
0.01
0.001
0.1
1
10
100
1000
10000
Delay (μs)

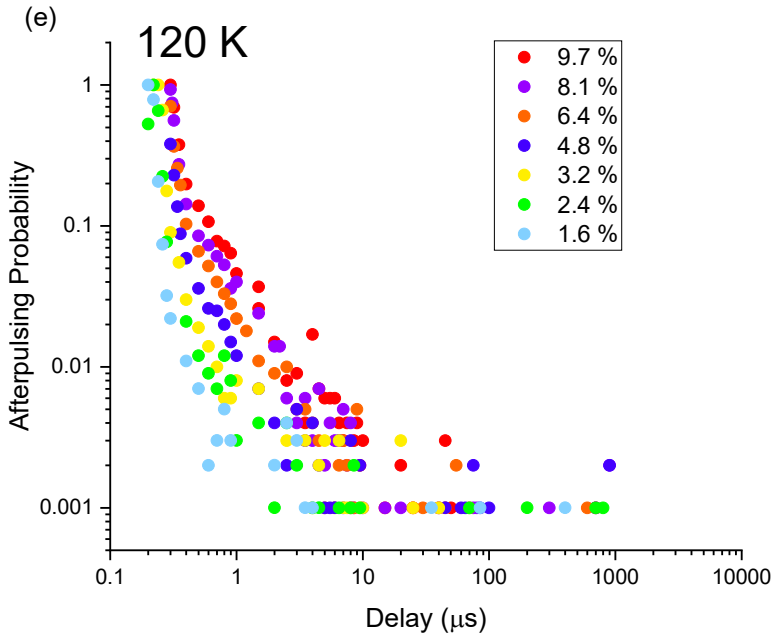


*Figure 6.11 The afterpulsing probability as a function of delay time for a commercial Si SPAD at 120, 110, 100, 90 and 78 K at excess biases between 1.6 % and 10 % of the avalanche breakdown voltage.*

Analysis was performed using several different methods on these results whilst we investigated the theory of the physical mechanisms giving rise to the afterpulsing behaviour. More detail on this can be found in the following section 6.6 Fitting physical significance to decay behaviour. Initially we used an exponential fit with two terms shown in Equation 6.3:

$$Y(t)(a.u) = A_1 e^{\frac{-t}{\tau_1}} + A_2 e^{\frac{-t}{\tau_2}} + y_0 \tag{6.3}$$

Where Y(t) is the afterpulsing probability, A and $y_0$ are constants and t is the time constant. We used two terms instead of one because we believed there to be two distinct gradients in the logarithmic-linear plot, and there could be two distinct and separate mechanisms leading to two separate activation energies. This was most clear at higher temperatures and biases as seen in the examples as shown in Figure 6.12, where the gradient at delays smaller than 1000 ns is much steeper than over longer delays.

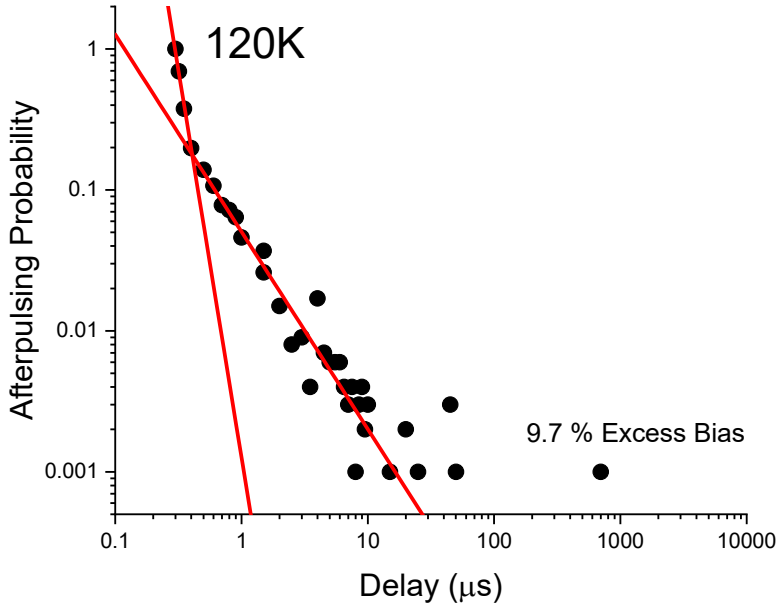


*Figure 6.12. Example of afterpulsing probabilities for a Si-SPAD at high biases at 120 K showing two different gradients.*

Initially we used OriginPro software to fit the exponential equation but found the background term was misleading and unreliable depending on the background noise and whether it was removed prior to fitting. In the case of Figure 6.13 the blue line shows the exponential fit using all of the data and the red line shows the exponential fit when data underneath the noise level of the blue fit is removed giving two very different values for the second time constant terms.

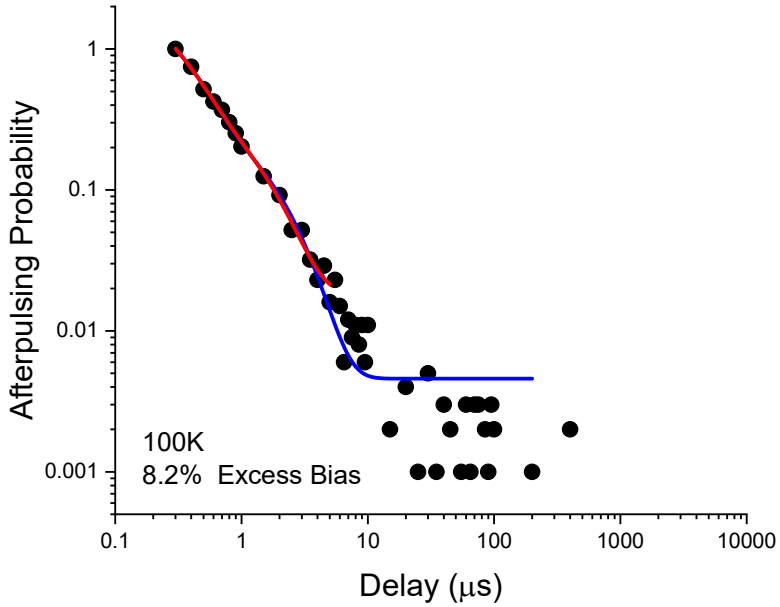


*Figure 6.13. Example of two exponential fits on afterpulsing data showing the effect of including all data point prior to fitting (blue) and removing the data caused by noise before fitting (red).*

To avoid this unreliability, the exponential curves were manually fitted using trial and error. This resulted in T1 being similar to the OriginPro fitting function, but when T2 was manually fitted it formed a much more reliable result as when plotting the Arrhenius plot a larger proportion of time constants appeared linearly related. Figure 6.14 is an example of what a manually fitted exponential looks like without a background term when compared to one computationally fitted with a background term. Note how the computational fit (red) agrees with my manual fitting (blue) for the first part of the curve yet is a poor fit for the data from the second half of the graph and gives only two identical time constants.

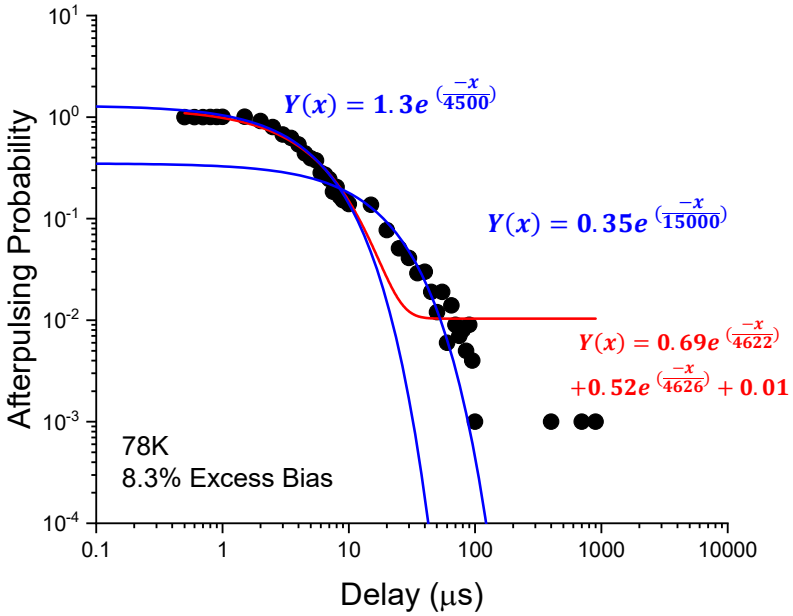


*Figure 6.14. Examples on an afterpulsing probability graph of a computational double exponential fit including a background term (red) compared to manually fitting two exponentials without a background term (blue).*

Figure 6.15 shows a comparison of the exponential fit Arrhenius plot including a background term and the Arrhenius plot resulting from a manual fit of two exponentials to the data using trial and error to find an approximate time constant value.

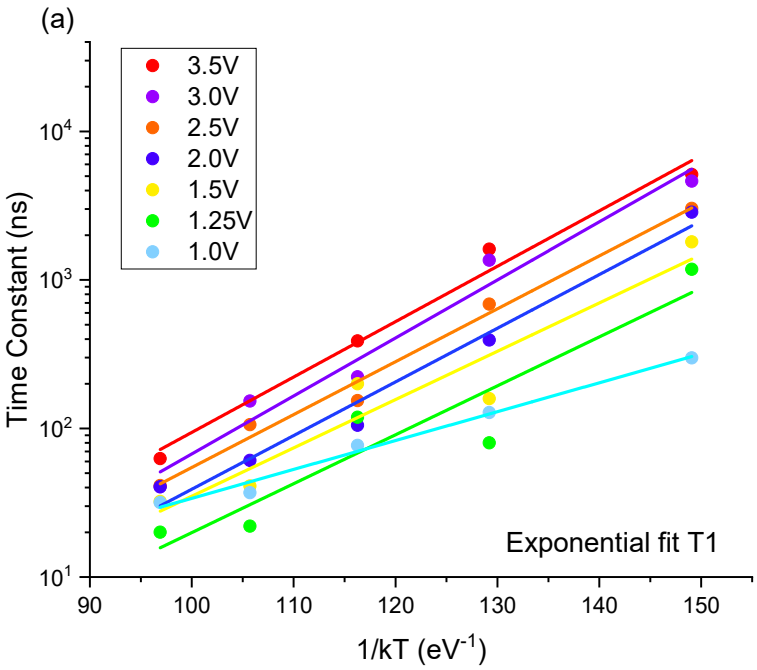
(a)
3.5V
3.0V
2.5V
2.0V
1.5V
1.25V
1.0V
Time Constant (ns)
$10^4$
$10^3$
$10^2$
$10^1$
90
100
110
120
130
140
150
1/kT ($eV^{-1}$)
Exponential fit T1

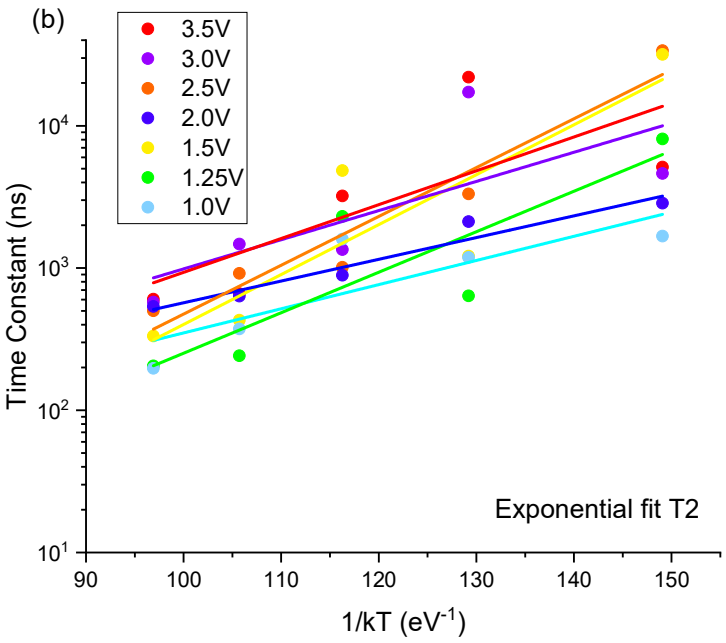
(b)
3.5V
3.0V
2.5V
2.0V
1.5V
1.25V
1.0V
Time Constant (ns)
$10^4$
$10^3$
$10^2$
$10^1$
90
100
110
120
130
140
150
1/kT ($eV^{-1}$)
Exponential fit T2

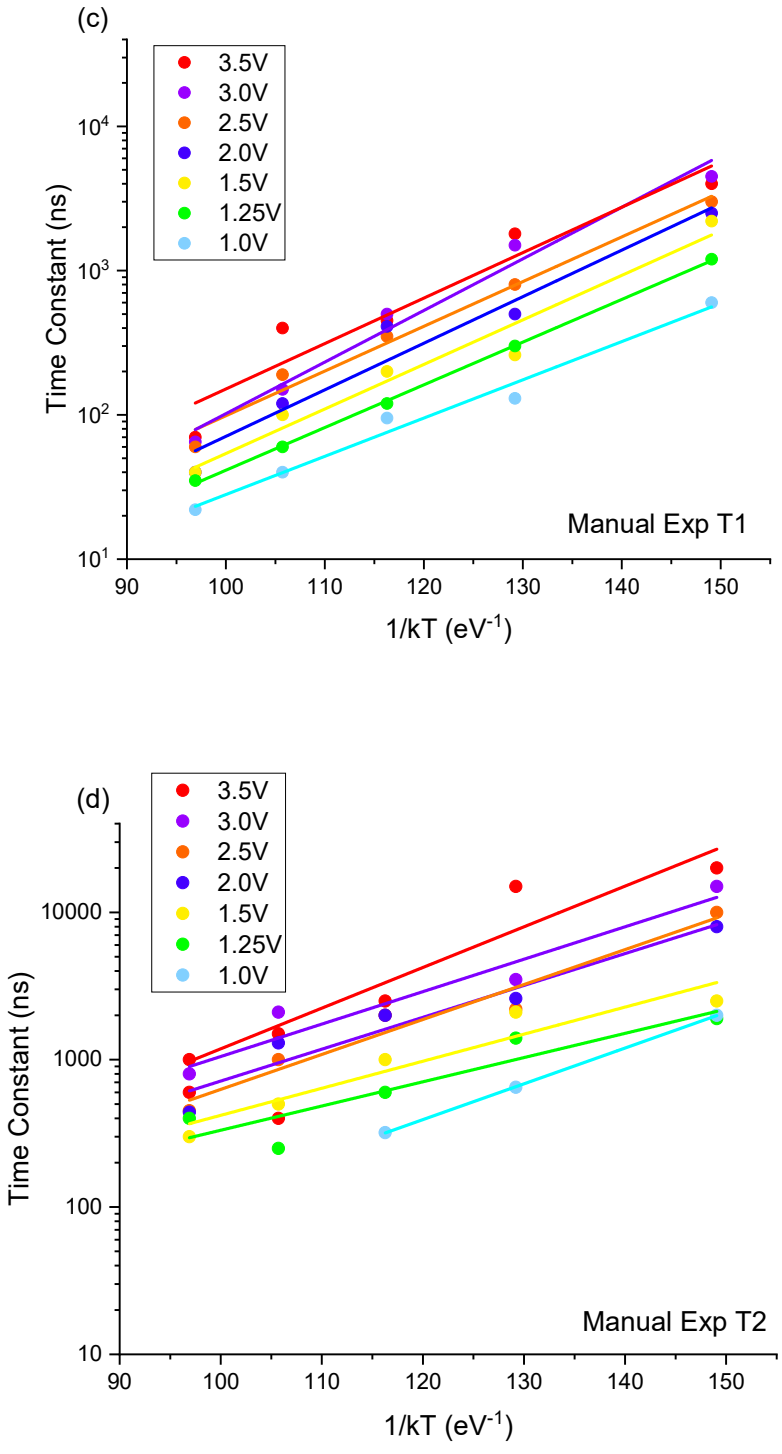


*Figure 6.15. Comparison of time constants calculated from fitting a computational exponential fit produced by origin including a background term and the Arrhenius plot resulting from when two exponentials are manually fitted to the raw afterpulsing results.*

For comparison, the same data was used to determine time constants using the 10 % method used to find the Ge-on-Si activation energies, this method uses the time taken for the afterpulsing to fall to 10 % of the original value. This produced the following Arrhenius plot, Figure 6.16. When fitting a gradient to the results a better fit was achieved than previously with the results shown in Figure 6.15.

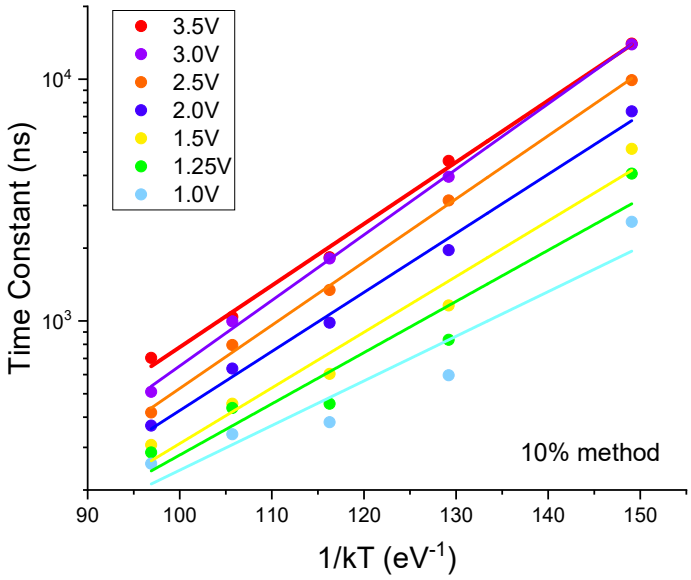


*Figure 6.16. Arrhenius plot of Si SPAD time constants at seven different overbias conditions. The time constants were estimated using the 10 % method.*

The issue with using the 10 % method is that it does not account for the existence of two dominant traps at higher temperatures. To compare the 10 % method to the computational fitted exponential and manually fitted exponential the activation energies are plotted together, Figure 6.17.

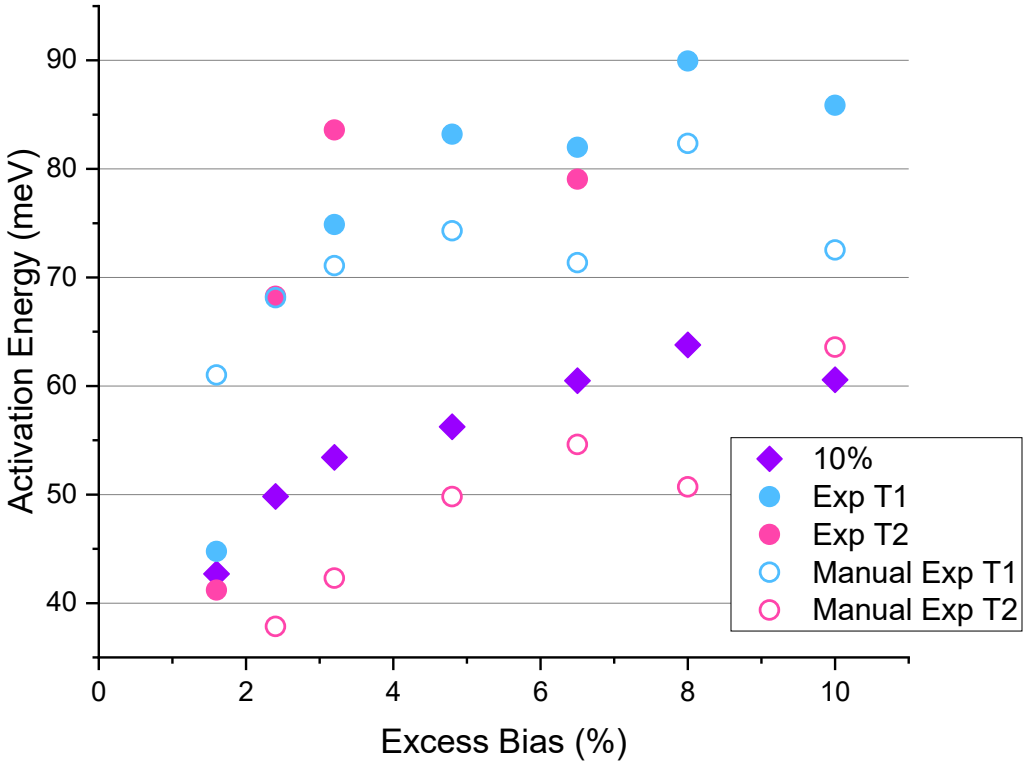


*Figure 6.17. The activation energy of a commercial Si SPAD calculated using three different analysis methods; 10 % method (purple), computationally fitted exponential (Exp T1/T2) and manually fitted exponentials (Manual Exp T1/T2).*

To compare, the Si and the 26 and 50 µm diameter Si-on-Ge activation energies calculated using the 10 % method have been plotted together. Results for activation energy using the 100 µm device reported by Vines *et al.* [32], were calculated using the same 10 % method with his raw data. This reduced any faults caused by random and human error. All these results including the device reported by Vines *et al.* [31], are shown in Figure 6.18.

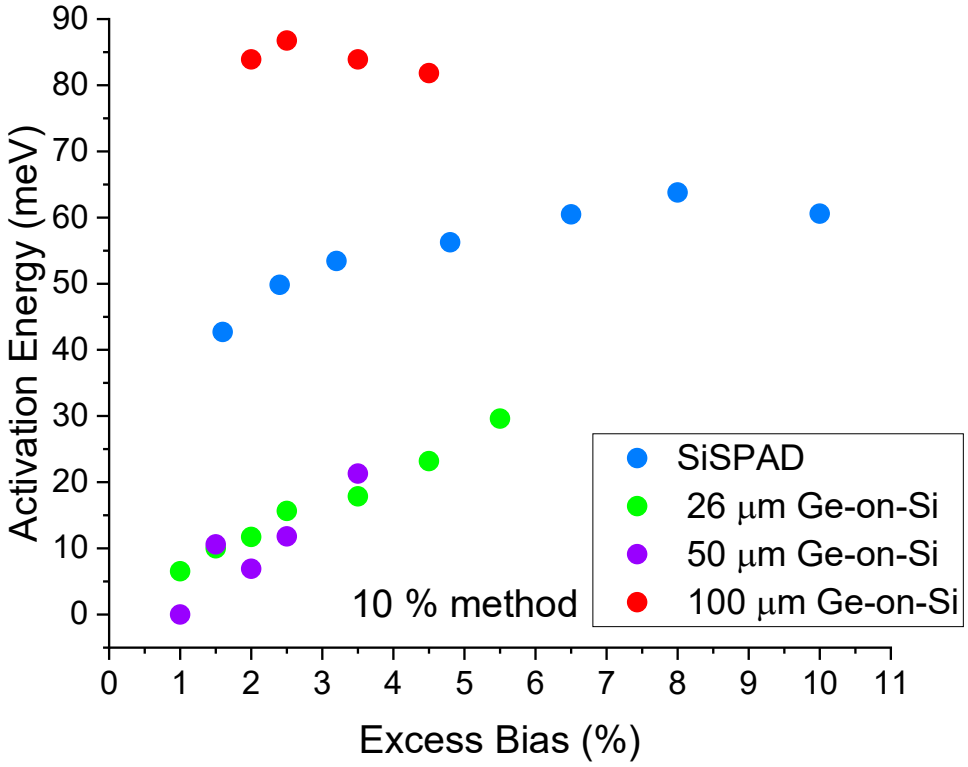


*Figure 6.18. Activation energies as a function of excess bias calculated using the 10 % method for a commercial Si SPAD and 26, 50 and an earlier generation 100 µm diameter Ge-on-Si SPAD.*

These results are all within the same order of each other, however it appears the Si and 100 µm devices have activation energies with a low dependence on excess bias when compared to the 26 and 50 µm Ge-on-Si devices which show a more noticeable slope. As the activation energy required to excite a carrier from a trap should not be dependent on the excess bias across the device, the 26 and 50 µm devices showed more dependence that expected. Although the gradient may have flattened out for these devices had they been operated at higher excess biases, which should be investigated in the future.

### 6.6. Investigation of the Afterpulsing Experimental Parameters

Initially as with the previous DCR, SPDE and jitter measurements on SPAD 4.8 the DC voltage was approximately 1.4 V below the breakdown voltage. However, it was hypothesised that changing the DC voltage and altering the AC voltage to account for it would affect the afterpulsing probability by changing the electric field strength through the device when it is 'off'. One theory we postulated was, a device with a larger electric field between AC pulses turning the device on should have less afterpulsing as more carriers become excited out of traps quicker as they are under a constantly high electric field. This was investigated using different DC and corresponding AC voltage combinations to give a set excess bias. The experiment was carried out with a DC voltage at the breakdown voltage and at 0.96 and 0.93 of the breakdown voltages. The AC voltage has a trailing and leading edge of 10 ns and a width of 50 ns in order to avoid unwanted capacitive spikes at the leading and falling edges of the gates. Hence, having a higher DC current the trailing and leading edge of the AC pulse will be over the voltage breakdown for a longer period of time, up to 70 ns, whereas a lower DC current will only turn the device on for a maximum on 50 ns. This is because the output of the pulse pattern generator producing the AC voltage is set to peak at the voltage programmed for the given excess bias, as shown in Figure 6.19.

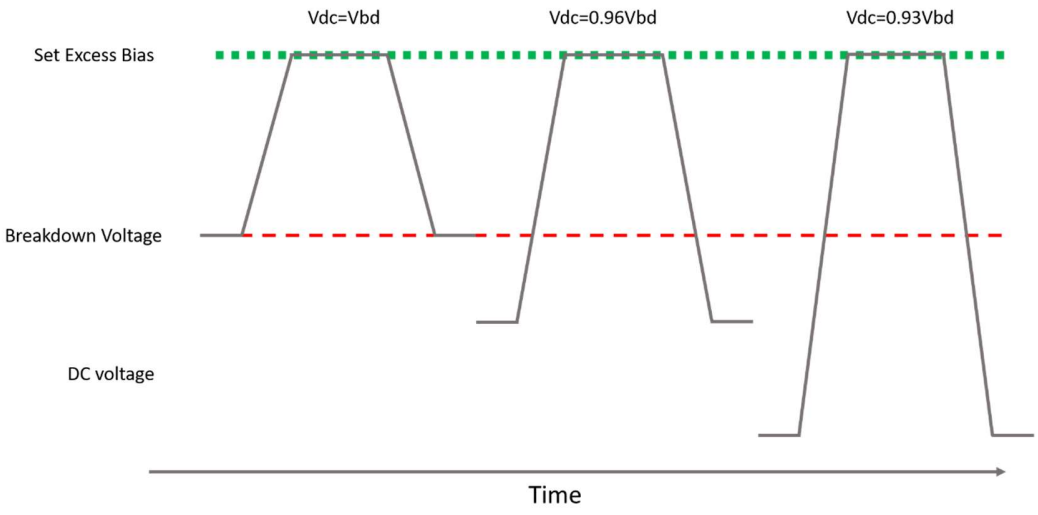


*Figure 6.19. The sloping rise and fall of the gate meant that different DC voltages meant the SPAD was above breakdown for different periods of time with the same excess bias.*

The results at an excess bias of 1 % are shown in Figure 6.20, at temperatures of 150 K, 125 K, 100 K and 77 K.

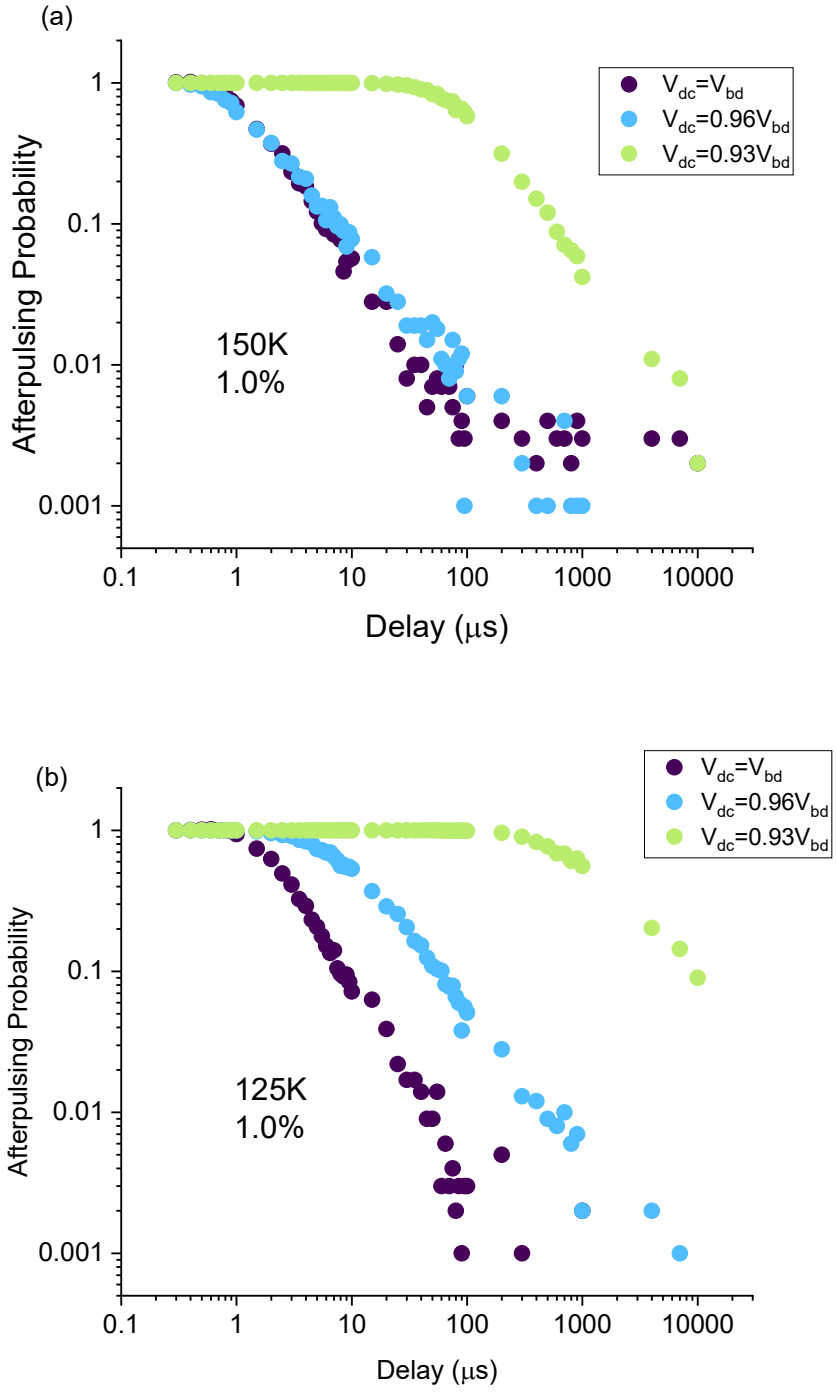

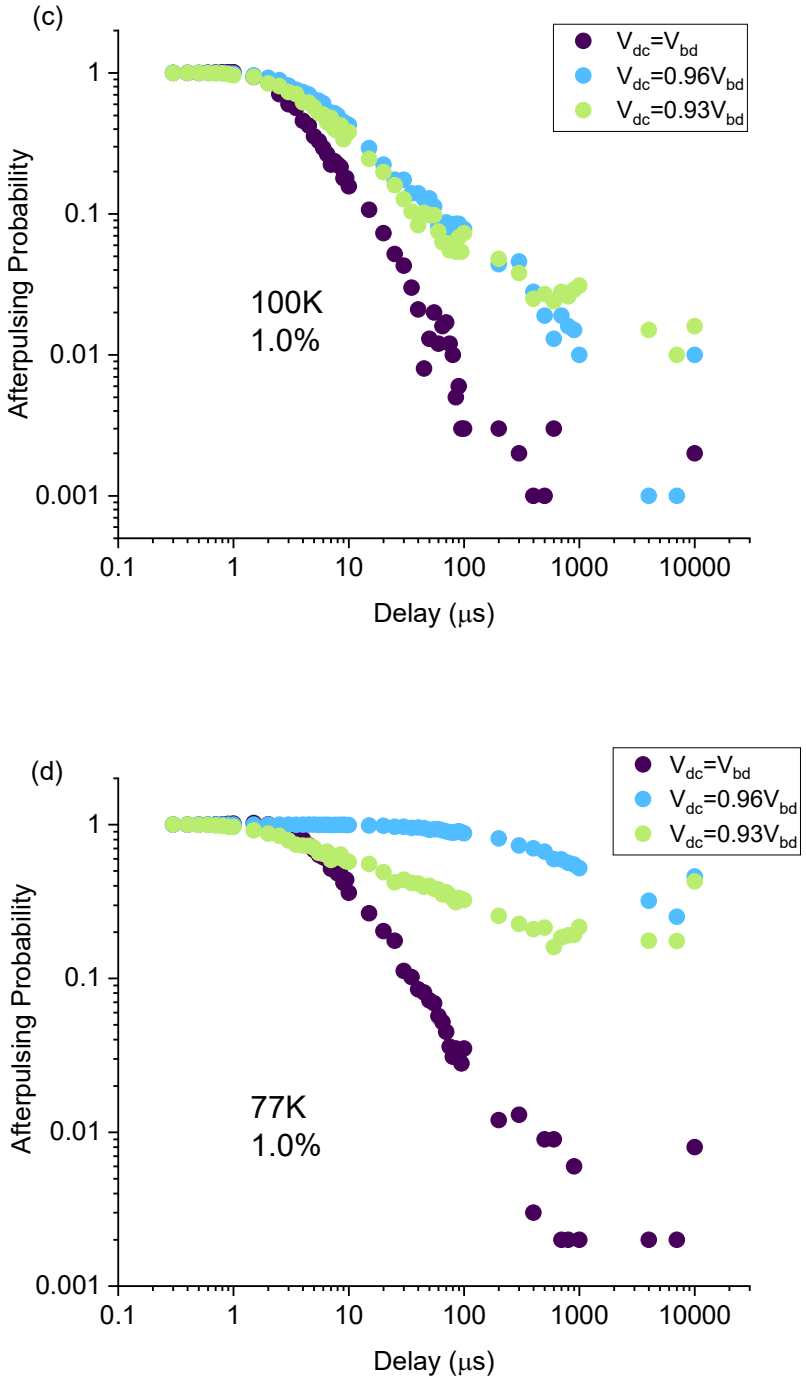


*Figure 6.20. Shows the afterpulsing versus set delay of a Ge-on-Si SPAD at an excess bias of 1% with different DC currents applied, where Vdc is the DC voltage and $V_{bd}$ is the breakdown voltage in the temperature range 77K to 150K.*

From these results we can see a considerable difference in the afterpulsing rate when the voltage is equal to the breakdown voltage and much higher rates for the other two curves. The reason for a lower afterpulsing rate with a DC voltage equal to breakdown could be, as mentioned above, caused by a combination of two factors, the wider gate and subsequently longer 'on' time for the device and the higher electric field between the device being turned 'on'. But we cannot draw any conclusions as the $V_{dc} = 0.96\ V_{bd}$ and $V_{dc} = 0.93\ V_{bd}$ results do not show any clear trends. As we did not perform SPDE readings with a DC equal to the breakdown voltage, we cannot prove that the device was effectively quenched making it possible that the device was not functioning as a SPAD as it was unable to absorb new photons when switched back 'on'. This would considerably lower the number of trapped carriers and explain the lower afterpulsing rate. At 0.96 and 0.93 of the voltage breakdown the results are unclear and so no conclusions were drawn from these results. From Figure 6.10, we would expect the afterpulsing to be higher for a higher DC voltage because the device is active for a longer duration, however that was not observed in these measurements. To explore this further we looked at the DCR of the devices under the same conditions. If the DCR for the same device at the same excess bias is the same, then the different afterpulsing results must be caused by the different electric fields across the device when it is switched off. Because having the same DCR at different DC/AC ratios would prove the device is on for the same amount of time in each case, or that the difference in 'on' times is small enough to be negligible in our calculations.

However, if the DCR under different DC currents varies then the width of the AC voltage must be the factor affecting the afterpulsing and the excess biases will need to be adjusted until the DCR under different DC voltages are the same. Comparing DCR produced the following graphs shown in Figure 6.21.

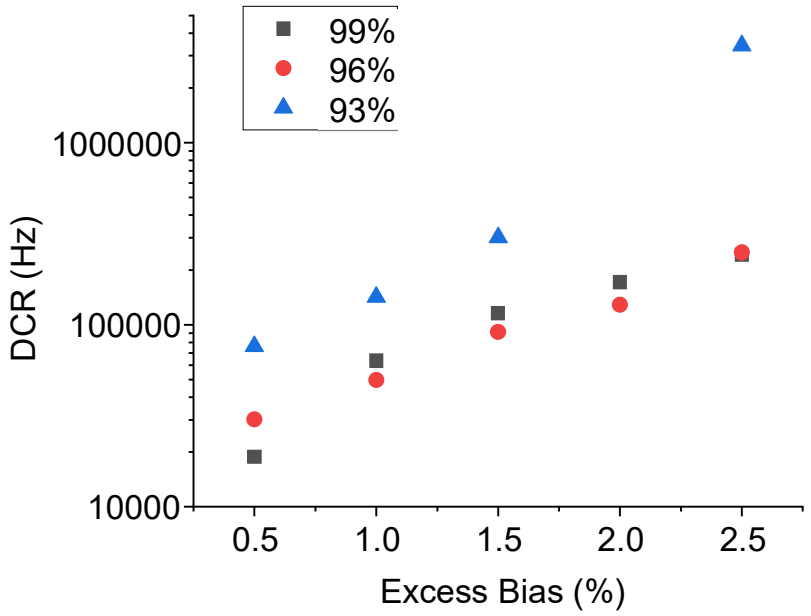


*Figure 6.21. The effect of changing the DC voltage from 93-99% of the breakdown voltage has on the DCR. In each case the overbias was identical.*

By comparing the DCR at the three different DC voltages, we can see some similarity between the 99 % and 96 % points and a much larger DCR at 93 %. But this is the opposite of what we would expect basing our predictions purely on Figure 6.19 and the different lengths of time the device is on for. So, we must conclude that the changing afterpulsing rates are caused by electric field differences between the device when being quenched and perhaps different levels of quenching.

Looking at Figure 6.22 it is evident the temperature dependence of afterpulsing is not abundantly clear either. We expect at lower temperatures carriers are trapped within the device for longer and the afterpulsing should increase but we have no way to differentiate a count caused by a trapped carrier and a count cause by a thermal excitation dictated by the DCR of the device. And so, we see when $V_{dc} = 0.96V_{bd}$, afterpulsing is dominating the results and 150 K shows a much lower rate than at 77 K, as expected. But at $0.99V_{bd}$ and $0.93V_{bd}$, 125 K has the highest afterpulsing rate. Perhaps a combination of trapped and thermally excited carriers caused by the electric field levels within the devices is causing this.

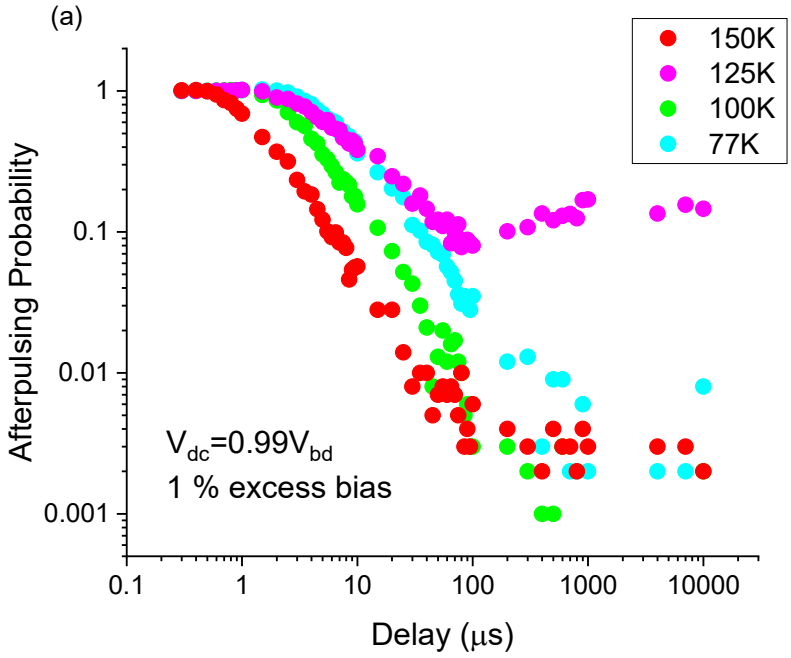
(a)
150K
125K
100K
77K
Afterpulsing Probability
1
0.1
0.01
0.001
$V_{dc}$=0.99$V_{bd}$
1 % excess bias
0.1
1
10
100
1000
10000
Delay (μs)

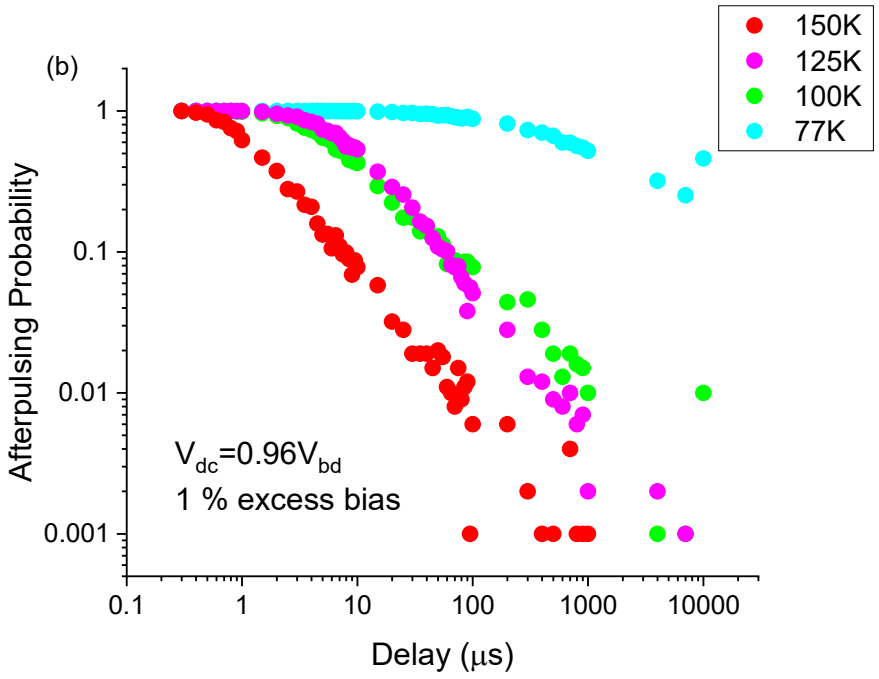
(b)
150K
125K
100K
77K
Afterpulsing Probability
1
0.1
0.01
0.001
$V_{dc}$=0.96$V_{bd}$
1 % excess bias
0.1
1
10
100
1000
10000
Delay (μs)

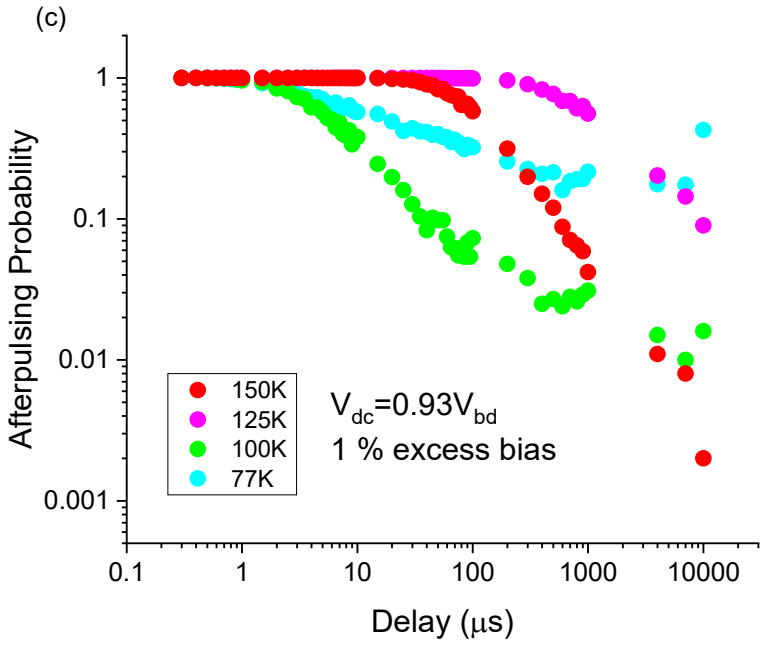


*Figure 6.22. Graph showing the effect temperature has on afterpulsing at an excess bias of 1 % for three different $V_{dc}$ values.*

This leads to another line of questioning: why does the DC voltage effect the ratio of afterpulsing to thermal counts? Further investigation into the reliability of these results was needed. Unfortunately, during the afterpulsing tests the device short circuited and no more tests could be performed on the same device. To summarise, we were able to calculate activation energies between 7 and 30 meV for Ge-on-Si SPADs. This did not correspond to any of the known trap states at the Ge-Si heterointerface [32]. We also studied the effect of altering the DC to AC voltage ratio, which did lead to different rates of afterpulsing although the reason for this was not understood. And the peak temperature of device operation where afterpulsing was at its lowest changed based on this ratio, this is another area that needs to be investigated in the future.

### 6.7 Fitting Physical Significance to Decay Behaviour

To analyse the afterpulsing decay graphs we used an exponential fit as mentioned in the previous section. We assumed this to be an adequate measure of decay rate as we made

assumptions about the nature of the reaction causing an avalanche, but these assumptions are potentially incorrect and to improve reliability of results the exact mechanisms leading to afterpulsing behaviour were further scrutinised. For a system to decay exponentially the probability of a reaction of a particular particle taking place must remain at a constant rate. And if the probability of a particular reaction taking place is R then the number of reactions per unit time is: $\frac{dN}{dt} = -RN$. Which has the solution $N = N_0 e^{-Rt}$ , hence the exponential fit. This in practical terms would model a small number of dominant trap types within the SPAD that are thermally activated [33]. Yet, when analysing the results, the exponential fit only appears to be a suitable measure at lower time delays and a much poorer fit at time delays near and above the time constant, as can be seen in Figure 6.23.

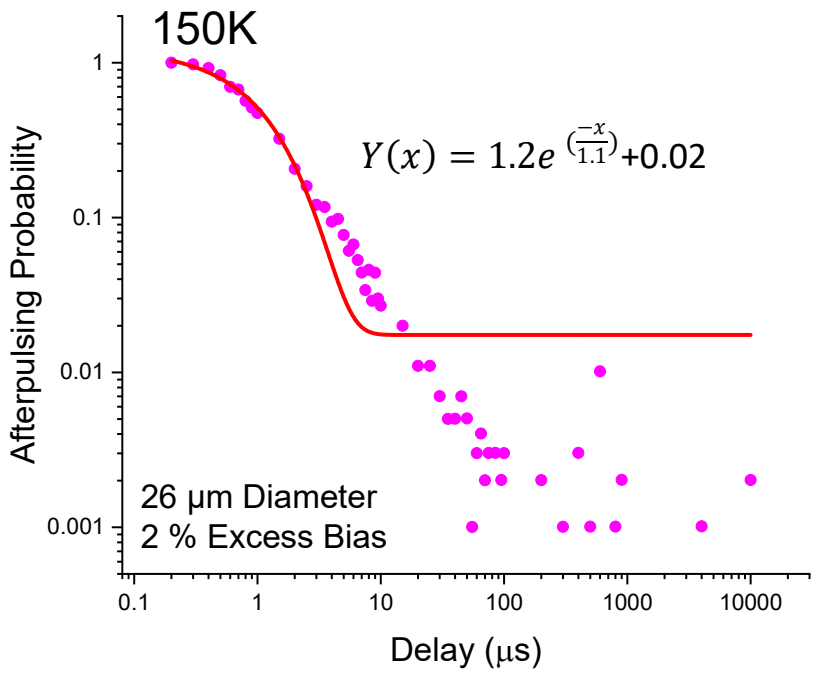


*Figure 6.23. Using OriginPro software to fit an exponential decay to the absolute afterpulsing probability of a Ge-on-Si SPAD at 150 K with an excess bias of 2%.*

Using two or more exponential fits to represent many mechanisms contributing formed fits with lower deviation from my results but highlighted the arbitrariness of the time constants

because they lacked physical significance and therefore were not representing information about the particular particles and their contribution.

It is however clear on a log-log plot that the afterpulsing decay, disregarding the saturation and noise contributing to the flat top and bottom of the graph, has a clear linear relationship between the time delay and afterpulsing probability, the linear relationship is highlighted in Figure 6.24. This behaviour corresponds with a power law decay, as shown in Equation 6.2. And it has been noted in the past as a better fit to Si and InGaAs/InP devices experimental results when compared to using an exponential fit [13, 34].

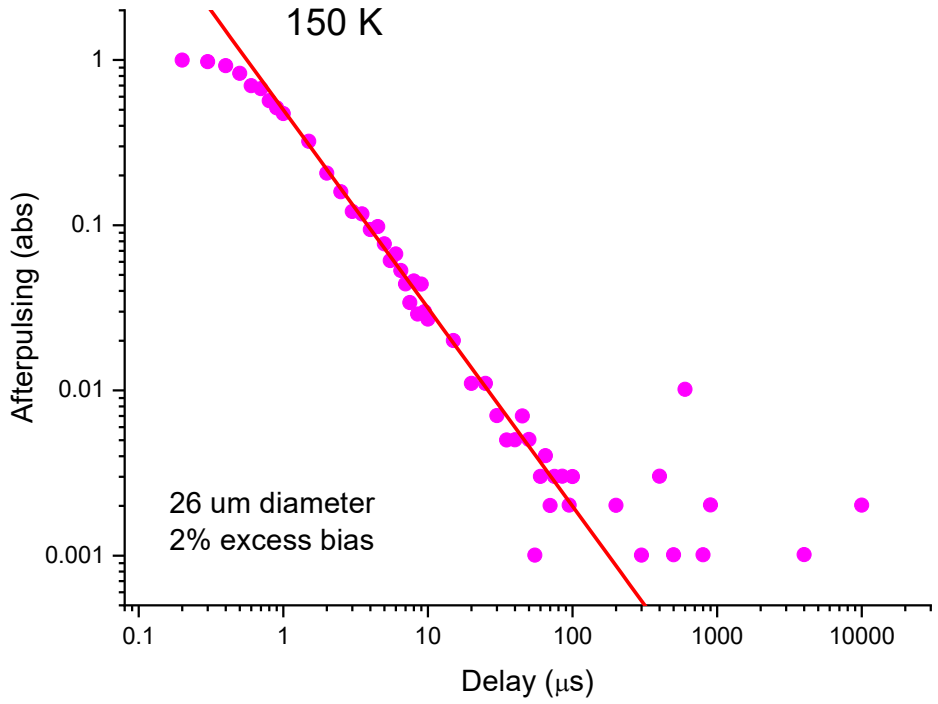


*Figure 6.24. Example of the linear relationship between the delay and afterpulsing probability of a Ge-on-Si SPAD at 150 K with an excess bias of 2%, when plotted on a log-log plot.*

By fitting power law decays to my results there was merit in investigating whether it produced interesting information and was a legitimate method of fitting for both the Ge-on-Si and Si SPAD afterpulsing behaviour and using this method to compare against SPADS fabricated from other material systems. The mean α value for the Ge-on-Si SPAD 4.8 26 μm SPAD was 1.08 and for the commercial Si SPAD the mean α value was 1.5. To investigate

how reliable these results were, they were compared to the results reported by S.Cova in his paper 'Progress in Silicon Single-Photon Avalanche Diodes' [7]. It was found that the Si SPAD reported had a mean α value of 1.55 calculated from the three excess biases investigated, this result is not unlike the Si SPAD that was investigated. I also considered the Ge-on-Si 100 µm SPAD reported by Vines et al. [32]. Which found the mean α to be approximately 1.25. Although not as similar to the 26 µm device it is worth noting that all devices had α values of between 1 and 1.55.

While we were unable to specify the exact physical significance of the power law decay, in the paper 'An explanation of the power-law decay of Luminescence' D J Huntly found α was typically between 1-1.5 and that the power law relationship can result from the tunnelling of trapped electrons to recombination centres, whereby the distribution is exponential in energy [33] . This suggests that using only one or two exponential fits to represent one or two trap levels could be misleading.

Another avenue for assigning physical significance to the decay behaviour was emphasised by Itzler et al. [13]. In research into the afterpulsing in InGaAs/InP and Si SPADs they found that if the distribution of states is inversely proportional to the detrapping rate then a power law fit would have physical significance. This is based on the theory of diffusion limited reactions, whereby a reaction would remove some of the reactant from a specific region and causes a reduction in the density of the reactants locally. It would then take a significant amount of time for the density of the reactant species to even out again and therefore the distribution and the mobility of the reactants affect the decay rate which takes the form of a power law decay, shown in Equation 6.2, when both species are symmetric for example electrons and holes [35].

He also observed the power law dependence and investigates the behaviour as though the device has exponential de-trapping from a broad distribution of trap levels instead of a few dominant trap levels. If the afterpulsing probability is directionally proportional to the change in trap concentration, then $\frac{dN}{dt} \sim Re^{-tR}$. Where the rate R is the inverse of the time

constant τ. Then if there is a broad spectrum of trap levels the distribution of detrapping rates can be described as D(R). And so if we integrated over the distribution of detrapping rates such that:

$$P \sim \int_{tmin}^{tmax} dRD(R)Re^{-tR} \tag{6.4}$$

We should end up with a power law decay. If there only exists one dominant trap the distribution would be a delta function: D(R) = δ(R-$R_o$) and the solution would be $P \propto R_o e^{-tR_o}$. However, we established earlier an exponential fit did not describe the full decay over longer periods of time. If D(R) was constant, then the result of the integral would equal:

$P \propto -\frac{cR^{-tR}}{t} - \frac{ce^{-tR}}{t^2}$, and with a D(R)=1/ R the result is $P \propto -\frac{-e^{-tR}}{t}$. To get an idea of what these results look like compared to a power law decay, they were plotted with arbitrary amplitudes, background levels and R and C values in Figure 6.25.

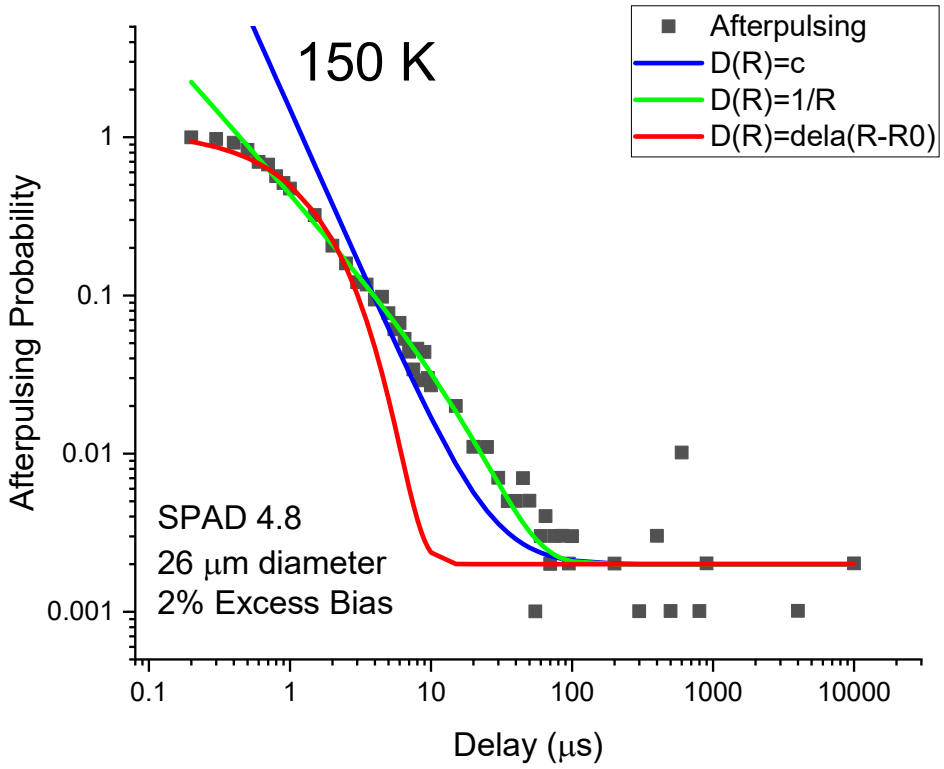


*Figure 6.25. Example of afterpulsing decay data from a Ge-on-Si SPAD with three different fits based on different distributions of trap levels. Measurements performed at 150 K with an excess bias of 2%.*

From Figure 6.25 it is clear that the behaviour that warranted the best fit to the experimental results was that of D(R)= 1/R. From this it seems that the narrow distributions such as a delta or gaussian function produce exponential decays whereas a wider distribution for example one that is constant or proportional to 1/R results in a power law decay. Based on this, we can assume the afterpulsing being initiated within the Ge-on-Si SPADs do show a wide distribution of detrapping rates however there are still the nonlinear parts of the curve that do not fit a power law decay and could indicate as Itzler mentioned that Si detrapping rates are somewhere between an exponential and a power law decay. This is a small step towards narrowing down the origin of the afterpulsing.

## 6.8 Conclusions and Future Work

In terms of afterpulsing a great deal of work still has to be done to establish the origin of traps in the Ge-on-Si SPAD, and its potential advantages compared to other material systems. For example the Heriot-Watt group are now examining Si SPADs fabricated under similar conditions as the Ge-on-Si to establish the effect of the Si layer in isolation. Also, by looking at different sized Ge-on-Si SPADs the edge effects of afterpulsing can be examined.

### *6.8.1 Novel FELIX Experiment*

A novel experiment was proposed to verify our afterpulsing results and activation energy values calculated from them. The principle of the following experiment is to use a laser to release trapped carriers by resonant excitation in the device. This will allow us to understand the energy level of the carriers which would identify their origin. This information would allow us to alter the fabrication methods in different ways to avoid the effect of trap incorporation, as well as finding optical ways in which we can release trapped carriers from within the device. To perform the experiment would require a laser with energies around that of the activation energies we calculated earlier, this is approximately 5-30 meV. Such low energies correspond to laser wavelengths between approximately 250-40 μm which would be difficult to acquire. And so, we successfully applied to use the Felix laser contained at the Radboud University in the Netherlands, the experiment would use a similar set-up as shown in Figure 6.2 with the Felix 1 laser both temporally and physically aligned with the SPAD which would be housed in a Microstat He Oxford Instruments cryostat provided by Felix laboratory. The temperature-dependent breakdown voltage would allow us to study potential temperature fluctuations within the MicrostatHe and the effect that has on the breakdown voltage of the device. If needed, we would then use the breakdown voltage as a more accurate measure of temperature.

Once the preliminary experiments have been performed, we would need to align both the 1310 nm wavelength diode laser with the active area of the device. Felix would then be aligned, using specialist lens/mirrors suitable for the wavelength we wish to study. When both lasers are successfully aligned with the active area of the SPAD the timing of the lasers will be adjusted so they are triggered at the same time We will be quenching the device using

an AC voltage as mentioned earlier in the afterpulsing experiment. Once all the equipment is aligned and the devices have been tested the main body of the experiment can commence.

A set of afterpulsing measurements will be taken with only the 1310 nm wavelength diode laser illuminating the device. We expect to see similar results to Figure 6.4 whereby the number of non-illuminated avalanches in the second gate decreases with delay time as we believe the traps are emptying over time. This will act as our reference. We then perform a second set of measurements with both the 1310 nm diode laser and the tuneable Felix 1 laser illuminating the device. If our prediction is correct the afterpulsing will be severely reduced as the traps will have been emptied by Felix 1 illumination. If this is indeed the case, then this novel experiment will confirm the activation energy of the traps matches the Felix 1 pulse energy and prove, not only that the activation energy of the traps is accurate and the method of analysis used is correct, but that it is possible to study defects in materials using the experiment we have proposed here. This experiment was proposed with the help of Professor Ben Murdin at the University of Surrey and Professor Carl Pidgeon at Heriot-Watt University.

### *6.8.2 Conclusions*

Afterpulsing probability as a function of delay time has been experimentally measured in Ge-on-Si SPADs. The results have been compared to a commercial Si SPAD obtained under similar operating conditions. Although the afterpulsing probability in the current Ge-on-Si is not currently as good as those of Si, similar afterpulsing activation energies were demonstrated, giving some evidence that the origin of the traps may be in the Si layer in Ge-on-Si SPADs when comparing large area devices (i.e greater than 100 μm diameter). In the case of 100 μm diameter Ge-on-Si SPADs the energies ranged from 50 to 90 meV. For the small diameters of 26 μm and 50 μm Ge-on-Si SPADs exhibit activation energies that ranged from 7 to 30 meV which may indicate an additional trapping mechanism. When the same analysis method was used for the Si SPAD activation energies were between 43 and 64 meV depending on excess bias.

To confirm our hypothesis, we also analysed the other methods used to calculate activation energies such as manually fitting exponentials, using two exponential terms, and fitting a power law decay and found that the power law decay formed a better fit to the experimental results for all the devices we looked at.

The time constant associated with the power law decay α had an average value of 1.5 for the commercial Si SPAD and 1.08 for the 26 μm charge sheet diameter Ge-on-Si SPAD with a 15 μm superpixel width. This was compared to the Si SPAD reported by S.Cova which was 1.55 [7]. By analysing the 100 μm Ge-on-Si SPAD data reported by Vines et al. [32] , the time constant was estimated as 1.25. For both Si and Ge-on-Si SPADs, the time constant almost always falls between 1-1.5 which is expected if afterpulsing is caused by trap-assisted tunnelling behaviour of electrons with an exponential distribution of energy [33]. Unfortunately, we were unable to assign some physical energy values to the time constants calculated using power law decay and whether this method could lead to accurate trap level calculations would need to be investigated further. Overall, there is some evidence that Si appears to be dominating the trap lifetime in Ge-on-Si SPADs, however more work needs to be performed on different device diameters and a larger temperature range in order to provide further evidence.

A new experiment was proposed which could validate the activation energies by using a laser to empty the traps immediately between device operation, and once performed could conclude the most accurate method of analysing afterpulsing data and calculating trap energies. Once the origin of the traps can be verified, procedures to reduce these impurities can be undertaken, for example, there is typically a high number of threading dislocations in the Ge epitaxial layer which could form mid-gap states and not only lead to afterpulsing but can increase dark currents too [36-38]. And if that does prove to be the source of the dominant afterpulsing traps adjustments to the current growth conditions and geometry for the Ge epitaxial layer process should be adjusted.

The next steps to continuing this research would be looking at the afterpulsing of a commercial Ge device to then calculate the activation energy of its traps and compare to the Ge-on-Si device traps. If we have found an accurate method of calculating the activation energy, and we are correct that it is the dominant cause of afterpulsing we can isolate the source of the traps.

**References**

[1] F. Thorburn, X. Yi, Z. Greener, J. Kirkoda, R. Millar, L. Huddleston, D. Paul, G. Buller, Ge-on-Si single-photon avalanche diode detectors for short-wave infrared wavelengths, Journal of Physics: Photonics, (2021).

[2] F. Wang, W. Chen, Y. Li, D. He, C. Wang, Y. Han, S. Wang, Z. Yin, Z. Han, Non-Markovian Property of Afterpulsing Effect in Single-Photon Avalanche Detector, Journal of Lightwave Technology, 34 (2016) 3610-3615.

[3] H.T. Yen, S.-D. Lin, C.-M. Tsai, A simple method to characterize the afterpulsing effect in single photon avalanche photodiode, Journal of Applied Physics, 104 (2008) 054504.

[4] S.J. Fancey, Single-photon avalanche diodes for time-resolved photoluminascence measurements in the near infra-red, (1996).

[5] A. Lacaita, F. Zappa, S. Cova, P. Lovati, Single-photon detection beyond 1 μm: performance of commercially available InGaAs/InP detectors, Appl. Opt., 35 (1996) 2986-2996.

[6] P. Hiskett, G. Buller, A. Loudon, J. Smith, I. Gontijo, A. Walker, P. Townsend, M. Robertson, Performance and Design of InGaAs /InP Photodiodes for Single-Photon Counting at 1.55 μm, Appl. Opt., 39 (2001) 6818-6829.

[7] M. Ghioni, A. Gulinatti, I. Rech, F. Zappa, S. Cova, Progress in Silicon Single-Photon Avalanche Diodes, Selected Topics in Quantum Electronics, IEEE Journal of, 13 (2007) 852-862.

[8] D. Bronzi, S. Tisa, F. Villa, S. Bellisai, A. Tosi, F. Zappa, Fast Sensing and Quenching of CMOS SPADs for Minimal Afterpulsing Effects, IEEE Photonics Technology Letters, 25 (2013) 776-779.

[9] M. Liu, C. Hu, J.C. Campbell, Z. Pan, M.M. Tashima, *Reduce Afterpulsing of Single Photon Avalanche Diodes Using Passive Quenching With Active Reset*, IEEE Journal of Quantum Electronics, 44 (2008) 430-434.
[10] Y. Xu, T. Zhao, D. Li, *An accurate behavioral model for single-photon avalanche diode statistical performance simulation*, Superlattices and Microstructures, 113 (2018) 635-643.
[11] D.B. Horoshko, V.N. Chizhevsky, S.Y. Kilin, *Afterpulsing model based on the quasi-continuous distribution of deep levels in single-photon avalanche diodes*, Journal of Modern Optics, 64 (2017) 191-195.
[12] G. Ribordy, J.-D. Gautier, H. Zbinden, N. Gisin, *Performance of InGaAs/InP avalanche photodiodes as gated-mode photon counters*, Appl. Opt., 37 (1998) 2272-2277.
[13] X.J. Mark Itzler, Mark Entwistle, *Power law temporal dependence of InGaAs/InP SPAD afterpulsing*, Journal of Modern Optics, (2012).
[14] R. Pagano, D. Corso, S. Lombardo, G. Valvo, D.N. Sanfilippo, G. Fallica, S. Libertino, *Dark Current in Silicon Photomultiplier Pixels: Data and Model*, IEEE Transactions on Electron Devices, 59 (2012) 2410-2416.
[15] M.A. Itzler, r. Ben-Michael, C.F. Hsu, K. Slomkowski, A. Tosi, S. Cova, F. Zappa, R. Ispasoiu, *Single photon avalanche diodes (SPADs) for 1.5 μm photon counting applications,* Journal of Modern Optics, 54 (2007) 283-304.
[16] E. Engelmann, S. Vinogradov, E. Popova, F. Wiest, P. Iskra, W. Gebauer, S. Loebner, T. Ganka, C. Dietzinger, R. Fojt, *Extraction of activation energies from temperature dependence of dark currents of SiPM*, IOP Publishing, pp. 042049.
[17] G.S. Buller, R.E. Warburton, S. Pellegrini, J.S. Ng, J.P.R. David, L.J.J. Tan, A.B. Krysa, S.Cova, *Single-Photon avalanche diode detectors for quantum key distribution*, IET Optoelectronics, 1 (2007) 249-254.
[18] B. Korzh, T. Lunghi, K. Kuzmenko, G. Boso, H. Zbinden, *Afterpulsing studies of low-noise InGaAs/InP single-photon negative-feedback avalanche diodes*, Journal of Modern Optics, 62 (2015) 1151-1157.
[19] T. Kaneda, H. Fukuda, T. Mikawa, Y. Banba, Y. Toyama, H. Ando, *Shallow-junction p+-n germanium avalanche photodiodes (APD's)*, Applied Physics Letters, 34 (1979) 866-868.

[20] T. Mikawa, S. Kagawa, T. Kaneda, T. Sakurai, H. Ando, O. Mikami, *A low-noise np germanium avalanche photodiode*, IEEE Journal of Quantum Electronics, 17 (1981) 210-216.
[21] S. Cova, M. Ghioni, A. Lotito, I. Rech, F. Zappa, *Evolution and prospects for single-photon avalanche diodes and quenching circuits*, Journal of modern optics, 51 (2004) 1267-1288.
[22] A. Tosi, A.D. Mora, F. Zappa, S. Cova, *Germanium and InGaAs/InP SPADs for single-photon detection in the near-infrared*, SPIE2007.
[23] B.F. Levine, C.G. Bethea, J.C. Campbell, *Near room temperature 1.3 ¼m single photon counting with a InGaAs avalanche photodiode*, Electronics Letters, 20 (1984) 596-598.
[24] K.E. Jensen, P.I. Hopman, E.K. Duerr, E.A. Dauler, J.P. Donnelly, S.H. Groves, L.J. Mahoney, K.A. McIntosh, K.M. Molvar, A. Napoleone, *Afterpulsing in Geiger-mode avalanche photodiodes for 1.06 μ m wavelength*, Applied Physics Letters, 88 (2006) 133503.
[25] M. Liu, C. Hu, X. Bai, X. Guo, J.C. Campbell, Z. Pan, M.M. Tashima, High-*Performance InGaAs/InP Single-Photon Avalanche Photodiode*, IEEE Journal of Selected Topics in Quantum Electronics, 13 (2007) 887-894.
[26] G.S. Buller, S. Pellegrini, R.E. Warburton, J.S. Ng, L.J.J. Tan, A. Krysa, J.P.R. David, S. Cova, *Semiconductor avalanche diode detectors for quantum cryptography*, IEEE LEOS Newslett, 20 (2006) 20-24.
[27] A. Katz, *Indium phosphide and related materials: processing, technology, and devices*, Artech House Boston1992.
[28] IDQ, ID230 *Infrared Single-Photon Detector*, in: IDQuantique (Ed.)2021.
[29] MPD, *InGaAs SPAD - gated, in*: M.P. Devices (Ed.)2021.
[30] R.E. Warburton, *Infrared Time-Correlated Single-Photon Counting*, School of Engineering and Physical Sciences, Heriot-Watt University, Edinburgh, UK, 2008, pp. 157.
[31] *Laser Components*.
[32] P. Vines, K. Kuzmenko, J. Kirdoda, D.C.S. Dumas, M.M. Mirza, R.W. Millar, D.J. Paul, G.S. Buller, *High performance planar germanium-on-silicon single-photon avalanche diode detectors*, Nature Communications, 10 (2019) 1086.

[33] D.J. Huntley, *An explanation of the power-law decay of luminescence,* Journal of Physics Condensed Matter, 18 (2006) 1359-1365.
[34] A.W. Ziarkash, S.K. Joshi, M. Stipčević, R. Ursin, *Comparative study of afterpulsing behavior and models in single photon counting avalanche photo diode detectors*, Scientific reports, 8 (2018) 1-8.
[35] J.W. Lee, V. Privman, *Three-species diffusion-limited reaction with continuous density-decay exponents*, Journal of Physics A: Mathematical and General, 30 (1997) L317.
[36] J. Michel, J. Liu, L.C. Kimerling, *High-performance Ge-on-Si photodetectors*, Nature photonics, 4 (2010) 527-534.
[37] N.J.D. Martinez, M. Gehl, C.T. Derose, A.L. Starbuck, A.T. Pomerene, A.L. Lentine, D.C. Trotter, P.S. Davids, *Single photon detection in a waveguide-coupled Ge-on-Si lateral avalanche photodiode*, Opt. Express, 25 (2017) 16130-16139.
[38] *N.J.D*. Martinez, C.T. Derose, R.W. Brock, A.L. Starbuck, A.T. Pomerene, A.L. Lentine, D.C. Trotter, P.S. Davids, *High performance waveguide-coupled Ge-on-Si linear mode avalanche photodiodes*, Opt. Express, 24 (2016) 19072-19081.

# Chapter 7. Conclusions and Future Work

This thesis presented single-photon characterisation in planar geometry Ge-on-Si SPADs with a 1 μm Ge absorber, and small diameters of 26 and 50 μm. We found the highest SPDE achieved was 30 % at 1310 nm wavelength and a NEP of 4 x $10^{-17}$ $WHz^{-1/2}$ for a 26 μm diameter device. This NEP is the lowest measured for a Ge-on-Si SPAD, and is two orders of magnitude better than previously reported results of mesa geometry devices. The SPDE level is comparable to InGaAs/InP SPAD detectors [1-3]. In the past SPDE of up to 38 % have been found for Ge-on-Si SPADs with a 100 μm diameter [3]. An impressive jitter value of 126 ps was achieved, this is the lowest jitter reported using a Ge-on-Si SPAD. Hence, it can be concluded that reducing detector diameter and optimisation of fabrication processing have successfully improved Ge-on-Si SPADs performance.

We briefly looked at the current-voltage behaviour of Ge-on-Si SPADs containing 1, 1.5 and 2 μm thickness germanium absorbers , initially using preliminary devices fabricated without full optical access. The aim of using a thicker Ge layer was to increase the SPAD efficiency in the SWIR region. The dark IV characteristics show that SPADs with 2 μm Ge have similar breakdown voltages and dark current values to the previous batch of devices with 1 μm thickness Ge. This demonstrates the potential to produce thicker Ge absorption layer SPADs with similar characteristics such as low DCR, but with higher efficiency levels. It also suggests that the same fabrication process for thicker germanium absorber SPADs can be used in making optical access SPADs. However, as the yield of the 1, and 1.5 μm thickness absorber thickness devices were poor compared to previous batches, and the 2 μm thickness devices did not survive temperature cycling. The fabrication process was revisited and refined leading to the production of a final set of 2 μm thick germanium absorption layer SPADs that were reliable enough to perform reverse and forward IVs on, and photoresponse measurements allowing a comparison between the initial 26 and 50 μm diameter devices. These structures were compared to Ge-on-Si SPADs with a 1 μm thick germanium layer, as well as InGaAs/InP APDs and commercial Si and Ge APDs. The results showed considerable extension of the spectral operating region of the 2 μm thick Ge absorber SPADs when compared to the thinner devices and illustrated a clear design improvement. However, even the 2 μm thick Ge absorber SPAD did not reach the InGaAs/InP SPAD upper operating

wavelengths at temperatures of greater than 250 K, although the 2 μm thick absorber compared favourably with InGaAs/InP at temperatures under 150 K.

The effects of afterpulsing at different temperatures were observed on Ge-on-Si SPADs, and whilst at our desired room temperature operation afterpulsing is a less significant cause of high DCR, it will help us to study the origin of traps within the device which should enable a more informed design of optimised devices with a lower DCR. Characterising the time taken for the afterpulsing decay to fall to 10 % of its original value, we calculated activation energies of between 7 and 30 meV for a Ge-on-Si SPAD for small area devices and energies ranged from 50 to 90 meV for larger diameter devices. For large area commercially available Si SPAD devices, the activation energies were found to be between 43 and 64 meV. The comparison of large area Ge-on-Si SPADs and Si SPADs provides some evidence that the origin of the traps may be in the silicon multiplication layer in Ge-on-Si SPADs. A comparison was made between using the 10 % method and an exponential decay fitting method used to calculate the activation energy, the results were analysed, and although they were inconclusive as the physical significance of the time constants and the exact origin of the traps could not be established, nonetheless significant findings were made. By operating InGaAs/InP SPADs under the same conditions it was shown that Ge-on-Si SPADs can be operated at a faster gate repetition rate at temperatures < 175 K. We believe enhancing material quality in Si multiplication layer will further increase count rate by taking advantages of low background DCR and shorter de-trapping lifetime. The overall performance using Ge-Si material systems will be better than the existing InGaAs-InP systems whilst also costing less. A novel experiment was suggested as a way of verifying the validity of the activation energies calculated through different methods of analysis. It involves using a free electron laser to excite SPADs at the calculated activation energy whilst running afterpulsing experiments to study whether the laser excitation emptied the trapped carriers and therefore reduced the afterpulsing. This would determine the most accurate method for calculating the activation energy and help to assign physical significance to the fitting method.

A selection of InGaAsSb/GaSb and AlGaAsSb /GaSb APDs and SPADs were provided for testing by Lancaster University. Although a very low yield highlighted fabrication issues we were able to produce some IV graphs that showed SPAD and APD like behaviour; a considerable improvement was found from previous research showing a proof of concept using AlGaAsSb structures with GaSb absorption regions [3]. Again, the information was fed back to Lancaster University and they are working on improving the reliability and yield of the fabrication process.

### 7.1 Future Work

In the next stages of research, we will study the effect of device diameter on carrier lifetime, and this will help investigate areas for improvement in manufacture. Comparisons between 1550 nm, 905 nm and 940 nm wavelength detection also needs to be investigated for applications in LIDAR sensing for automobiles, and so performing the same characterization of the devices but at a range of wavelengths will not only allow us to study wavelength dependent behaviours of the devices but their potential for use in other applications. As InGaAs/InP SPADs currently dominate as SWIR detectors of choice it would be beneficial to characterise one using the same set-up and equipment to fairly and accurately compare to our samples of Ge-on-Si SPADs. The University of Glasgow is in the process of perfecting their fabrication of optical access SPADs by varying the Ge thickness, the charge sheet doping and passivation methods using a variety of different approaches. When the most reliable method is determined and when the devices have been completed, they will be characterised to allow for comparison between different thickness germanium absorber devices and different charge sheet doping densities, hopefully with higher absorption qualities and an optimised charge sheet higher Ge-on-Si SPAD SPDE values and lower DCR will be achievable. And, as previously mentioned, the set-up used to study SPDE, DCR and jitter will have to be adjusted to improve the collimation of the laser in preparation for smaller active area devices which is another area of interest when considering how to reduce the DCR further.

**References**

[1] R.E. Warburton, G. Intermite, M. Myronov, P. Allred, D.R. Leadley, K. Gallacher, D.J. Paul, N.J. Pilgrim, L.J. Lever, Z. Ikonic, *Ge-on-Si single-photon avalanche diode detectors: design, modeling, fabrication, and characterization at wavelengths 1310 and 1550 nm*, IEEE Transactions on Electron Devices, 60 (2013) 3807-3813.

[2] S. Pellegrini, R.E. Warburton, L.J.J. Tan, N. Jo Shien, A.B. Krysa, K. Groom, J.P.R. David, S. Cova, M.J. Robertson, G.S. Buller, *Design and performance of an InGaAs-InP single-photon avalanche diode detector*, IEEE Journal of Quantum Electronics, 42 (2006) 397-403.

[3] P. Vines, K. Kuzmenko, J. Kirdoda, D.C.S. Dumas, M.M. Mirza, R.W. Millar, D.J. Paul, G.S. Buller, *High performance planar germanium-on-silicon single-photon avalanche diode detectors*, Nature Communications, 10 (2019) 1086.